CHARACTERIZATION OF *IN VIVO* HUMAN SKIN IN RESPONSE TO MECHANICAL INDENTATION USING OPTICAL COHERENCE TOMOGRAPHY

BY

PIN-CHIEH HUANG

THESIS

Submitted in partial fulfillment of the requirements
for the degree of Master of Science in Bioengineering
in the Graduate College of the
University of Illinois at Urbana-Champaign, 2016

Urbana, Illinois

Adviser:

Professor Stephen A. Boppart

Abstract

The biomechanical response of skin can reflect not only health or localized pathology, but also systemic disease or an abnormal physiological condition of an individual. Both the intrinsic stiffness of the solid constituents and the time-evolved redistribution of fluid within skin tissue can influence the biomechanical response to external forces. Therefore, it is important not only to evaluate the responding skin dynamics upon mechanical perturbation, but also to understand the intrinsic viscoelastic properties and fluid dynamics in the skin. While the clinical diagnosis of skin pathologies relies mostly on visual inspection and manual palpation, a more quantitative tissue characterization is highly desirable. Optical coherence tomography (OCT) is an interferometry-based imaging modality that offers an imaging resolution (cellular level) that surpasses those of most standard clinical imaging tools and has shown to be able suitable for *in vivo* skin imaging. Therefore, this thesis investigates OCT-guided characterization of the biomechanical response of skin, as well as the viscoelastic properties and the characteristics of local fluid transport. Quantitative analysis metrics were developed and demonstrated on *in vivo* human subjects, and a significant difference between the mechanically-perturbed and non-perturbed skins is revealed. Additionally, the quantitative results exhibit differences in the post-indentation scenarios between the young skin and the aged skin. Functional OCT techniques, such as optical coherence elastography (OCE) and Doppler OCT, are demonstrated to assess the stiffness and fluid dynamics of *in vivo* human tissue as well. The OCE results successfully reveal the stiffness at different anatomical sites, and the Doppler OCT shows the existence of the micro-vessels. This thesis research demonstrates the feasibility of quantitative skin characterization, the assessment of skin elasticity, and the revelation of fluid flows. With these information combined, a more objective and potentially more accurate diagnosis tool for skin pathologies may be possible in the future.

Acknowledgments

First of all, I would like to thank my advisor, Prof. Stephen Boppart, for offering this research opportunity and making everything in this study possible. In addition, I thank the Procter and Gamble company for financially sponsoring this study. I also appreciate Prof. Michael Insana and everyone in his group for sharing the mechanical indentation testing instrument. I thank Darold Spillman for all the administrative assistance and Eric Chaney for helping with the IRB protocols.

I would like to thank all the past and current group members in the Biophotonics Imaging Lab. It has been a great pleasure to work with all my lab mates, who are intelligent, friendly, and continuously giving support. In particular, I thank Dr. Paritosh Pande for all the valuable discussions (regarding the quantitative analysis, especially), from time to time. I thank Dr. Ryan Shelton and Guillermo Monroy for helpful discussion about OCT when I first joined the group, and Ryan Nolan for helping with the skin indentation study at the very beginning. I also thank Dr. Adeel Ahmad for leading me into the field of OCE. I thank Yue Wang from Prof. Michael Insana's group for insightful discussion about elastography as well. Finally, but importantly, I would like to thank (in no specific order) Dr. Marina Marjanovic, Dr. Paritosh Pande (again), Dr. Kush Paul, Dr. Youbo Zhao, Dr. Aneesh Alex, Dr. Haohua Tu, Dr. Yuan-Zhi Liu, Dr. Adeel Ahmad (again), Dr. Yuan Liu, Dr. Nathan Shemonski, Fredrick South, Guillermo Monroy (again), Joanne Li, Andrew Bower, Sixian You, Eugene Ark, Javier Suarez, Kelly Mesa, and Jungeun Won for their encouragement, support (and snacks) from time to time.

Special thanks are given to my all my family on the other side of the Pacific Ocean, for their unconditional support and understanding (as always) for whatever I choose to do.

Table of Contents

1 Introduction

1.1 Overview

Skin health can reflect important physiological conditions of a person, given that abnormalities presented on the skin can be linked to both a localized malignancy (e.g. skin cancer) or systemic diseases (e.g. heart failure and diabetes). Note that skin cancer is the most common cancer in the United States [1], heart failure is responsible for 1 in 9 deaths in the United States in 2011 [2], and diabetes has a 12-14 % prevalence among adults in the United States in 2011-2012 [3]. The skin of a diseased patient may exhibit changes in biomechanical response, the viscoelastic properties, and the fluid content or dynamics within the tissue. Clinically, the diagnosis of a skin abnormality is commonly based on visual inspection or palpation, unless a biopsy is taken. To diagnose fluid retention or edema, typically the physician presses (i.e. introduces a localized compression) the skin and observes whether a temporary depression or "pit" is formed. As for the diagnosis of local skin lesions, visual inspection or manual palpation on the skin are commonly performed in order to detect the abnormal alteration in skin texture or stiffness (e.g. stiffening or softening) of the diseased region. However, the lack of proper instrumentation or quantitative characterization might lead to a more subjective and less accurate diagnostic results. On the other hand, biomedical imaging has been an actively developing field of study which has shown great potential for assisting non-invasively in clinical diagnosis. In this thesis, an optical-imaging-based technique is proposed, mainly optical coherence tomography (OCT), to enable quantitative evaluation of skin health conditions based on the biomechanical response, viscoelastic properties, and fluid dynamics. To characterize fluid retention, this thesis research proposes several quantitative metrics based on the morphological information given in the OCT images. It is

hypothesized that when an external mechanical indentation is introduced, the unbound extracellular fluid (ECF) within the skin would be expelled aside and hence reduce the distances between the cells or fibrous components. Therefore, not only the skin deformation, but also the optical intensity and the spatial pattern of the OCT images would alter accordingly. In addition to the quantification of the biomechanical response (outcome) of the mechanically perturbed skin, this research are also extended to investigate the underlying physical and physiological factors (causes) that would affect the spatial and temporal response of the skin. Two functional extensions of OCT, namely the optical coherence elastography (OCE) and Doppler OCT techniques, are performed on *in vivo* human subjects in order to investigate their feasibilities in measuring the elasticity and visualizing the fluid flows within tissues, respectively. It is believed that the capability of quantifying the stiffness and the blood flow could assist a more systematic understanding of the biomechanical response of the skin, which may potentially enhance the accuracy of the diagnosis process in the future. Moreover, the characterization of both the outcome of the skin response and the contributing physical and physiological factors of the skin can be conceivably performed via the same OCT system (with a few OCE hardware components added and the Doppler OCT algorithm implemented). Therefore, an integrated OCT system may be potentially developed to allow for a quantitative, multifunctional characterization for skin biomechanics, which may assist in the clinical diagnosis by providing more information in the future.

1.2 Skin health and biomechanical response

1.2.1 Skin structure and functions

Skin is one of the largest organs in the human body, which serves as the first barrier for protecting the body against the outer environment. It is composed of three main layers, namely the epidermis, dermis, and subcutaneous fat (Figure 1.1). The epidermis (0.06-1 mm) is a stratified squamous epithelium which contains keratinocytes that undergo cell division and differentiation [4, 5]. The dermis layer (1-4 mm) is a vascularized tissue, composed of supportive cell matrix components such as collagen (77%) and elastin (4%) [5, 6], as well as nerves, sweat glands, lymphatics cells, and hair follicles [4]. The subcutaneous layer contains fat, which is located beneath the dermis and above the fascia [4]. The complex nature of the skin gives rise to its unique biological, physical, chemical, and mechanical properties, while each can be related to the health condition of skin or the overall body. Here, this research is focused on the biomechanical response of skin to external mechanical forces.

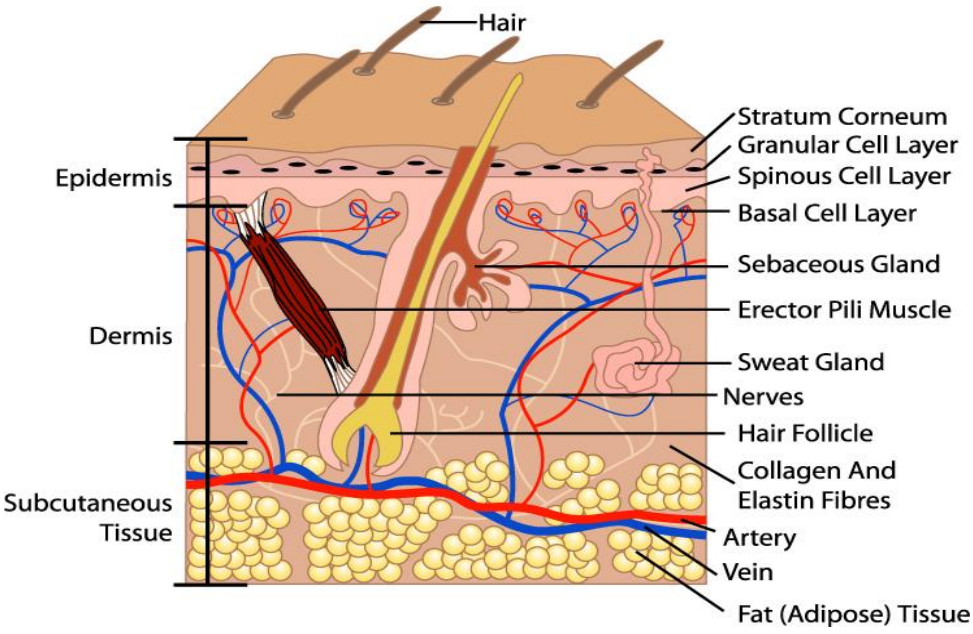

Figure 1.1. Human skin diagram [7]. Three main layers are shown, including the epidermis, dermis, and subcutaneous tissue.

1.2.2 Biomechanical properties of skin

The biomechanical response or properties of bulk skin can be affected by both the intrinsic viscoelasticity of the individual skin constituents as well as the overall physiological conditions, such as fluid retention or fluid distribution and flow. The mechanical integrity of skin is mostly determined by the dermis. At the cellular level, the dermis includes a large number of fibroblasts, which generate fibrous tissues (e.g. collagen and elastin) and structural proteoglycans [8]. The fibrous network can release stored energy and provide resistance to mechanical stress [9]. Collagen fibers provide mechanical support and the elastin assists in elastic recoil and maintaining normal elasticity and flexibility [8, 10]. The dermis is comprised of a thin papillary layer and a thicker reticular layer. The former lies beneath the epidermis and has thin and loosely organized collagen, and the deformation of dermal papillae is largely dependent on the behavior of the epidermis [11]. In contrast, the latter contains thicker collagen bundles lying in parallel to the skin surface, and the collagen fibers, along with the fiber bundles, form a three dimensional interwoven network, making the reticular dermis the major layer that provides resilience to skin [11]. Most collagens in skin are type I (80%) and type III (15%) [11].

Due to the fluid components in skin, other mechanical properties such as viscosity and porosity are observed as well. Apart from the fibrous tissues, the proteoglycans which contain glucosaminoglycans (GAGs) make up most of the extracellular fluid (ECF). The ECF can hold a great capacity of water (GAGs can bind 1000 times their volume in water [12]), and functions to provide nutrition, hormones, and fluid-based molecules to the dermis [10]. Due to their water-absorptive nature, proteoglycans can provide hydration, give "fullness" to the skin, and protect the skin against compressive loading [8, 10]. This fluid-related property also gives rise to viscosity, which describes the time-dependent fluid redistribution in tissue. Other sources of fluids within the skin are those that flow in the vasculature and lymphatics, which can be linked to the poroelasticity of skin. The fluid constituents, whether physically different or not, that reside in different compartments (e.g. extracellular space versus micro-vessels) can be modelled as distinct

phases, while the deformation of solid components can also be associated with the fluid exchange in the soft tissue [13].

1.2.3 Biomechanical response and diseases

A change in the biomechanical response of skin to an external force could be a result of several diseases, reflecting either a systemic or localized abnormality. The alteration of the overall mechanical properties of skin, as discussed earlier, can be related to either a change in the elasticity of the solid constituents, or a change in the visco- or poro-elasticity of the fluid components, or both. Localized skin lesions, such as early-stage melanoma, can change the arrangement of collagen fibers and induce a local stiffness change [14]. In cancerous skin, malignant melanomas and squamous cell carcinomas stiffen the skin, while basal cell carcinomas will soften the skin [15]. Connective tissue diseases, e.g. scleroderma and polyfibromatosis, generally reduce tissue extensibility as both conditions result in excessive amounts of collagen. While scleroderma results in an accumulation of type I and/or type III collagen within cutaneous tissue, polyfibromatosis involves an abundance of type III polymeric collagen within adventitial dermal tissues [9]. Scars, such as those induced by burns or poor wound healing, are known to increase skin stiffness [16], as various skin scar types (hypertophic, normotrophic, and keloid scar) involve collagen bundles arranged in a more parallel manner, compared to that of normal skin [17].

Fluid retention or swelling can also affect the time dependent biomechanical response of skin. An abnormal accumulation of fluid volume in tissue can lead to edema, which is commonly diagnosed by the finding of temporary depressions or “pits” on the skin of the feet, legs, or arms, when pressed. Various physiological processes can lead to edema, including the imbalance of fluid pressure, decreased drainage capacity, and increased permeability of the vasculature. Normally, fluids carrying nutrients often pass from capillaries to the interstitium to nourish the cells before returning to the capillary. When the blood pressure within capillaries is increased or when capillaries become more leaky, fluid will accumulate within the extracellular space and

hence swell the tissue [18]. In lymphedema, excessive interstitial fluid is present when the drainage capacity of the lymphatic system cannot accommodate the capillary filtration of the interstitial fluid [19]. Congestive heart failure can result from a decrease in cardiac output, which also disturbs the capacity of the kidneys for excreting sodium and water, and eventually leads to water retention and an increase in venous pressure [20]. Type 2 diabetes often induces cardiorenal dysfunction [21]. Edema of the lower limbs has also been reported as a symptom for thrombophlebitis, which is related to blood clotting and reduced blood flow velocity [22]. Induced by different diseases, water retention can take place at different locations in the dermis (e.g. in the subepidermal region for lipodermatosclerosis, the deep dermal area for heart failure, and more uniformly distributed for lymphedema) [23].

1.2.4 Biomechanical response and aging

The variation of skin biomechanical properties in healthy individuals can be large as well, due to the large variation in physiological conditions. Aging, in particular, can contribute remarkably to this variation. Aging involves chronic intrinsic and extrinsic (e.g. photoexposure, diet, etc) changes. Comparing the skin of young adults to that of the elderly, a decreased collagen synthesis rate, bundle thickness, content, and organization is exhibited in intrinsically aged skin, while photodamaged skin contains thick but fragmented collagen [24, 25]. In addition, aging induces an increase in collagen network density (due to the decrease in the extracellular volume) and the ratio of collagen type III to type I [25]. In aged skin, elastin fibers degrade due to the accumulative damage to existing fibers and the depletion of oxytalan fibers in dermal papillae [25], which increases the rigidity but decreases the elasticity and extensibility of skin [24]. The recovery time of skin from mechanical depression exhibits great differences (i.e. minutes in young skin versus more than 24 hours in aged skin) as well [24].

The water content, however, was found to increase in photoexposed aged skin. The water molecules in aged skin are mostly unbound (i.e. do not bind to proteins or GAGs), which likely

contributes to the dry and wrinkled appearance of aged skin [25]. In addition, a decrease in cutaneous perfusion and the number of blood vessels may potentially be related to aged skin as well [24, 26]. Infant skin, on the other hand, has been shown to have unique features in both structure and function, compared to adults [27]. The collagen in the upper reticular dermis of infants is thinner and less dense than in adults, and hence a clear distinction between dermal papillae and the reticular dermis is not seen in confocal laser scanning microscopy (CLSM) images [28]. Skin hydration increases after birth (possibly due to maturation of sweat glands), and the hydration level of the stratum corneum (SC) of older infants (3-12 months or 8-24 months) is significantly higher than that of adults [27, 29]. Interestingly, the barrier function of infant skin is not fully developed. A lower natural moisture factor concentration (which maintains the hydration level), less lipid levels on the skin surface, and a higher trans-epidermal water loss value are present in infants, suggesting that the higher water content in infant skin is potentially regulated by other factors, e.g. thinner SC, higher desquamation rate, or surface structure [27].

In summary, the skin biomechanical response is an important indicator of localized skin health, the systemic health condition, and physiological variations between individual humans. Therefore, new characterization tools and quantitative metrics for skin will offer the potential to assist in the clinical diagnosis, and are highly desirable.

1.3 Optical coherence tomography (OCT)

1.3.1 Introduction

Optical coherence tomography (OCT) is a biomedical imaging modality first published in 1991 and pioneered by Huang et al. [30]. OCT can be regarded as an optical analogue to ultrasound imaging, providing high-resolution cross-sectional images of biological samples based on their intrinsic optical scattering properties. However, unlike ultrasound, the speed of light ($\sim 3\times10^{8}\, m/s$) is too high to allow for time-of-flight pulse detection by current electronical

devices. Therefore, the basic principle of OCT relies on the detection of backscattering light intensity by using low coherence interferometry (LCI).

Typical image resolution of OCT range from 2-10 μm, which surpasses that of ultrasound imaging (100-200 μm), magnetic resonance imaging (500-1000 μm), and clinical computed x-ray tomography (500-1000 μm), but is not as high as that of most microscopes (< 1 μm). In contrast, the penetration depth of OCT (1-2 mm) is shallower than most standard clinical imaging techniques, but better than that of microscopy (Figure 1.2). In addition, OCT provides non-invasive depth-resolved assessment through *in vivo* tissues due to its use of near infrared wavelengths of light. Overall, OCT enables microscale resolution imaging capabilities while allowing *in vivo* non-invasive clinical imaging, making it an attractive imaging modality in biomedicine. A number of reviews on OCT can be found, such as [31-34].

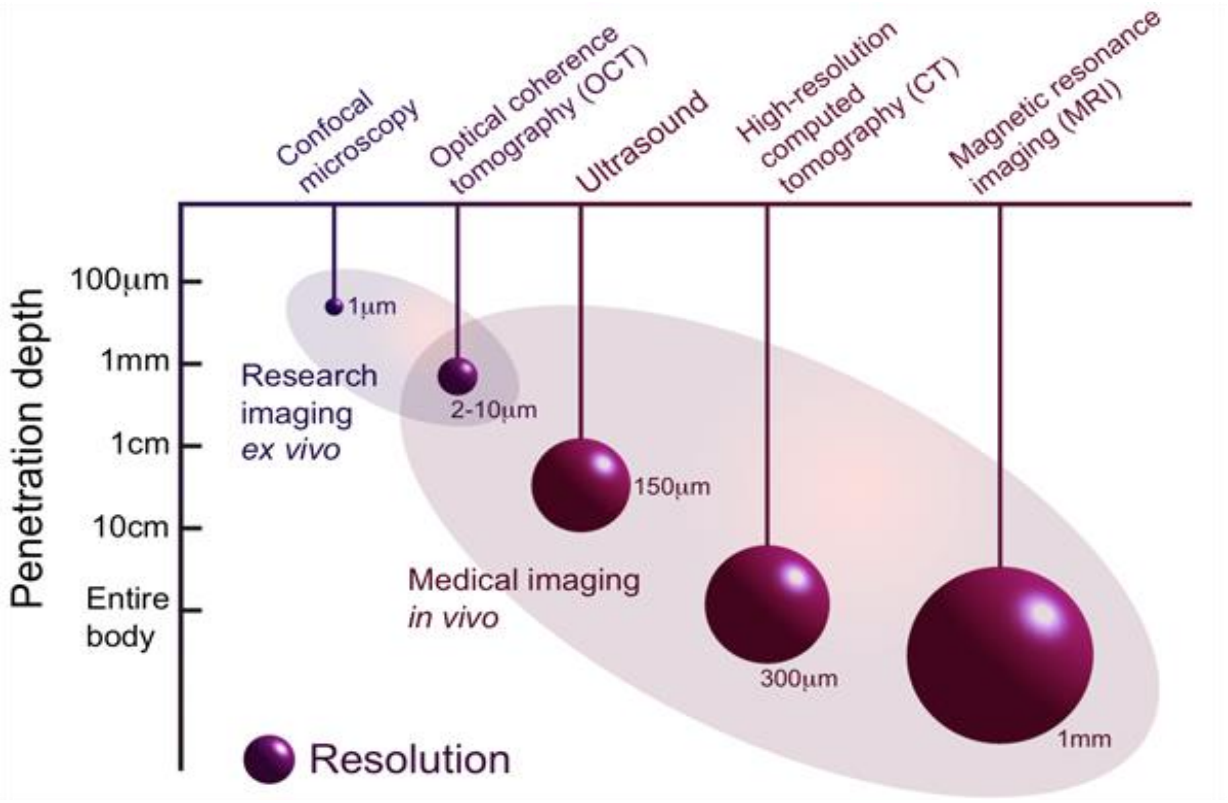

Figure 1.2. Comparison of image resolution and penetration depth of OCT with respect to multiple standard clinical imaging modalities [35]. The tradeoff between image resolution and penetration depth can be visualized.

1.3.2 Principle

OCT relies on the interaction between the tissue and ballistic or near-ballistic photons. Originating from the refractive index mismatch between different components, the depth-resolved reflection sites within the tissue can be mapped via low coherence interferometry (LCI). By assembling numerous adjacent LCI scans acquired across a certain range of lateral locations, a two–dimensional OCT image can be obtained. Usually, an "A-scan" represents one depth-resolved line scan obtained using LCI, a "B-scan" refers to a two-dimensional cross-sectional image consisting of several A-scans obtained across different lateral locations, and an "M-scan" refers to multiple A-scans acquired at the same location over time.

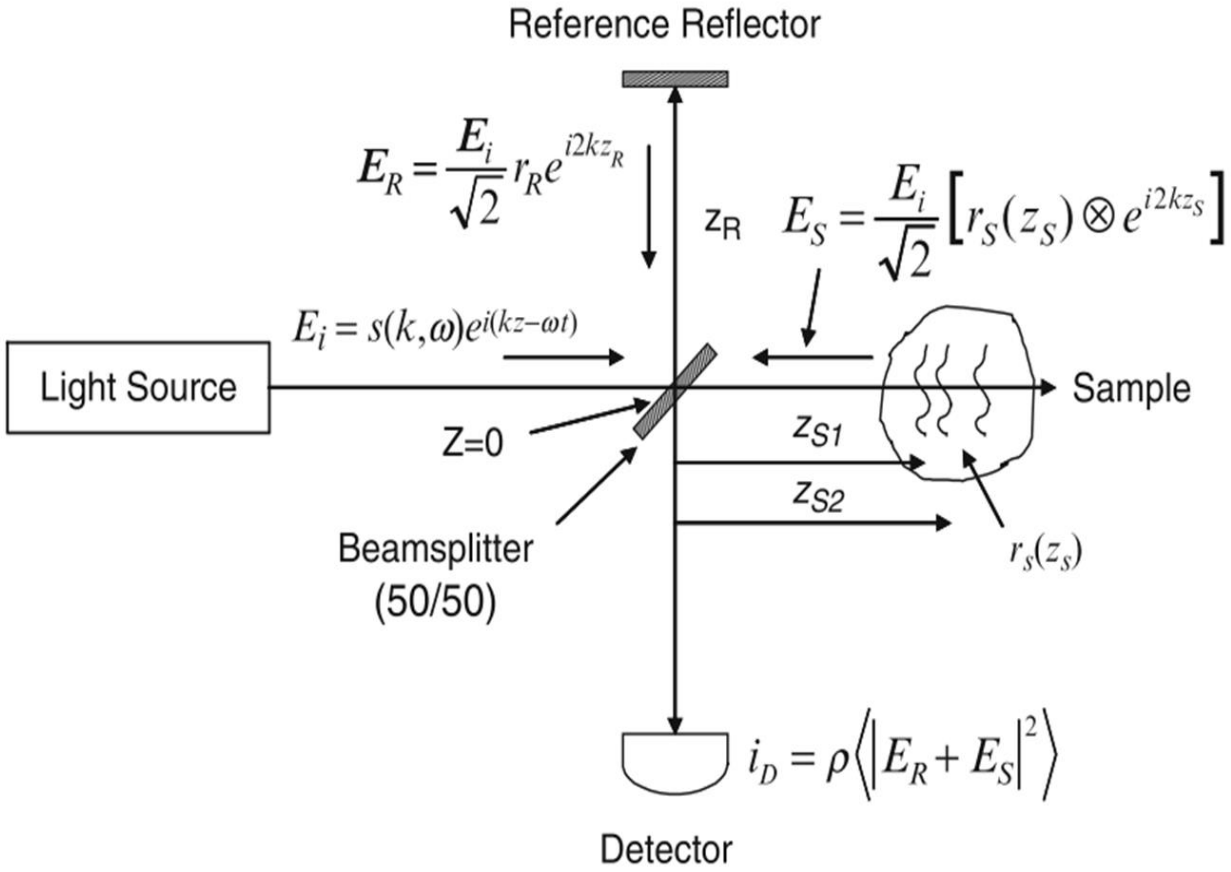

Figure 1.3. Basic scheme of OCT. A Michaelson interferometer configuration is shown with major components such as a low coherence light source, a reference arm consisting of a reference reflector or mirror, a sample arm, and a detector [33].

A basic OCT schematic is shown in Figure 1.3, which consists of a Michaelson interferometer with a low coherence, polychromatic light source. Consider that the electric field of the plane wave illumination is $E_i = s(k,\omega)e^{i(kz-\omega t)}$, where the wavenumber is $k = \frac{2\pi}{\lambda}$ (λ: wavelength), the angular frequency is $\omega = 2\pi\nu$ (ν: frequency), and the amplitude is $s(k,\omega)$. When the incident field E_i passes through a beam splitter or a 2-by-2 fiber optic coupler, E_i would be split into two identical beams, one going to the reference arm and the other to the sample arm. The returning waves (E_R, E_S), though, would vary based on the reflectivity of the object (r_R, r_S) and the optical pathlength delay (z_R, z_S) within each arm. Assume the tissue sample contains N discrete reflectors along one depth (**Error! Reference source not found.** (I)), the fields eturned from the reference and the sample arm would then be $E_R = \frac{E_i}{\sqrt{2}} r_R e^{i2kz_R}$ and $E_S = \frac{E_i}{\sqrt{2}} \sum_{n=1}^{N} r_{Sn} e^{i2kz_{Sn}}$, respectively. The expression of E_S is a result of $\frac{E_i}{\sqrt{2}}\left[r_S(z_S) \otimes e^{i2kz_S} \right]$, where $r_S(z_S) = \sum_{n=1}^{N} r_{Sn}\delta(z_S - z_{Sn})$, r_{Sn} represents the reflectivity at each refractive index mismatch boundary, z_{Sn} denotes the path length from the beam splitter, δ is the delta function, and $\otimes$ is convolution. The intensity can be obtained by $I(k,\omega) = \frac{\rho}{2}\left\langle |E_R + E_S|^2 \right\rangle$ and eventually can be written as [33]

$$I(k)=\frac{\rho}{4}\left[S(k)\left(R_R+R_{S1}+R_{S2}+\ldots\right)\right]\ \text{"DC terms"} \tag{1-1}$$
$$+\frac{\rho}{2}\left[S(k)\sum_{n=1}^{N}\sqrt{R_R R_{Sn}}\left(\cos\left[2k\left(z_R-z_{Sn}\right)\right]\right)\right]\ \text{"Cross-correlation terms"}\quad .$$
$$+\frac{\rho}{4}\left[S(k)\sum_{n\neq m=1}^{N}\sqrt{R_{Sn}R_{Sm}}\left(\cos\left[2k\left(z_{Sn}-z_{Sm}\right)\right]\right)\right]\ \text{"Auto-correlatoin terms"}$$

Here, ρ is the responsivity of the detector, and $S(k)=\left\langle|s(k,\omega)|^2\right\rangle$ is the power spectral density of the light source. The first term in the equation is the constant or D.C. signal containing no fringes. The last (autocorrelation) term is independent of the optical path length between the two arms and represents self-interference occurring between different reflective layers inside the sample. This is a common artifact in OCT systems and can be reduced by adjusting the reference reflectivity. The second (cross-correlation) term is the signal of interest, which carries the interference of the light reflected back from the mirror and that from each reflective boundary within the tissue sample. The main goal of OCT is to extract the reflectivity profile $r_S(z_S)$, which can be achieved by the use of Fourier-domain OCT, where depth-resolved reflectivity profiles can be obtained by the inverse Fourier transform of Equation **Error! Reference source not found.**). ventually, the cross-correlation term as a function of z can be obtained as [33]

$$i(z)_{cross-corr.}=\frac{\rho}{4}\sum_{n=1}^{N}\sqrt{R_R R_{Sn}}\left\{\gamma\left[2\left(z_R-z_{Sn}\right)\right]+\gamma\left[-2\left(z_R-z_{Sn}\right)\right]\right\}. \tag{1-2}$$

Here, $\gamma(z)$ represents the coherence function, whose Fourier transform becomes $S(k)$ according to the Wiener-Khinchin theorem. A factor of 2 is the result of the round-trip distance that the light travels. Illustrated in **Error! Reference source not found.**, one can see that in one A-scan, ultiple peaks are present, arising from each reflector boundary within the tissue, and where the delta-function (of the reflectivity profile) has been broadened due to the coherence function $\gamma(z)$.

Therefore, the axial resolution (i.e. point-spread function, PSF) is governed by the full-width half-maximum (FWHM) of $\gamma(z)$. This also defines the round-trip coherence length l_c. For a Gaussian beam, l_c is given as [33]

$$l_c = \frac{2\ln(2)}{\pi}\frac{\lambda_0^2}{\Delta\lambda}, \tag{1-3}$$

where λ_0 and $\Delta\lambda$ are the center wavelength and the wavelength bandwidth, respectively. Note that l_c is expressed in optical length here. To convert the optical length to physical length, the refractive index of the medium n that the light passes through should be added to the denominator of Equation (1-3) (i.e. $l_c = \frac{2\ln(2)}{n\pi}\frac{\lambda_0^2}{\Delta\lambda}$). This suggests that to achieve a low coherence length and provide high axial resolution in an OCT system, a broadband light source is highly desirable.

While the axial resolution is confined by the temporal coherence gate, the lateral resolution is determined by the confocal gate. In Figure 1.5, an OCT sample arm beam along with several important optical parameters are illustrated (assuming a cylindrically symmetric beam). The OCT sample arm beam travelling through a single-mode fiber can be regarded as a reflection-mode confocal microscope, where the fiber works similarly to a pinhole, both illuminating the sample and collecting the backscattered light. Defined by the FWHM of the intensity detected from a point reflector located at the focal plane of a reflection confocal microscope, the lateral resolution of OCT (dx) is provided as [33]

$$dx = 0.37\frac{\lambda_0}{\sin(\alpha)} = 0.37\frac{\lambda_0}{\mathrm{NA}} \tag{1-4}$$

where λ_0 is the center wavelength and α is half of the angular aperture subtended by the objective lens. It is intuitive to understand the inverse relation between the lateral resolution and the

numerical aperture (NA, which equals $\sin(\alpha)$): the tighter the light is focused, the better the lateral resolution.

On the other hand, the axial field-of-view (FOV_{axial}) of the OCT beam can then be defined as the FWHM of the confocal axial response (intensity detected from a plane reflector at the focal plane of a confocal microscope), which is given as [33]

$$FOV_{axial} = \frac{0.565\lambda}{\sin^2(\alpha/2)} = \frac{0.565\lambda}{\sin^2\left[\frac{\sin^{-1}(NA)}{2}\right]}. \quad (1\text{-}5)$$

The equation can be understood as the tighter the beam focused, the smaller the range of depth-of-field. In addition, the trade-off between the lateral resolution and the light penetration depth of OCT can clearly be seen from Equation **Error! Reference source not found.**) and **Error! ference source not found.**). Up to this point, one can see that the axial and lateral resolutions of the OCT system are independent of each other.

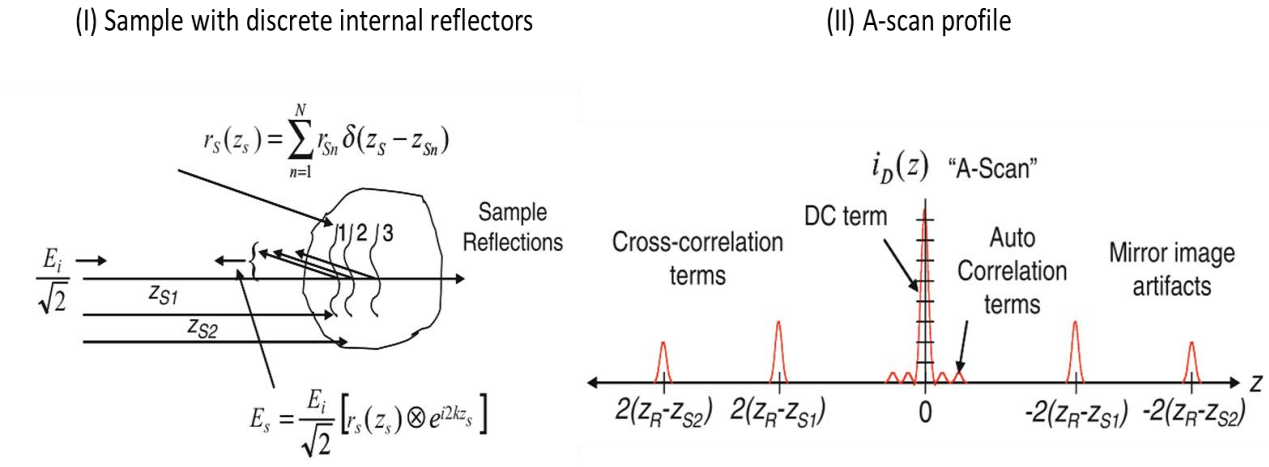

Figure 1.4. Illustration of the internal reflectors in a tissue sample and the A-scan profile along depth. (I) Discrete boundaries caused by refractive index mismatch, along with the incident and backscattered field, are plotted. (II) Cross-correlation term obtained from a SD-OCT system is shown. The zero position in the plot indicates $z_S=z_R$, where optical path length matches completely. Both figures are obtained from [33].

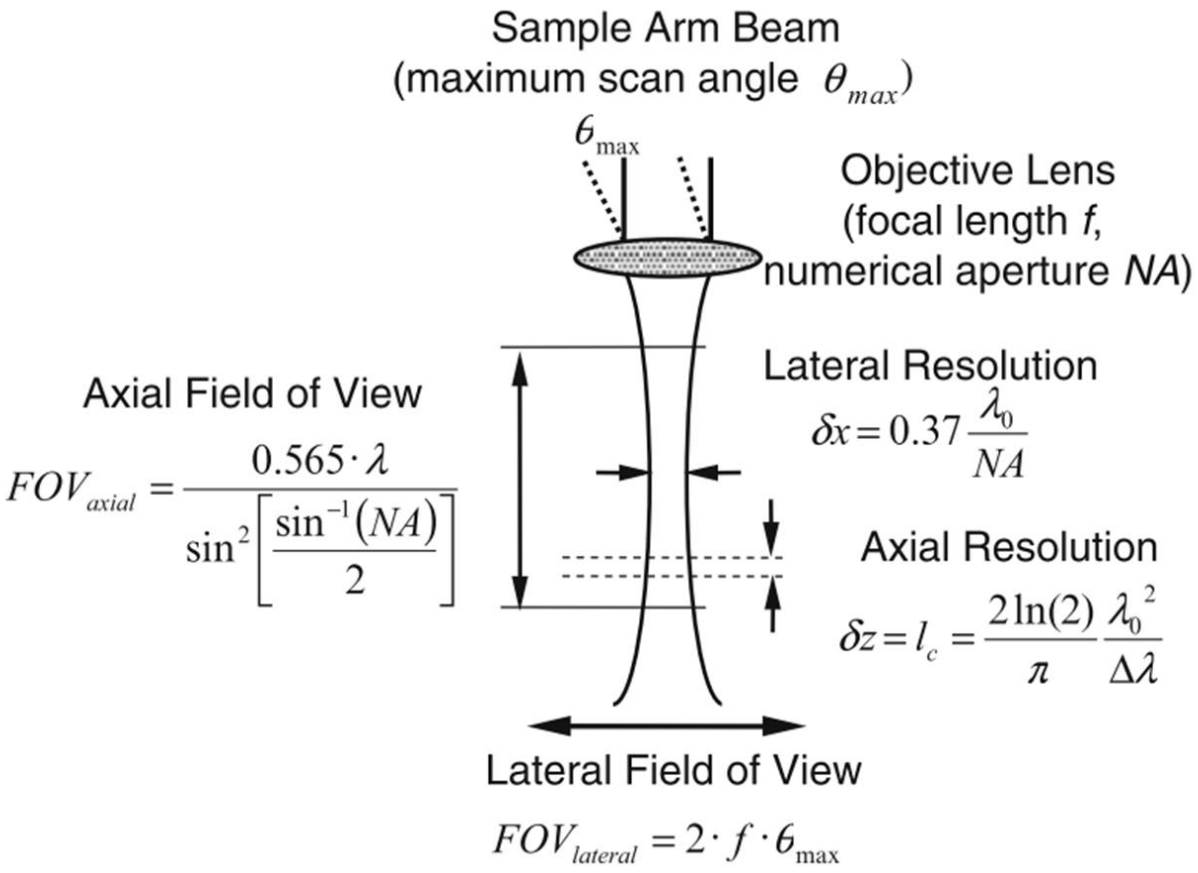

Figure 1.5. OCT sample arm and various optical parameters of the OCT system [33].

The light penetration depth into biological tissue is governed by the scattering and absorption characteristics of the tissue sample, which depends on the wavelength of the light. Most biological tissues are heterogeneous and made of different components, such as water, melanin, hemoglobin, oxygenated hemoglobin, and proteins. The wavelength-dependent absorption curves are characterized and shown in Figure 1.6. Melanin and hemoglobin (the main tissue chromophores) are less absorptive at wavelengths higher than 700 nm, while water is highly absorptive at wavelengths above 1300 nm. In addition, the red and near infrared (NIR) bands interact with tissue in a highly forward-scattering manner (anisotropy parameter g =0.85-0.9, which is close to 1) [32]. Therefore, the wavelength of the light source for OCT is commonly chosen to be within the

"biological window" of tissue, approximately 700-1300 nm, where scattering, rather than absorption, dominates. For example, for eye imaging, a center wavelength near 1300 nm is often avoided in order to reduce the high absorption from the large amount of water content in eyes. Wavelengths around 800 nm are often used, not only to reduce absorption, but also to afford higher imaging resolution at this shorter wavelength within the biological window.

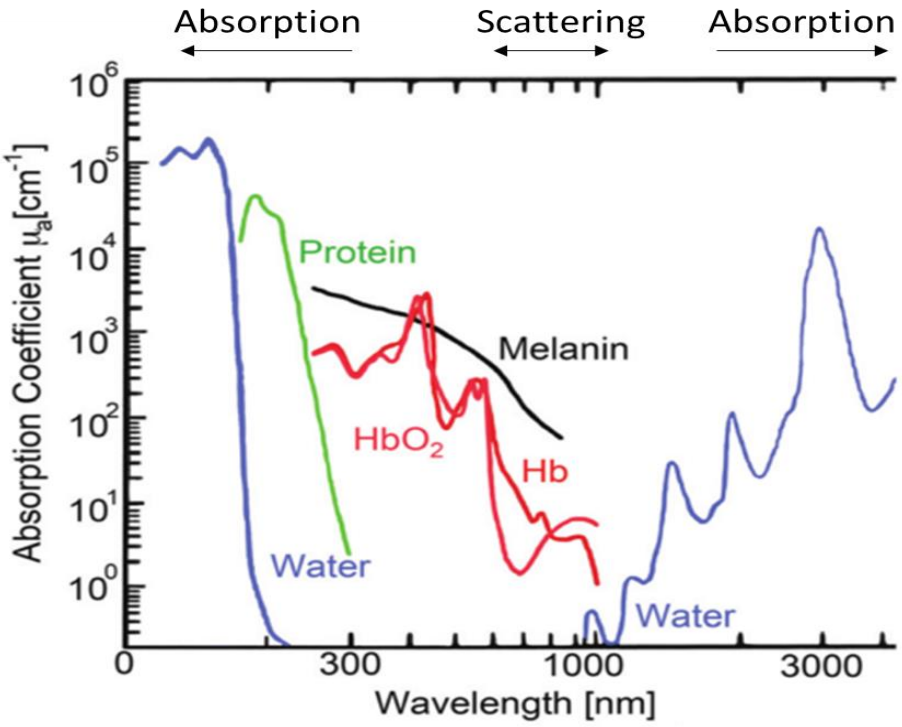

Figure 1.6. Wavelength-dependent absorption of various tissue biomolecules. The "biological window" refers to the wavelength range around 700-1300 nm, where scattering is more dominant over absorption for most molecules. Adapted from [36].

1.3.3 OCT system and instrumentation

Different instrumentation setups are required for OCT systems based on different scanning schemes. Three main types of OCT systems, namely time-domain (TD-OCT), spectral-domain (SD-OCT), and swept-source OCT (SS-OCT), are commonly used.

TD-OCT uses a continuous-wave broadband source to provide low coherence light, while the depth-resolved information is probed by moving the reference arm mirror to create a variable

time delay in the reflected signal. The interference signal is then collected via a photoreceiver. For both SD-OCT and SS-OCT, the depth-resolved information is encoded in the Fourier domain and hence the reference arm mirror is fixed at one location (where the optical path length between the two arms is matched). SD-OCT uses a continuous-wave broadband light source and acquires the depth-resolved information simultaneously (with a single data acquisition). A collimated beam encoded with the broadband spectrum is dispersed by the optical grating within a spectrometer, allowing different spectral frequencies to be mapped to individual pixels on a line scan camera. In SS-OCT, a light source that can rapidly sweep through a range of wavelengths is utilized. The fringes as a function of time are then detected by one or more photoreceiver(s). In both schemes, the depth-resolved information can be extracted by Fourier analysis of the measured spectral interference pattern [33].

1.3.4 Applications in biomedicine

OCT has been widely applied to the field of biomedicine and has been commercially available since 1995. Its sub-cellular level resolution provides the potential for detecting early changes in disease processes, with clear applications for biomedical investigation in ophthalmology [37], dermatology [38], oncology [39], cardiology [40], dentistry [41], and musculoskeletal diseases [42], to name a few. In particular, ophthalmic imaging has become the most clinically established application of OCT. For instance, OCT can detect the morphological changes within the retinal and further monitor or quantify progression of diseases such as age-related macular degeneration, macular edema caused by diabetes or retinal vein occlusion, and the treatment response of glaucoma patients [37]. In addition, the choroid in posterior segment diseases, retinal dystrophy, and intraocular tumors has been investigated with OCT as well [37].

Although conventional bench-top OCT systems perform well for fixed tissue or for ophthalmic imaging, the instrument design of an OCT system can also be adapted for other

applications. Catheter-endoscopes can be integrated into OCT and allow for imaging within internal biological lumens or organs, such as *ex vivo* human artery and *in vivo* rabbit esophagus [43, 44]. The light beam can be delivered with an optics fiber enclosed inside a rotating hollow cable, where a gradient index lens (GRIN) and a microprism are encased by a transparent sheath at the distal end of the fiber for beam focusing, and reflecting the beam in a perpendicular direction, respectively [43, 44]. In addition, OCT has also be engineered into a portable system with a handheld scanner, showing potential for point-of-care diagnosis. The handheld scanner has been realized by encasing the sample arm components into a handheld probe [45], while some designs also replace the conventional galvanometer-scanners with a small-size microelectromechanical system (MEMS) mirror to downsize the probe volume and weight, making the system more user-friendly [46]. Handheld scanners can also allow for real-time, *in vivo* imaging, which are suitable for intraoperative imaging [47].

Other functional extensions of OCT have been introduced as well. Polarization-sensitive OCT (PS-OCT) measures the cross-sectional polarization information, e.g. the phase retardation, to reveal the birefringence of linearly organized tissue. PS-OCT can assist in the diagnosis of glaucoma, the evaluation of collagen denaturation in burned skin, and the detection of cancerous tissue such as basal cell carcinoma (BCC) or breast tissue [48, 49]. Magnetomotive OCT (MM-OCT) utilizes magnetic nanoparticles (MNPs) as a dynamic contrast agent, where magnetomotion can be modulated by an external magnetic field. Using MM-OCT, injured vasculature can be detected by MNP-labeled platelets [50] and antibody-functionalized MNPs allow for *in vivo* tumor targeting prior to visualization [51]. Optical coherence elastography (OCE) is also a widely investigated extension, where the mechanical contrast of tissue is revealed in the sample displacement. OCE has showed potential for disease diagnosis and for tumor margin visualization

[52]. The presence of fluid flow or fluid dynamics can be assessed through Doppler OCT or optical microangiography (OMAG), which take advantage of the Doppler frequency shift and the blood-flow-induced modulation of the spectral interferogram, respectively. Both techniques are capable of visualizing and quantifying blood flow or perfusion *in vivo* [53, 54].

1.4 Statement of work

This thesis research evaluates the morphological changes of *in vivo* human skin induced by external mechanical indentation using OCT. In addition, the feasibility of using OCE and Doppler OCT to assess the biomechanical properties and fluid dynamics within the tissue are demonstrated, which may be the main contributors affecting the skin response during and after indentation. The chapters are organized as follows. Chapter 2 focuses on the quantitative characterization of the skin response before and after indentation, based on the structural features revealed in time-lapsed OCT images. The study design, the algorithm employed, and the quantification approaches are detailed, followed by the results of a clinical human study, where the indentation response of both adults and infants are presented, discussed, and compared. In Chapter 3, OCE techniques are introduced to enable the assessment of viscoelasticity of the biological tissue and provide preliminary datasets acquired from human skin. In Chapter 4, the fluid dynamics probed by Doppler OCT are discussed and *in vivo* human data are also provided. Finally, in Chapter 5, the conclusions of the current investigation of OCT-guided characterization of human skin biomechanics, and the future directions of this line of research, are both included.

2 Quantitative analysis of human skin in response to mechanical indentation

2.1 Introduction and motivation

The aim of this research is to investigate using OCT the biomechanical and tissue response of *in vivo* human skin after indentation, and define metrics for quantitative analysis. By applying an external mechanical compression on skin, various changes in the empirical parameters, such as the optical backscatter intensity and spatial distribution of speckle, are revealed in OCT images. It is hypothesized that this may be associated with the viscoelasticity and alteration of local fluid dynamics and hemodynamics in the indented sites. Geometric changes, such as the residual deformation and the recovery kinetics of the indented skin, are also observed and quantified. Based on these metrics, quantitative analysis was performed for both adult and infant skin data.

2.1.1 Study design

To investigate the skin response of human subjects with different physiological conditions and biomechanical properties, two groups of subjects varying in age were recruited to participate in study, including a total of 8 Caucasian female adults (20-32 years of age) and 8 Caucasian infants (9-18 months, 4 females and 4 males). For the adult group, the indentation sites were selected on the volar forearm, while the indentation was induced on the dorsal thigh for the infants. For each subject, the targeted indented locations were marked prior to the application of the indentation force. The indentation device and procedure is detailed in Section 2.1.2. For all subjects, the indentation force was held on the skin surface for 3 minutes, and the OCT images were acquired for the following conditions: before the indentation (pre-indentation), immediately after (<10 sec, for simplicity, this is denoted as "0-min") and after 1, 2, 3, 4, and 5 minutes after the indentation (post-indentation).

2.1.2 Indentation procedure and devices

Indentation form an applied external force to the skin was performed in *in vivo* human subject experiments. Indenters with a dimension shown in Figure 2.1 (I, II) were machined, while an elastic band (Seraket® Automatic Tourniquet 48300-770, Propper manufacturing Co., Inc., Long Island, NY) was used to hold the indenters in place for 3 minutes (Figure 2.1 (III, IV)). In order to fix the applied strain at 16.7%, the length of the elastic band was adjusted according to the circumferences of the body sites of the subjects. After indentation, the OCT probe was immediately (<10 sec) placed at the indented skin sites for image acquisition from 0 to 5 minutes, with an image-interval of one minute, in order to track the changes during the recovery process. During the imaging session, the subjects' forearms were rested on a metal-based "hand stand" covered with a soft fabric, in order to keep the skin surface flat and stable at all times (Figure 2.1 (IV)).

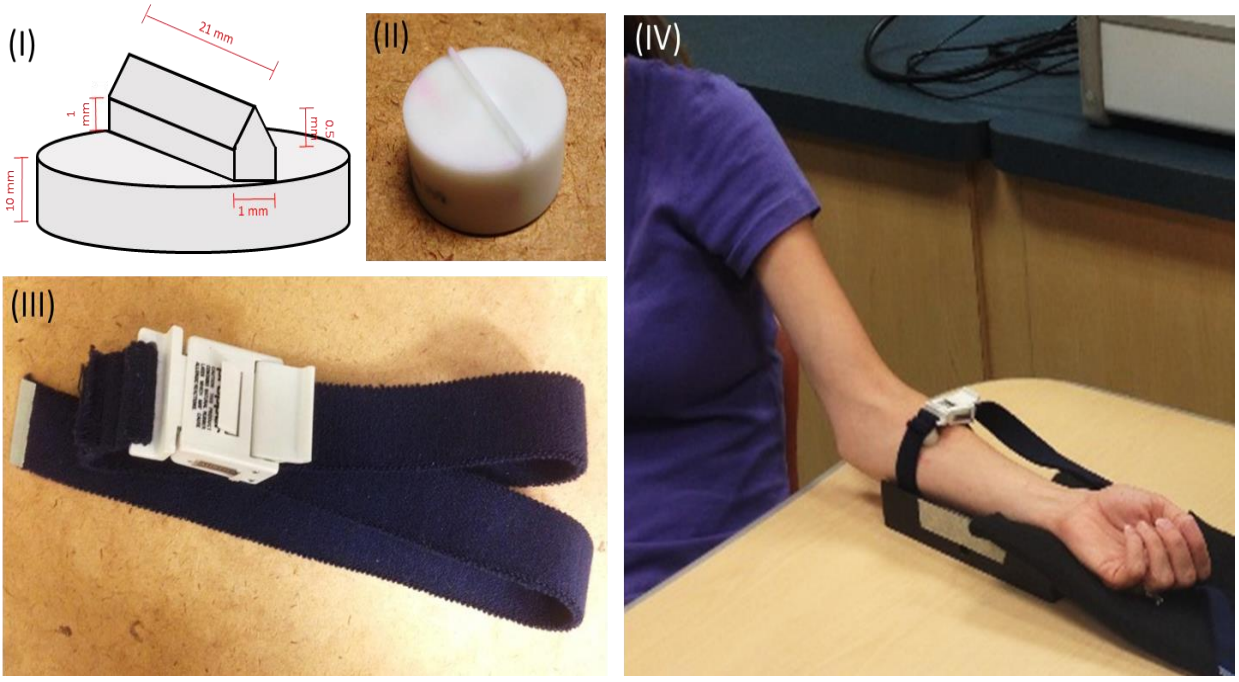

Figure 2.1. Indentation device and setup. (I) The geometry and dimension of the custom-made polymer indenter. (II) A photograph of the indenter. (III) The elastic strap used to hold the indenter in place. (IV) The patient undergoing the 3-min indentation procedure.

2.1.3 Experimental setup

Two OCT systems, one bench-up and one portable, were involved in this study. For the phantom sample experiment, a home-built bench-top SD-OCT system was used, whereas for the *in vivo* human study, a portable commercial SD-OCT system (Telesto, Thorlabs, Inc.) was used in order to better assess the subjects' skin at various body sites (forearm and thigh for adults and infants, respectively). The specifications of the bench-top system are the same as the one previously described [55]. In brief, a superluminescent diode (LS2000B, Thorlabs Inc.) with a center wavelength of 1310 nm and a bandwidth of 170 nm was used as the light source. The axial and the lateral resolutions were calculated to be ~ 4.5 μm and ~ 16 μm, respectively. The portable commercial OCT system had a center wavelength and bandwidth of 1310 nm and 100 nm, which corresponded to a theoretical axial and lateral resolution of 7.6 μm and 15 μm, respectively. During imaging, a relatively slow line scan rate (~ 5.5 kHz) was selected for both systems in order to achieve better sensitivity. The specifications of the two systems are summarized in Table 2.1.

Table 2.1. Specification of the two OCT systems used in this thesis research.

	Bench-top OCT	**Portable commercial OCT**
OCT Type	Spectral-domain	Spectral-domain
Center wavelength	1310 nm	1310 nm
Bandwidth	170 nm	100 nm
Axial resolution (in air)	4.5 μm	7.6 μm
Lateral resolution	16 μm	15 μm
Field-of-view	4 mm × 2.2 mm	6 mm × 2.5 mm

For the portable imaging system, a customized polymer-based attachment was mounted at the end of the rigid OCT scanner in order to enable handheld imaging and to keep the working distance constant between the sample and the lens. The physical dimensions of the probe attachment are shown in Figure 2.2 (I). The diameter of the aperture (~2.7 cm) is an order of magnitude larger than the width of the indenter tip (~1 mm). In addition, the ring-shaped edge

around the aperture was designed to have a wider area (~24.5 cm^2) so that the amount of pressure applied at the edge would be reduced. During the experiment, the probe was held manually not only to target the region of interest but also to avoid the weight of the probe resting on the skin (Figure 2.2 (III)). This was also to ensure that the localized-loading-induced fluid dynamics at the indented site would not be affected by the perturbation within the surrounding skin region.

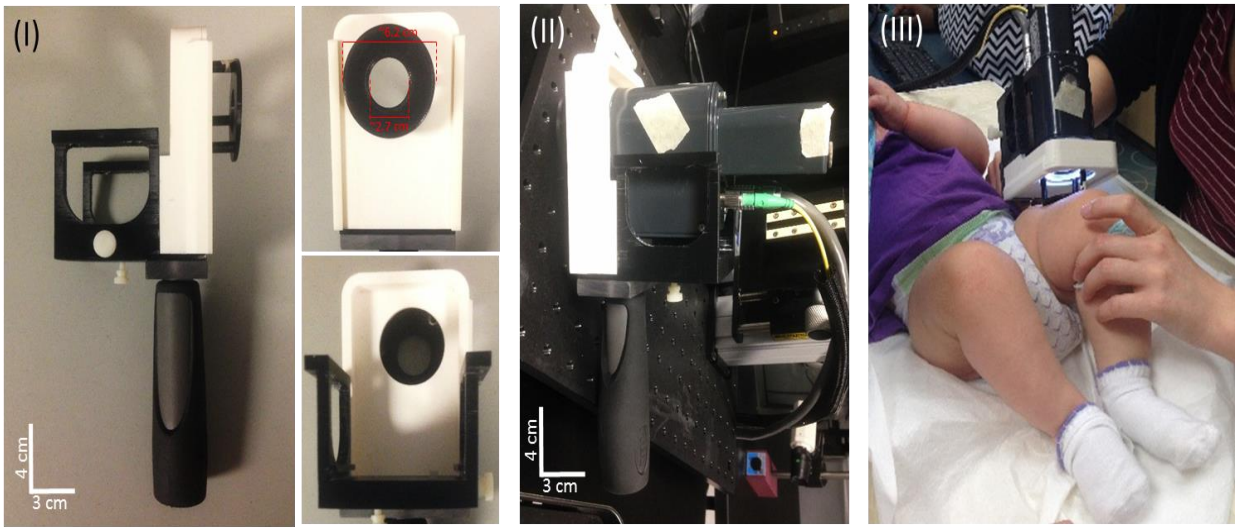

Figure 2.2. The handheld probe and the illustration of the imaging process. (I) The design and the dimensions of the handheld attachment. The photographs were taken from (left) the side, (top right), the side facing the skin, and (top bottom) the side carrying the rigid scanner head. (II) By mounting the rigid scanner to the attachment, (III) handheld OCT imaging was possible.

2.2 Selection of metrics

The metrics chosen here are broadly categorized into two groups, with one group focusing on the quantification of the in-tissue dynamics, and the other group focusing on the skin surface kinetics during the pre- and post- indentation time periods.

A number of algorithms have been proposed to extract the morphological features of biological tissues from OCT images [56, 57]. These algorithms can be generally grouped into two: one group that is related to the attenuation properties obtained from the backscattered intensity profile; and the other group that is associated with the spatial variation or speckle pattern revealed

from the OCT images. Therefore, for the in-tissue parameters, two features for characterization are also proposed, namely intensity-based and statistical features.

2.2.1 Intensity-based feature

Morphological information, as well as many optical properties of the tissue specimen, are often encoded in the intensity profiles within OCT images. Incident on any biological specimen, the OCT light intensity would inevitably diminish with depth, either due to the attenuation of the propagating ballistic light or due to the system roll-off. In SD-OCT, system roll-off is a result of the lack of sensitivity of the line scan camera detection at higher frequencies, which corresponds to deeper regions in an OCT image. The roll-off of the OCT systems (both bench-top and portable handheld OCT setups) were characterized to be negligible within the depth-of-field (decreased ~3% within a 2 mm depth range). Therefore, in this study, the light intensity changes were primarily caused by light-tissue interactions.

Optical attenuation as a function of depth is a combined result of absorption and scattering, and the Beer's Lambert law can be applied to characterize the attenuation coefficient [58],

$$\mu_t = \mu_a + \mu_s . \tag{2-1}$$

where μ_t , μ_a , and μ_s represent the total attenuation coefficients of tissue, absorption, and scattering, respectively. In the near-infrared region, the dominant factor is scattering (i.e. $\mu_s >> \mu_a$). As modelled in several studies, biological tissue can be regarded as being composed of solid (e.g. proteins, collagen, fibers, cells, etc) and fluid components (e.g. water, blood, extracellular or interstitial fluid, etc), while the bulk attenuation coefficient and average refractive index can be obtained based on the linear rule of mixture [59, 60]. When a pressure gradient is introduced to the tissue, the unbound water or fluids would by expelled aside, which effectively

decreases the fraction of the water contained at the indented site. Since the absorption coefficient of water is higher than that of other molecules near 1300 nm (shown in Figure 1.1, biological window), the bulk absorption coefficient of the tissue decreases as the water content is reduced [59]. On the other hand, the scattering coefficient within the tissue μ_s can be approximated as below [60].

$$\mu_s = \frac{3.28\pi r^2 \rho_s}{1-g}\left(\frac{2\pi r}{\lambda}\right)^{0.37}\left(\frac{n_s}{n_f+\delta n_{mol}}-1\right)^{2.09}. \quad (2\text{-}2)$$

Here, r and ρ_s are the radius and volume density of scattering centers, respectively. The term g is the scattering anisotropy factor, λ is the wavelength of light, and n_s, n_f, and δn_{mol} are the refractive indices of the scattering center, the fluid components, and the molecular-induced index increase, respectively. In skin, the refractive indices of the non-fluid components are typically greater than that of the fluid components ($n_{collagen}$ = 1.55 >> n_{water} = 1.32 at 1310 nm). Compression of the soft tissue induces refractive index matching of the solid components such as the extracellular matrix, and hence decreases scattering (i.e. when $n_s \approx n_f + \delta n_{mol}$, $\mu_s \to 0$). However, the compression of the skin thickness at the indentation site would result in an increase in the effective scatterers (i.e. the solid components) and the local chromophore concentration, which may lead to increasing μ_s and μ_a. Yet, overall, less attenuation was observed due to the significantly lower thickness (d) of the tissue (since the overall attenuation is characterized by $\left(\mu_a+\mu_s\right)d$) [60]. As a result, the OCT signal intensity increases and the depth of the light penetration is extended [61].

The attenuation coefficient or a similar parameter, e.g. signal slope, has been utilized to characterize the attenuation properties of tissues in several studies [62, 63]. However, the

compression-induced change of the attenuation coefficient may be subjected to the fit of the window size, which may be affected from the greatly reduced sample thickness. In addition, the attenuation coefficient does not necessary carry the information about the absolute intensity amplitude. The same attenuation trend may also arise from regions with different intensities.

Therefore, this research focused on the change in the absolute intensity value across a fixed area, which provides information regarding both the intensity increase and the enhanced penetration depth. Many studies have investigated the backscattered intensity change caused by the water fraction inside the tissue (e.g. the dehydration phenomena) and proposed to apply mechanical compression to optical clearing, allowing a larger penetration depth; while a few also reported the prolonged clearing effect on human tissue even after the release of a localized stress [60, 64]. One study demonstrated how the compression-induced intensity contrast could be used to distinguish between an inflamed *ex vivo* rectum and a tumor-bearing rectum [65]. However, rarely have studies implemented the use of the backscattered intensity change to quantitatively investigate the post-indentation residual effect on *in vivo* subjects with varying physiological conditions.

In this study, an intensity-based metric is defined as follows. For a validation (phantom) study, the absolute intensity value was quantified at each compression step. For the human subject study, the ratio of average intensity obtained from the indented region to the unperturbed area was chosen to reflect the level of deformation and local fluid transport upon mechanical compression. The changing intensity ratio as a function of time was also recorded after the indentation force was removed.

2.2.2 Statistical feature

Upon mechanical compression, the tissue becomes denser and hence this change affects not only the OCT signal but also the spatial distribution of the speckle. Here, the hypothesis is that the cumulative effect of the increased intensity, decreased attenuation, and a higher volume density of speckles can be revealed in a statistical parameter — a coefficient of variation.

Spatial variation of the tissue structure in OCT images can be extracted in numerous ways. Fourier or autocorrelation analysis is a common approach which detects the periodicity or repeated pattern of the tissue structure, and this has been applied in OCT data of breast and finger tissues [66, 67]. In one study [66], the mean distance between the strong intensity peaks was also used to to reveal the spatially periodic signals, which served as a criteria for differentiation between adipose, stroma, and tumor. To differentiate the variation of scatterer sizes, a time-frequency transform can be applied, which is often seen in spectroscopic OCT techniques [68].

Originating from the interference of multiple scattered waves within the confocal gate, speckle patterns within OCT images are affected by both the size and the quantity of the scatterers within the sample, and hence have been utilized to obtain texture information from tissues [69, 70]. Texture analysis includes structural, model-based, and statistical approaches, while the latter is more widely applied in OCT data [56]. In statistical texture analysis, one can take advantage of (1) the co-occurrence matrices (or spatial gray-level dependence matrices, SGLDMs), which evaluate the second-order joint conditional probability distribution, describing the probability of two pixels with specific intensity levels located at a certain direction [70-72], (2) the grey-scale run-length matrices (GLRLMs), which evaluate the number of consecutive pixels at a specific direction that expressed the same intensity level [73], or/and (3) the gray-level histogram based features [71]. In addition, basic statistics such as the standard deviation obtained after the removal

of the OCT signal attenuation slope has been applied for tissue characterization as well [63]. While many texture analysis approaches are subjective based on an observer's choice of parameters (window size, direction, etc), fractal analysis provides a more objective option to reflect geometric complexity and self-similarity of an object. Fractal analysis relies on the fractal dimension, where the calculation requires dividing the data into different scales of smaller datasets, and obtains the number of datasets that contain an intensity above a certain threshold value [74].

In the indented skin, optical intensity would increase, and hence standard deviation alone is not effective enough for sparseness characterization. Here, the coefficient of variation (CV) is utilized as an alternative statistical parameter, which is also simple and computationally low-cost, to characterize the dispersion of the speckle pattern in tissues. The CV is defined as:

$$\text{Coefficient of variation (CV)} = \frac{\text{standard deviation (std)}}{mean} \tag{2-3}$$

CV is often applied for data homogeneity testing, where in imaging the CV of the speckle intensity indicates a relative standard deviation and describes how sparse the speckle is distributed at a certain ROI. Typically, a smaller CV value implies a more homogeneous environment. Originally applied to synthetic aperture radar (SAR) imaging, speckle filtering has been carried out in an adaptive manner based on the local structural heterogeneity, quantified via CV (i.e. the filtering is less effective in the regions with strong structural information, such as edges or lines, where the structural features are detected based on CV [75, 76]). In this way, image enhancement is allowed while preserving the main morphological information. Later, CV-based adaptive filtering was implemented in ultrasound imaging of breast or thyroid tissue for speckle reduction [77, 78]. Apart from the application of speckle filtering, CV-based homogeneity analysis could also help enhance contour detection of the heart cavity in ultrasound imaging [79] and segmentation of SAR images [80]. While many studies have utilized CV as an intermediate

step (e.g. using CV to form a coefficient function for filtering purposes [77] or define a certain stopping criterion for image segmentation [79, 80]), one study [81] demonstrated the feasibility of analyzing macrophage content shown in the OCT data based on the normalize standard deviation, which is similar in concept to that of CV. In this thesis research, CV is quantified for a certain ROI to indicate regional structural homogeneity and serves as our statistical feature metric.

Optical intensity is related to the CV value, while intensity is highly dependent on the light attenuation. Hence, a simple analytic simulation is run to investigate the impact of spatial frequency, attenuation coefficient, and DC intensity level on the outcome of the CV. Assuming an A-scan intensity profile is $I_{total} = \left(I_{DC} + 0.3 \times \sin\left(kz\right)\right) \times e^{-\mu_t z}$ (where z is the depth), the CV is calculated from the standard deviation and the averaged intensity of the entire A-scan under the following cases: (1) spatial frequency (k) varies, while μ_t and the DC intensity level (I_{DC}) are fixed, (2) μ_t varies, while k and I_{DC} are constant, and (3) I_{DC} varies, while k and μ_t are fixed. Figure 2.3 shows the results of the above-mentioned cases. It is observed that CV decreases at larger k, lower μ_t, and higher I_{DC}, which are the hypothesized conditions of skin undergoing mechanical compression (during compression, a more packed distribution of solid scatterers within the ROI would increase k, and the refractive index matching would cause lower μ_t, and hence higher I_{DC}, as detailed in Section 2.2.1). Therefore, it is hypothesized that the CV value of the compressed sample sites would have a smaller CV as compared to the non-compressed sites.

In the phantom study, the change in CV is evaluated during the compression process to investigate the clustering effect of speckle upon compression. In the human study, the CV at the indented site was compared to that measured at a non-indented site. A ratio of the former over the

latter was used as the metric of interest, where a value closer to unity indicates that a more similar spatial distribution of speckles are observed at both indented and non-indented sites.

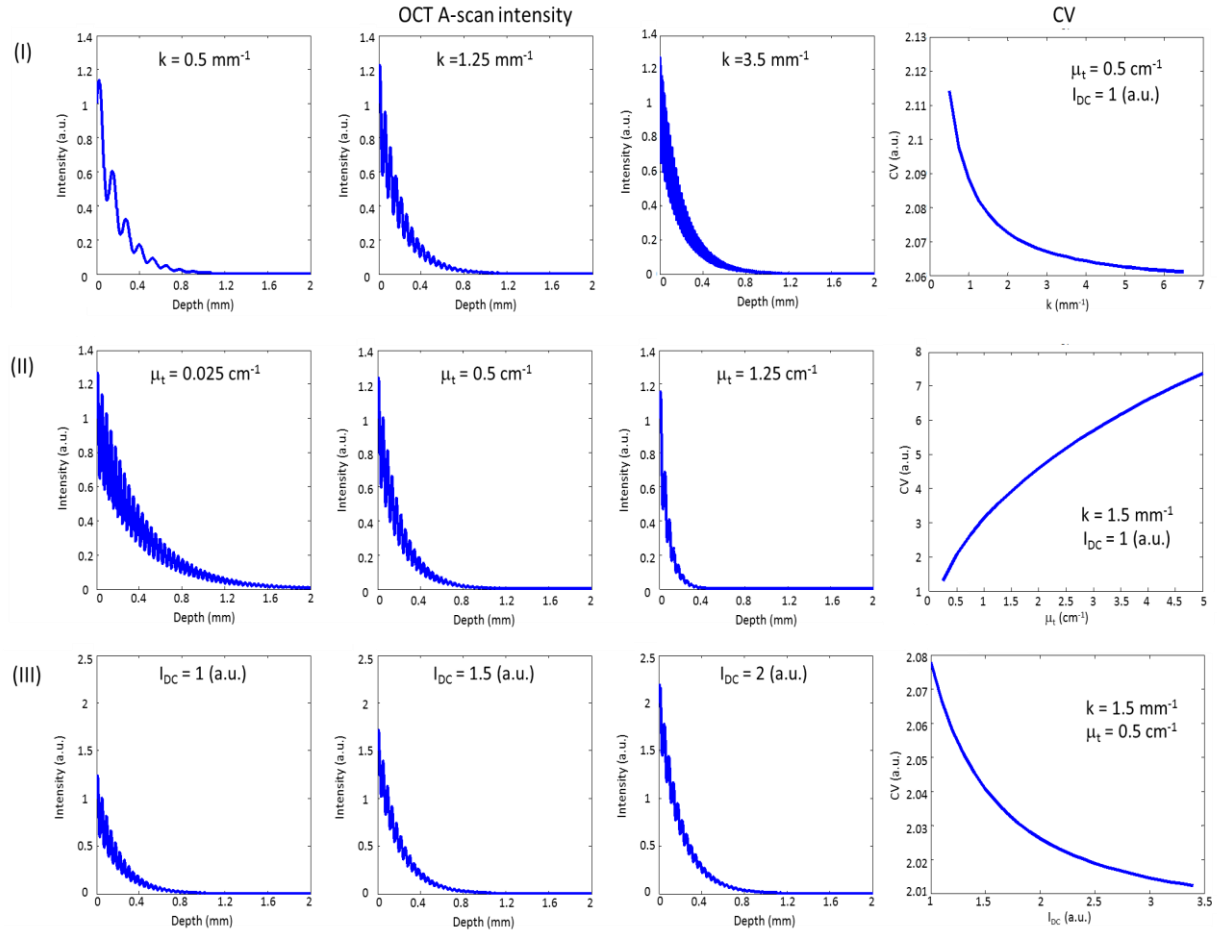

Figure 2.3. Simulation of OCT (Left) A-scan intensity signal and (Right) the correspondent CV under various conditions. (I) With fixed attenuation coefficient (μ_t) and DC intensity level (I_{DC}), the CV decreases as the spatial frequency (k) increases. (II) With fixed k and I_{DC}, the CV increases with increasing μ_t. (III) With fixed k and μ_t, the CV decreases with increasing I_{DC}.

2.2.3 Surface-geometry feature

The third metric is based on the indentation-induced spatial and temporal change of the deformation on the skin, which may be more directly associated with certain biomechanical and

physiological properties. When external loading is applied to skin at a strain greater than 10% and a large deformation is induced, the mechanical response of the skin falls out of the linear regime and exhibits nonlinearity. On the other hand, the history-dependent behavior of the indented skin tissue indicates that the skin is not purely elastic (as are most biological materials). A loaded elastic solid would return to its initial shape almost immediately with an unloading stress-strain curve identical as that of the loading process [82]. In contrast, a loaded plastic solid would be deformed permanently and may be accompanied by material piling-up, which may be related to residual stress [83]. Most biomaterials exhibit some viscoelastic nature, where the deformed specimen would return to the original state over a certain amount of time, while the history-dependent characteristics are associated with the redistribution of fluids inside the tissue. Conventionally, this can be quantified by the viscosity component η based on creep or stress relaxation. In a creep experiment, a constant stress is applied and an increasing strain as a function of time is detected. The creep retardation time can then be extracted, and represents the viscosity to elasticity ratio (η/E) of the medium [84, 85]. Alternatively, one can apply a constant strain and record the decreasing stress over time, where a relaxation time can be characterized and related to η/E [86]. A number of studies have characterized the time-dependent behavior of the edematous and non-edematous tissue and reported significant difference between the two cases, which indicates the fluid dynamics can be reflected in the viscoelastic response [87-89].

However, a viscoelastic model may not be sufficient when considering the complex and heterogeneous nature of the tissue and the physiological factors accompanying the large deformation, such as fluid transport. Embedded with micro-vessels, skin can be modeled as a biphasic material consisting of both solid and liquid, or a poroelastic material [13]. Previous research has aimed to associate fluid flow within the tissue with the deformation, using different

models and assumptions. In vascularized soft tissues, the fluid (e.g. water or interstitial fluid) residing in different compartments can be modelled as different phases, while the resulting formula exhibits a volume change term, linking fluid exchange with tissue deformation [13]. In other studies, poroelasticity can be defined based on strain relaxation, where the resulting strain over time is observed when the sample is loaded with a ramp or constant displacement [19, 90].

In this thesis research, local compression with large strain is applied to *in vivo* skin tissue, and hence it is hypothesized that both fluid translocation and a mechanical response resembling that of a nonlinear poro-viscoelastic material may present. The time-dependent mechanical response is investigated by applying a fixed strain and measuring the residual strains or deformation over time after the indentation process. It is believed that the residual deformation is, at a certain level, coupled with the local fluid dynamics during the post-indentation recovery process. Upon the removal of the indenter, the previously expelled fluids would gradually return to their original location. Since the indenter geometry and the indentation direction were designed so that the highest pressure gradient occurs in the axial direction, the focus is on the change in the axial deformation. It is hypothesized that as a larger volume of fluid returns, the remaining axial deformation would be smaller. In addition, a previous study also revealed a significant difference between the swollen and the normal tissue based on the compression-induced "pit depth" difference between the initial state (immediately after the compression) and the final mechanical equilibrium state (after 800 sec of sustained compression) [87]. Therefore, it is hypothesized that the residual strain obtained right after the removal of the indenter may be associated with not only the elasticity but also the fluid retention level of the skin. Finally, yet importantly, the fact that the analysis is performed merely based on strain indicates that a potentially more cost-effective measurement can be given, where force-sensing related hardware may not be necessary.

2.2.4 Quantification results of tofu phantoms

According to the discussion of the in-tissue parameters at Section 2.2.1—2.2.2, it is hypothesized that under an external mechanical compression, a porous, soft tissue would exhibits an increased optical backscattered intensity and a decreased CV value. To evaluate the hypothesis and performance of the selected metrics, the correlation between compression of a tissue-mimicking phantom and the change in in-tissue metrics was examined. A hydrated tofu sample, with its protein-based and porous-elastic nature similar to soft tissues, is a common phantom for elastic imaging [91, 92] and is utilized here to mimic human skin.

Here, a plastic plate was placed above the tofu sample and served as flat spatially uniform compression source. OCT images were collected at each axial compression step as certain compression displacements were applied. The resulting OCT data were analyzed by calculating the average intensity and the CV within the ROIs. The processing flow is described briefly as follows. First, preprocessing steps removed the duplicated reflections caused by the plastic surface. Sequentially, the phantom surface was allocated by searching for the maximum intensity within 45 pixels (~176 μm) in depth near the initial marked boundary. Finally, all images were aligned according to the surface so that the first row of each image represented the phantom surface. The aligned images were then used for analysis.

In each aligned image, a total of 8 locations were selected to quantify the average intensity and CV values. Each location was 20 pixels (~78 μm) below the phantom surface and 100 pixels (~391 μm) apart from each other in the lateral direction. The window size was 51 pixels (~199 μm) in depth and 102 pixels (~398 μm) in width.

The results reveal the alteration of the average intensity and CV change as the compression displacement increased from 0 to 65 mm with a step size of 5 mm in the axial direction (Figure

2.4). With increasing compression displacement, an increasing trend in the average intensity and a decreasing trend in the CV values was observed, which agree with the stated hypothesis, literature [60], and simulation (Figure 2.3). Therefore, it is suggestive that the intensity-based and CV-based metrics are appropriate indicators for the in-tissue changes under mechanical compression.

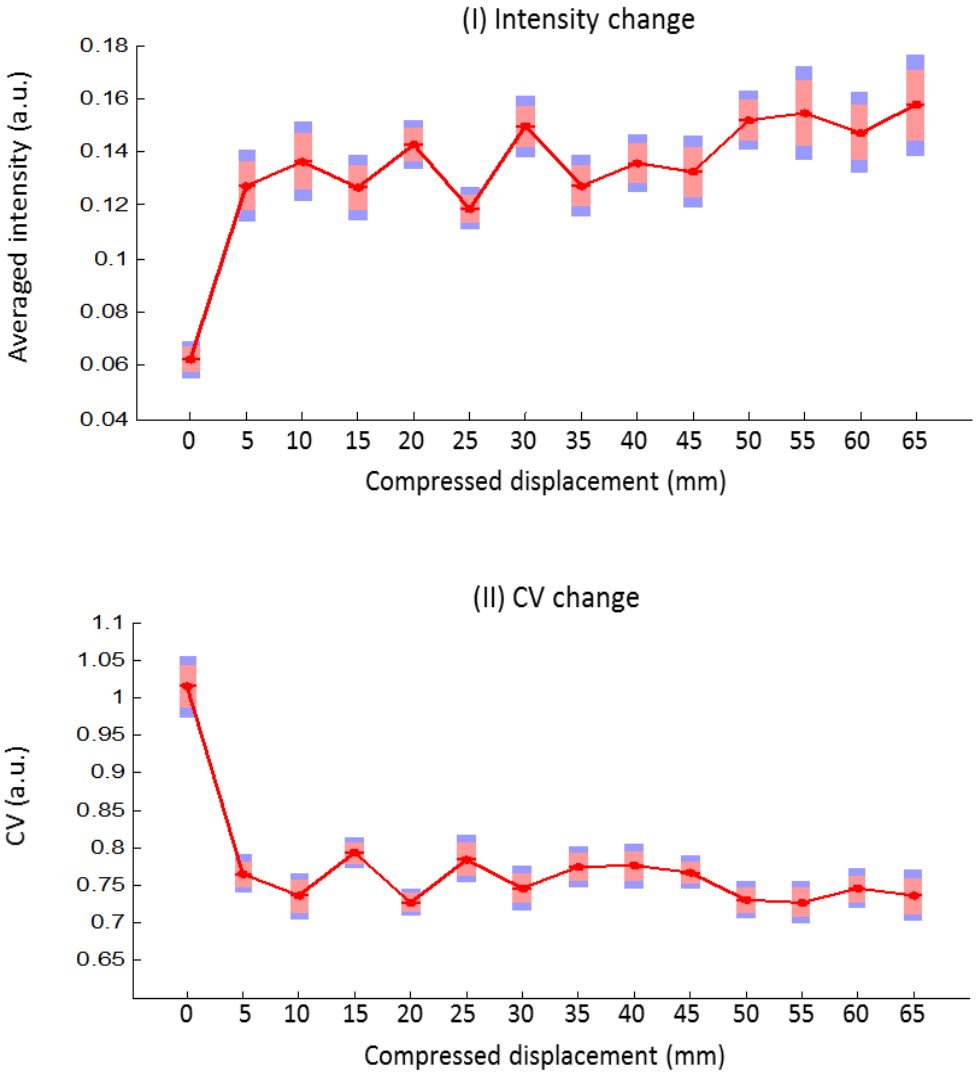

Figure 2.4. Quantitative analysis of a tofu phantom using in-tissue parameters. The results of the change in (I) averaged intensity and (II) CV at the ROIs during mechanical compression are plotted. A total of 8 measurements were performed

at 8 ROIs (N=8), while the red filler circles, the pink box, and the blue box indicate the mean, standard deviation, and 95% confidence interval, respectively.

2.3 Data processing for human subject results

2.3.1 Processing flow description

All human subject data were acquired with the Thorlab Telesto system and software (OCT 3.0.7), where standard OCT imaging processing procedures were performed, including offset subtraction, apodization, k-linearization/FFT, and scaling. After setting the dynamic range (22-63 dB), the image was then saved as an 8-bit grey scale image. These images were then used as the input for further metric extraction, where Matlab (R2013b, MathWorks, Natick, MA) was used as the imaging processing tool.

Regions of interest (ROIs) selected for the analysis of the in-tissue dynamics (e.g. intensity-based and statistical-based features) were at the dermal layer, where the collagen meshwork and elastin fibers were located. In contrast, the geometric-based parameter was quantified based on the deformation measured at the skin surface. To be more specific, the surface deformation at the center of the indentation site was utilized for quantification.

The data processing flow includes the pre-processing and the main data analysis based on the three metrics proposed. A general overview of the processing procedure is shown in Figure 2.5.

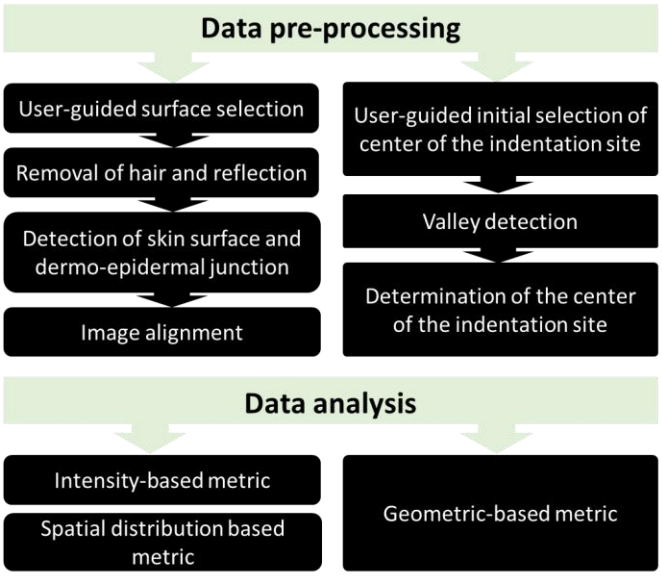

Figure 2.5. Data processing procedure, including the main steps for data pre-processing and the proposed metrics for data analysis.

2.3.2 Data pre-processing

Data pre-processing is a necessary step prior to the main processing and analysis in order to avoid partially non-indicative structural features and the presence of eventual outliers in data analysis. Correction for image artifacts and image alignment was the main goal of pre-processing. Since artifacts can be caused by the inevitable human subject motion and unremoved skin hair, image alignment in the axial and lateral directions are required to correct for skin surface incline and to determine the center of the indentation position, respectively. Note that the location of the indentation site is important in this analysis since this approach compares the dynamics under the indented sites with the non-indented sites.

Four major steps for artifact removal and image alignment was included in the pre-processing steps, namely (1) user-guided initial skin boundary selection, (2) removal of hair features and reflection artifacts, (3) detection of the dermo-epidermal junction (DEJ), and (4) image alignment.

(1) User-guided initial surface boundary selection

The very first step is to define the initial surface boundary (S_i) at the location close to but above the skin surface. This initial boundary is important in this algorithm for two reasons. First, most of the artifacts to be remove (such as any strong reflection and any presence of skin hair) could result in an outlier of the morphology information located above the skin surface. Second, the image alignment was performed after the segmentation of the epidermis and dermis regions, where the initial estimation of the dermo-epidermal junction (DEJ) depends on the location of the skin surface. Therefore, the initial boundary defined at the skin surface (or somewhere close to it) can be utilized as a reference line for sequential data pre-processing steps.

Numerous algorithms have been proposed to detect the skin surface and segment the skin layers, such as binary thresholding [93], thresholding and polynomial fitting after locating the maximum intensity [94], morphological dilation and erosion based on binary images [95], a shapelet decomposition algorithm [96], regularized short-path extraction [97], and morphological filtering after detecting the high gradient pixels of the B-scan images [98]. However, most approaches are either supervised, suitable only for a certain type of images, or computationally expensive [57]. On the other hand, manual marking of the tissue boundary, though more user-dependent, has still been applied in OCT data analysis [57] or served as the "validation" group for computationally segmented results [98]. Here, a simple user-guided border detection is applied. An example of the user-defined S_i above the skin surface used in this study is shown in Figure 2.6.

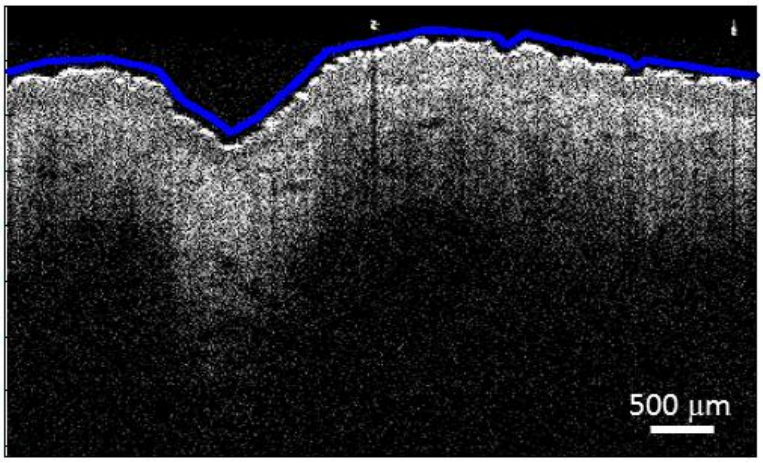

Figure 2.6. OCT image of skin and illustration of the user-defined initial surface boundary. The OCT image is acquired from the skin of an adult at 0 min after indentation. The user-defined initial surface boundary S_i is shown as the blue line.

(2) Removal of hair features and reflection artifacts

The highly reflective hair present on the skin surface may cause shadowing of the skin tissue beneath. In some datasets, there exist strong reflection artifacts originating from the mismatch between the refractive index of the air and the skin. Although index-matching agents, such as glycerol, are known to be effective in reducing surface reflections and artifacts in human skin [99, 100], they were not incorporated in our study for several reasons. Fluid content within the skin may increase with the uptake of glycerol. The potential for an increase of water absorption (from the air or deeper skin) exists, given that the glycerol is a hydrophilic humectant [100]. Since glycerol diffusion happens on the same time scales as these experiments (a few minutes) [99-101], this extrinsic factor not only could influence the intrinsic fluid volume but also the fluid dynamics (and even the biomechanical properties) in the skin during the experiment. In addition, the presence of glycerol may reduce the friction on the skin, and further affect the position stability of the indenter or the pressure applied during the indentation.

Instead, most of the morphological artifacts are removed using computational approaches. Here, a binary thresholding approach, modified and improved, and based on one previously described and implemented [93], was used where the preservation of each A-line was determined based on intensity thresholding. In each lateral location (x), the average intensity of the A-line ($\bar{I}_{A-line}(x)$) was calculated within an array range (ROI_{A-line}) of 35 pixels above the initial boundary $S_i(x)$. Sequentially, $\bar{I}_{A-line}(x)$ was compared to the threshold value ($I_{Thershold}$) as follows: If $\bar{I}_{A-line}(x) > I_{Threshold}$, the A-line is discarded; otherwise, the A-line is preserved.

The selected threshold $I_{Thershold}$ depended on the intensity distribution across an "air ribbon" two dimensional region (ROI_{Air}) at 15 pixels above S_i. It is determined by:

$$I_{Thershold} = I_{Interquartile} + I_{y_{th}-percentile}, \tag{2-4}$$

where $I_{Interquartile}$ and $I_{y_{th}-percentile}$ are the interquartile range and the y-th percentile intensity at the ROI_{Air}, respectively. Based on a fuzzy-logic-like filtering approach, the percentiles for $I_{y_{th}-percentile}$ can be decided as

$$y_{th} = \begin{cases} 100_{th}, & \text{if } I_{Max,\text{Air}} < 50\%\ I_{Max,\text{B-scan}} \quad \text{(No artifacts)} \\ 90_{th} \text{ or } 95_{th}, & \text{if } I_{Max,\text{Air}} > 50\%\ I_{Max,\text{B-scan}} \text{ and } \bar{I}_{\text{Air}} < 10\%\ I_{Max,\text{B-scan}}, \\ 75_{th}, & \text{if } I_{Max,\text{Air}} > 50\%\ I_{Max,\text{B-scan}} \text{ and } \bar{I}_{\text{Air}} > 10\%\ I_{Max,\text{B-scan}} \end{cases} \tag{2-5}$$

where $I_{Max,\text{Air}}$ is the maximum intensity of the ROI_{Air} region, $I_{Max,\text{B-scan}}$ is the maximum intensity of the entire B-scan image $I_{Max,\text{B-scan}}$, and $\bar{I}_{Air}$ is the averaged intensity at ROI_{Air}. As the $\bar{I}_{Air}$ value increases with more hair/reflection artifacts, a lower

percentile can be used for thresholding. An illustration of the images before and after the removal of hair and reflection artifacts is shown in Figure 2.7.

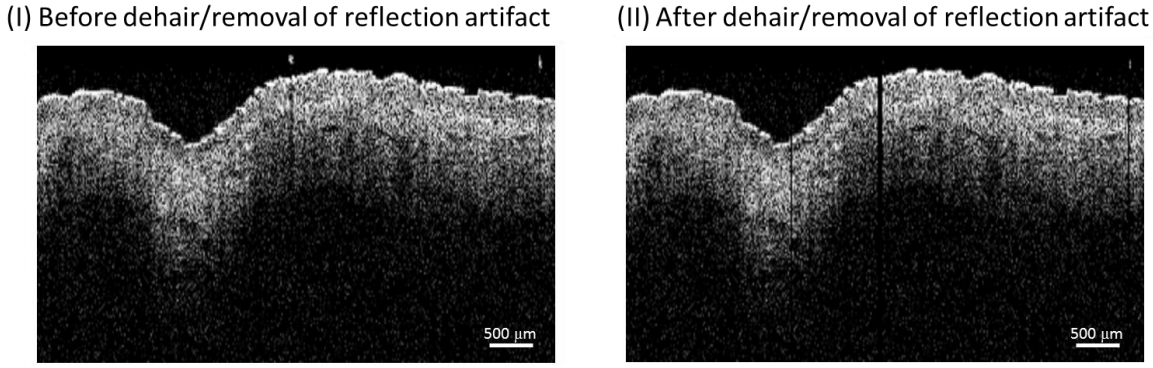

Figure 2.7. Illustration of the effect of hair and reflection artifact removal. The OCT skin images from a human adult at 0 min after the indentation are shown for (I) before and (II) after removing the image artifacts caused by the presence of skin hair.

(3) Detection of dermo-epidermal junction (DEJ)

The detection of the dermo-epidermal junction (DEJ) was performed after estimation of the skin surface (S_{Skin}), which is defined by locating the maximum intensity along the depth range from $S_i - 20$ to S_i at each lateral location. For the pre-indentation datasets, the initial estimation of the DEJ (DEJ_i) is determined by $S_{skin,smoothed} + d$ (positive sign indicates deeper area), where $S_{skin,smoothed}$ is the result after moving average filtering S_{Skin} (window size: 10 pixels) and d is the axial distance between $S_{skin,smoothed}$ and a user-defined point located close to the DEJ region. In terms of the post-indentation datasets, DEJ_i at the indented site ($DEJ_i(\mathrm{x}_{Indented\ Site})$) was determined by $S_{skin,smoothed} + d_{indented}$, where $d_{indented}$ is the axial distance between $S_{skin,smoothed}$ and another user-defined point at the DEJ location (within the lateral range of the indented site, which shows a much reduced epidermis thickness). Sequentially, the maximum intensity was located within

a depth range ($DEJ_i - 5$ to $DEJ_i + 5$) and defined as DEJ_i'. A moving averaging filter (window size: 20 pixels) was then performed on DEJ_i' and defined as the final form of DEJ. In Figure 2.8, an example of the final results of S_{Skin} and DEJ are provided.

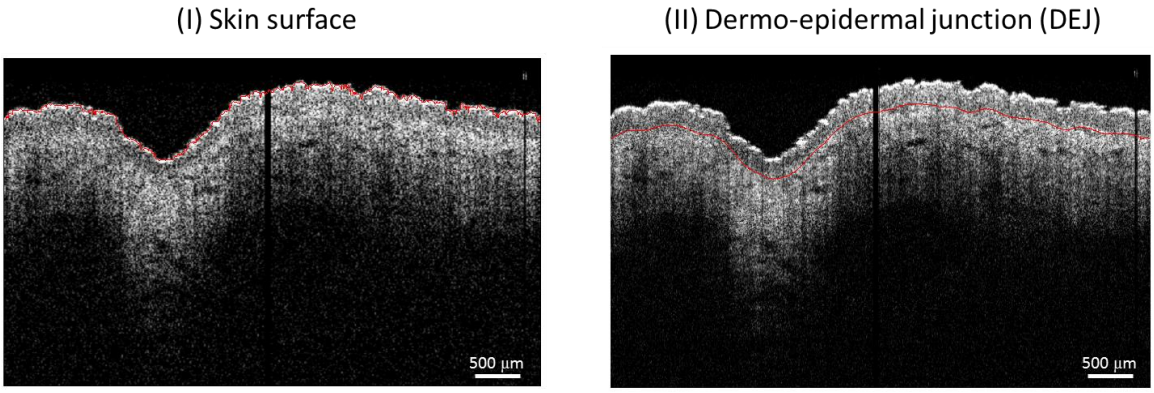

Figure 2.8. Visualization of the boundary detection on OCT skin images. (I) The skin surface (S_{Skin}) and (II) dermo-epidermal junction (DEJ) are represented with red lines in structural OCT images shown, respectively.

(4) Image alignment

As mentioned earlier, this study focused on the indentation-induced alteration within the dermis, and hence the images were flattened and aligned according to DEJ, which was defined in the previous step. The aligned result is illustrated in Figure 2.9.

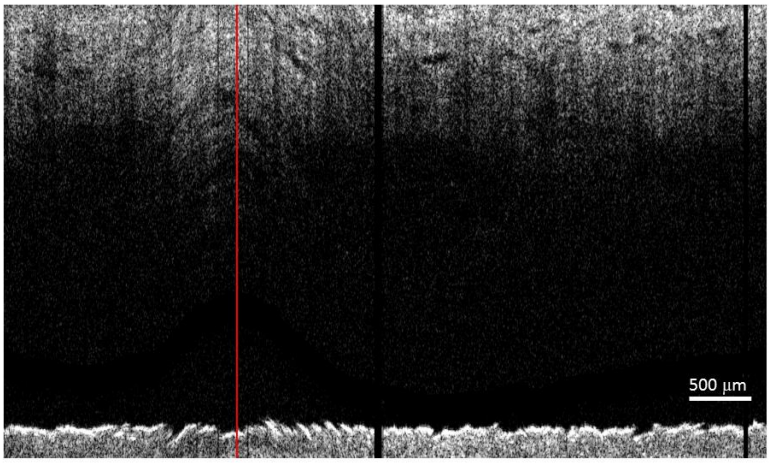

Figure 2.9. Aligned OCT image. The indented skin image was aligned by flattening the image according to the defined DEJ.

Apart from artifact removal and image alignment, the center of the indentation site, in the lateral direction, was also determined. The processing steps are illustrated in Figure 2.10 and are detailed as follows. First, initial selection of the indentation sites ($x_{indented,\,i}$) was decided manually. Afterward, valley detection was performed at the lateral range from $x_{indented,\,i} - 256$ to $x_{indented,\,i} + 256$ on the detrended $S_{skin,smoothed}{}'$ (obtained from moving averaging filtering of S_{skin} with a window size of 40 pixels). The detected valley was then recorded as the center of the indented site of the skin image ($x_{indented}$). In the in-tissue quantification parameters, $x_{indented}$ was used to decide the "indented site" parameters, as opposed to the surrounding "non-indented site" parameters. As for the geometrical-based quantification metric, the skin residual deformation distance was calculated at $x_{indented}$.

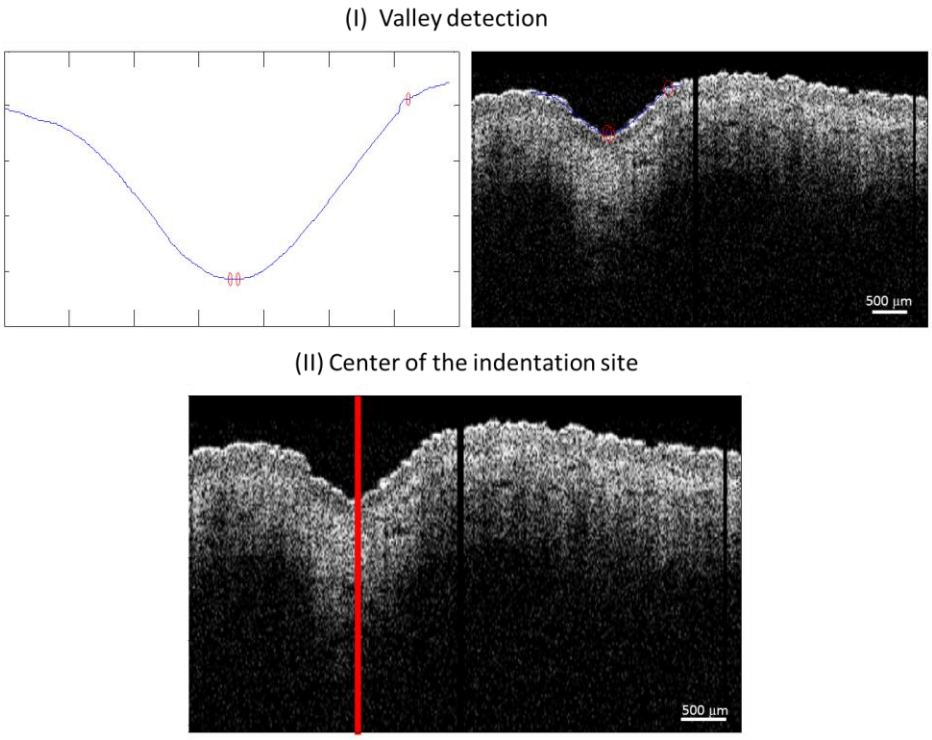

Figure 2.10. Detection of the center of the indented site. (I) Illustration of the valley detection at the lateral ROI. (II) Determination of the final selection of the center of the indentation site, which is indicated with a red line.

2.3.3 Data analysis procedure based on the selected metrics

After the pre-processing steps, the data analysis becomes straightforward. Based on the defined metrics for quantification (both in-tissue features and surface geometry), the processing procedure can be grouped as the following two types.

(1) In-tissue parameters: intensity ratio and coefficient of variation (CV) ratio

For the in-tissue metrics, the aligned images were used for quantification, which allows all quantification to be performed at the same depth range within the dermis. Since there is interest in comparing the quantitative values obtained at the indented site with those from the non-indented site, the characterization can be described using a ratio. Therefore, the metrics used for intensity-based and spatial-distribution-based quantification are:

$$\text{Intensity ratio} = \frac{I_{indented}}{I_{non-indented}} \tag{2-6}$$

$$\text{CV ratio} = \frac{CV_{indented}}{CV_{non-indented}}. \tag{2-7}$$

The lateral range of the indented site was chosen from $x_{indented} - 34$ to $x_{indented} + 34$ (~400 μm width), where $x_{indented}$ is the center of indentation site as defined in the pre-processing step. The lateral ranges ($lateral\ range_{1,2}$) of the two non-indented sites, on the other hand, were selected from $x_{non-indented} - 34$ to $x_{non-indented} + 34$, where the center locations are $x_{non-indented,\ 1,\ 2} = x_{indented} \pm 145$ (~850 μm width). The window size selected for all ROIs was the same, which is $window = 400\ \mu m \times axial\ range$. The lateral range was fixed at 68 pixels (~400 μm), however the axial range is a variable that is a function of the initial indentation displacement ($D_{indentation}$) applied on each subject (note that the applied strain was fixed, but not the displacement, and hence the displacement would vary with the circumference of either the forearm or the thigh of each subject). The physical depth of the axial range was selected to be $axial\ range = 250\ \mu m \times \frac{D_{applied\ indentation}}{1\ cm}$, where $D_{applied\ indentation}$ of the adult forearms and that of the infant thighs fell in the range of $0.54 - 0.72\ cm$ ($axial\ range = 28 - 47\ pix$) and $0.64 - 0.76\ cm$ ($axial\ range = 33 - 39\ pix$), respectively. The axial range of the collected datasets was designed to be limited to 250 μm, a region where single scattering dominates [102]. In both parameters, the non-indented site values were represented as an average of the values of the two non-indented ROIs (i.e.

$$I_{non-indented} = \frac{I_{(lateral\ range_1,\ axial\ range)} + I_{(lateral\ range_2,\ axial\ range)}}{2}$$,

$$CV_{non-indented} = \frac{CV_{(lateral\ range_1,\ axial\ range)} + CV_{(lateral\ range_2,\ axial\ range)}}{2}$$). An illustration of the ROIs selected at the indented sites and the two non-indented sites can be seen at Figure 2.11.

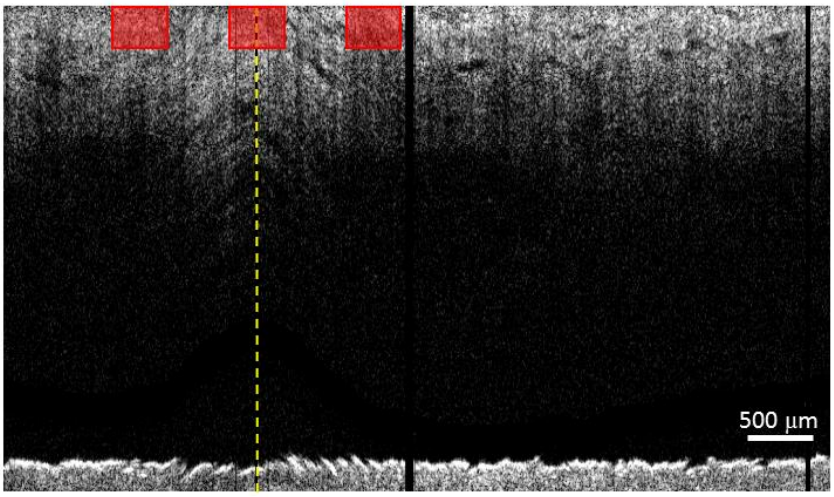

Figure 2.11. Illustration of the ROIs for in-tissue parameter quantification. The characterizations are performed on an aligned image, where the red boxes indicate the windows at the indented (center) and the two non-indented (side) sites. The yellow dashed line indicates the center location of the indented site ($x_{indented}$).

(2) Skin surface geometry parameter: residual deformation percentage (RD %)

The residual deformation percentage (RD%) was quantified by the deformation that remained on the indented site ($x_{indented}$, as defined in the pre-processing steps), followed by a normalization with respect to the initial deformation applied, as shown in the following equation

$$\text{Residual deformation } \% = \frac{D_{residual}}{D_{applied\ indentation}} \times 100\%. \quad (2\text{-}8)$$

Here, the residual or remaining deformation ($D_{residual}$) was obtained at $x_{indented}$ by measuring the distance from the skin surface to the average height of the two piled-up

peaks immediately adjacent to the indented site. Knowing $x_{indented}$, peak detection was sequentially performed at the two neighboring regions, each having a lateral range of 256 pixels (~1.5 mm in width). Note that RD % should only be a scaling factor different from the residual strain since the initial strain applied in each subject is fixed. An illustration of $D_{residual}$ quantification at $x_{indented}$ is shown in Figure 2.12.

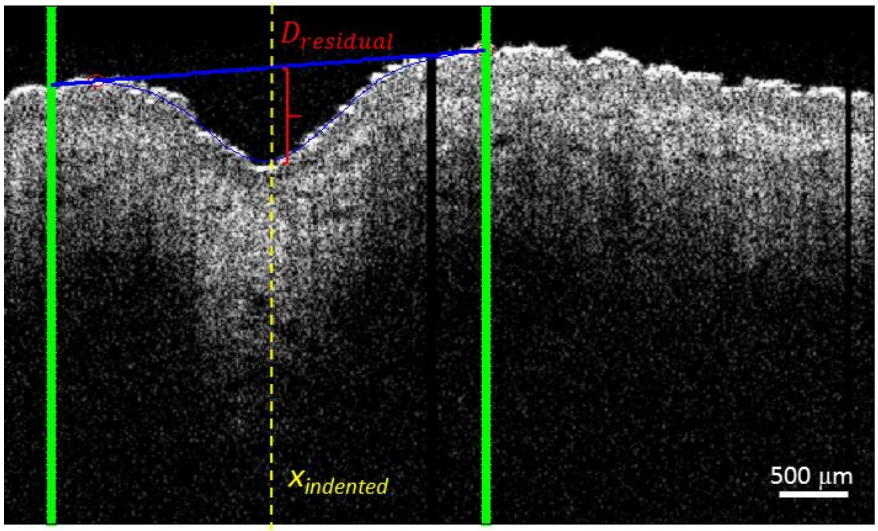

Figure 2.12. Quantification of the residual skin surface deformation ($D_{residual}$). $D_{residual}$ is quantified at the center of the indented site ($x_{indented}$, the yellow dashed line), measured as the distance between the height of the skin surface and the average height of the two "piled" peaks (the two hollow red circles). The two piled-up peak locations were detected within the lateral range from $x_{indented}$ to $x_{indented} \pm 256$ (the green lines), respectively.

2.4 Results of human subjects

The quantitative results of the human subjects (of both adults and infants) is discussed in this section, where the results from the adult forearm and the infant thigh are discuss separately, followed by a comparison between the two groups.

2.4.1 Results from the adult forearm

Here, the in-tissue results from the adult forearm datasets are given in Figure 2.13. Comparing the results from before indentation with those right after the removal of the indenter

(at 0 min), an increase in intensity ratio (p-value <0.01) is observed, indicating the average intensity at the indented site is larger than that of the non-indented sites, which agrees with the stated hypothesis. Plotting the recovery trend with a time interval of 1 min, a trend of fluctuating intensity ratios is shown, rather than a clear increase or decrease. On the other hand, a decreased CV value is observed right after indentation, as compared to the before-indentation scenario (p-values < 0.05), implying that the CV of the indented site is less than that of the non-indented sites, possibly due to the more homogeneous pattern caused by localized loading. From the post-indentation data, again, no clear trend is observed for the CV ratio. For both in-tissue parameters, the 0-min post-indentation cases show a significant difference as compared to the pre-indentation cases, and no apparent change is seen from the first 5 min after the release of the localized loading. This is suggestive that the fluids and the deformable tissue components have negligible recovery within the 5 min post-indentation period.

Similar plots are shown for the RD % (Figure 2.14), which describes the skin surface geometrical change. Here, an existence of RD % is observed immediately after the removal of the indenter, indicating a delayed re-bound of the skin. During the post-indentation period, a decreasing RD% is observed, indicating that the deformed skin is gradually recovering toward its mechanical equilibrium and shape (a flat skin surface).

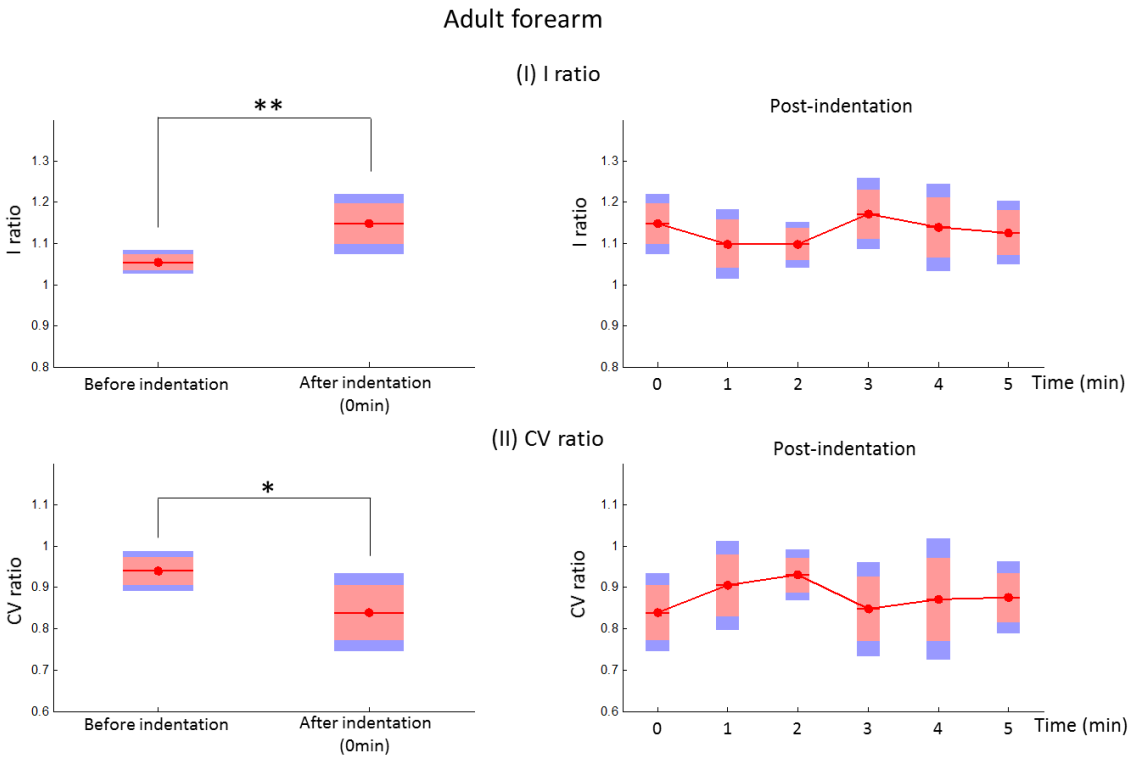

Figure 2.13. In-tissue parameters for adult forearm skin. (I) Intensity ratio and (II) CV ratio results for (left) before and immediately after indentation, and for (right) 0-5 min post-indentation. The red line, pink shading and blue shading indicate the mean, 95% confidence interval, and one standard deviation, respectively. * and ** indicate a p-value less than 0.05 and 0.01, respectively. Sample size N=8.

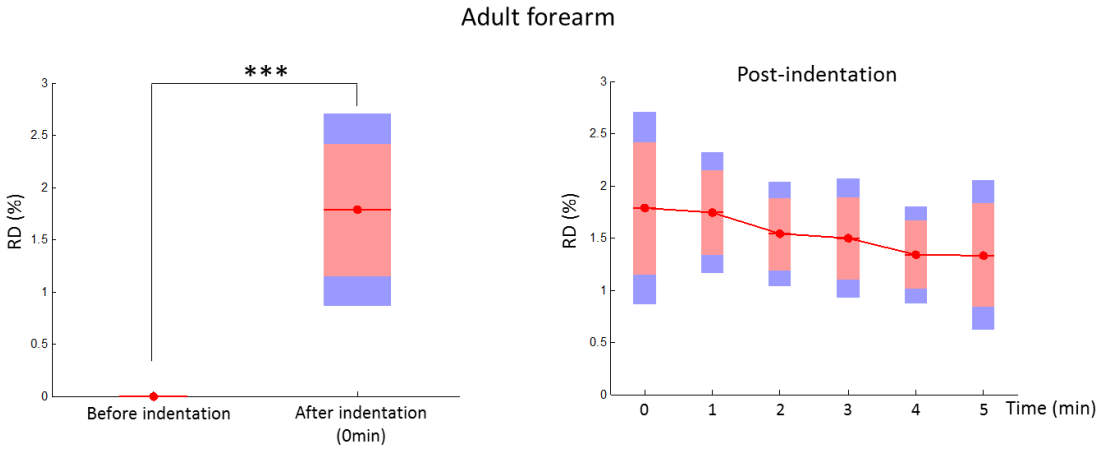

Figure 2.14. Residual deformation percentage (RD%) of adult forearm skin. (Left) Before and immediately after indentation and (right) 0-5 min post-indentation. The red line, pink shading and blue shading indicates the mean, 95% confidence interval, and one standard deviation, respectively. * indicates a p-value less than 0.001. Sample size N=8.**

A summary of the changes in the three parameters (i.e. the intensity ratio, the CV ratio, and the RD%) is illustrated using a three-dimensional scatter plot, and the alterations of the in-tissue parameters are plotted in two-dimensions (Figure 2.15). The before and after indentation periods show strong differences for all three parameters, and the trend of changes agree with the hypothesis. The intensity ratio is observed to be inversely related to the CV ratio. However, it is worth emphasizing that the two metrics represent different meanings, i.e. one focuses on the amplitude change of backscattered light signal and the other describes the sparseness of the scatterers.

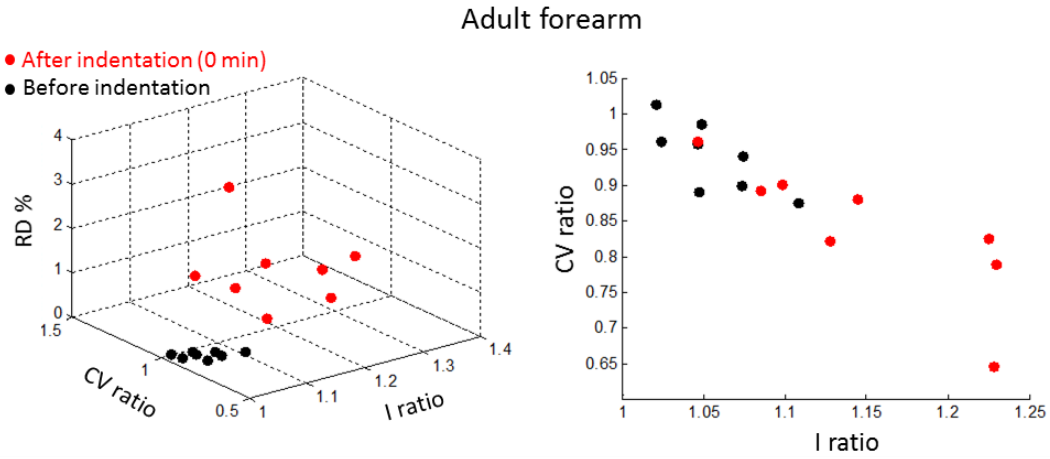

Figure 2.15. Summary of the adult forearm results. (Left) Scatter plot comparison of the in-tissue and skin surface parameters. (Right) Comparison of the intensity ratio and the CV ratio before (black circles) and 0 min after indentation (red circles).

2.4.2 Results from the infant thigh

Similar figures for the in-tissue and skin surface parameters are plotted for the infant thigh datasets (Figure 2.16 and Figure 2.17). Again, after the release of the indenter, the intensity ratio increased (p-values < 0.01) and the CV ratio decreased (p-values < 0.01). Within the first 5 min period after indentation, the intensity ratio and CV ratio both returned toward unity, showing obvious recovery trends. This may indicate a combined result of displacement recovery from elastic solids and fluid redistribution over time, reflecting the viscoelastic nature of skin. However,

it is also observed that both the intensity ratio and the CV ratio do not return completely to the initial values, suggesting that mechanical equilibrium has not yet been reached in 5 min.

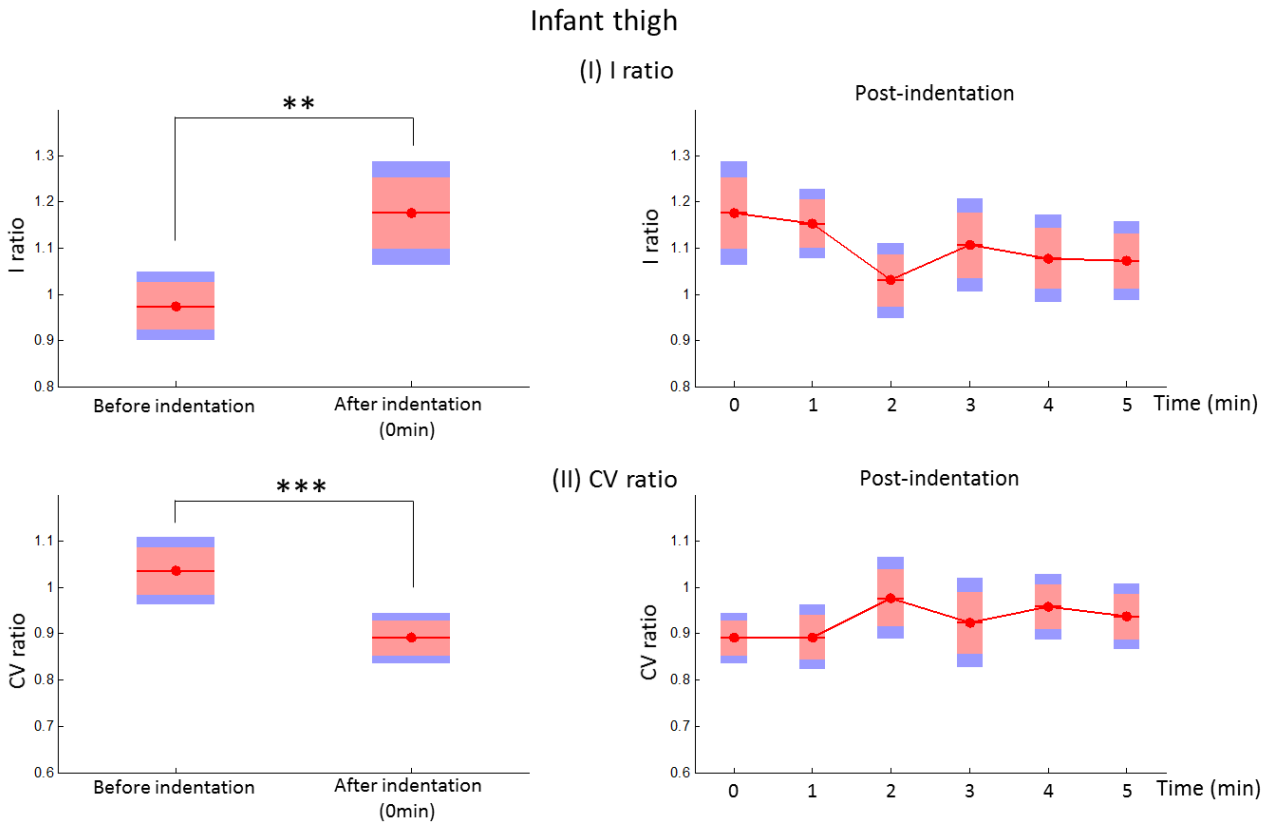

Figure 2.16. In-tissue parameters of infant thigh skin. (I) Intensity ratio and (II) CV ratio results for (left) before and immediately after indentation, and (right) 0-5 min post-indentation. The red line, pink shading and blue shading indicate the mean, 95% confidence interval, and one standard deviation, respectively. ** and * indicate a p-value less than 0.01 and 0.001, respectively. Sample size N=8.**

In addition, a non-zero surface residual deformation is also observed after indentation in the infant thigh datasets, and this value decreased (toward 0%) over time (Figure 2.17).

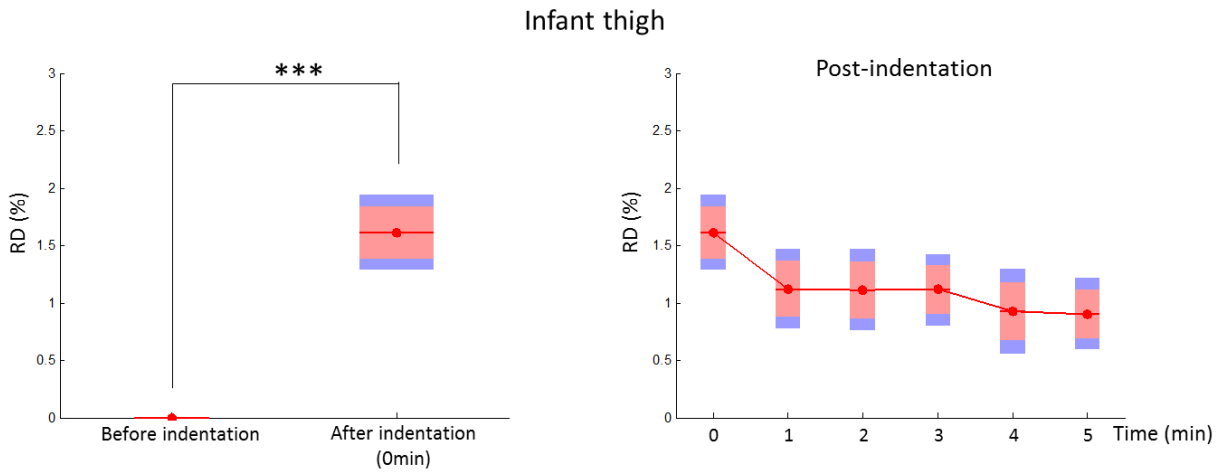

Figure 2.17. Residual deformation percentage (RD%) of infant thigh skin. (Left) Before and immediately after indentation, and (right) 0-5 min post-indentation. The red line, pink shading and blue shading indicate the mean, 95% confidence interval, and one standard deviation, respectively. * indicates a p-value less than 0.001. Sample size N=8.**

According to the three-dimensional scatter plot, a difference in the before and the after indentation periods is shown. Again, there is an apparent difference between the two datasets, where the post-indentation data show an existence of residual deformation, higher intensity ratio, and lower CV ratio. An inverse relationship between the intensity ratio and the CV ratio is shown as well.

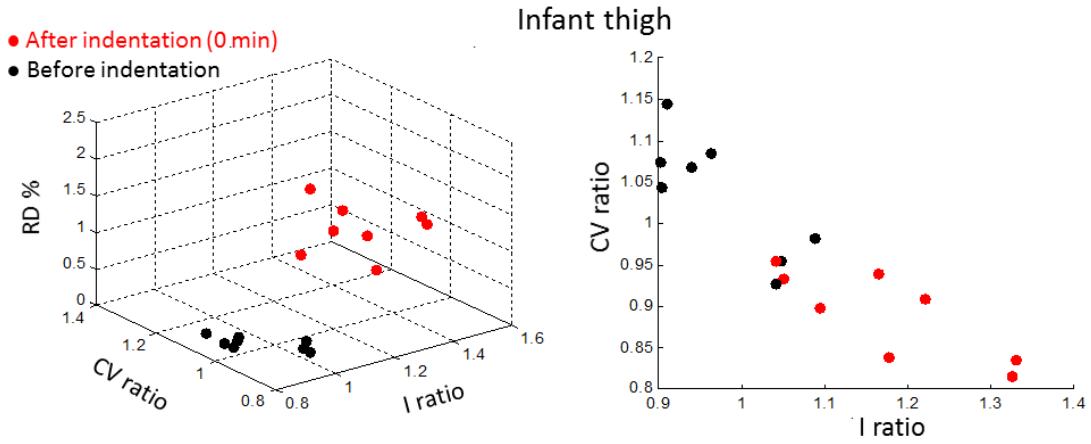

Figure 2.18. Summary of the infant thigh results. (Left) Scatter plot of the in-tissue and the skin surface parameters comparison, and (Right) comparison of the intensity ratio and the CV ratio before (black circles) and 0 min after indentation (red circles).

2.4.3 Inter-group comparison

Some similarities and some variations can be found when comparing the results from the adult forearm with the infant thigh groups (Figure 2.19). Similar trends for the three metrics under the pre- versus post-indentation cases are shown in both groups, indicating the remaining effect of the localized compressive force on both types of skin tissues, even upon the release of the external force. However, a larger difference of in-tissue parameters between the pre- and post-indentation sets is revealed in the infant group, and the RD% of the infant skin is lower than that of the adult.

Since an infants' upper reticular dermis contains collagen that is thin and less dense (sparse) [28], with a potentially higher fraction of ECF, mechanical compression would lead to a greater increase in volume density of scatterers (e.g. collagen fibers), and therefore a higher intensity and CV contrast between the indented and the non-indented sites. In contrast, the adult skin normally has a dense collagen network, and hence the contrast induced by mechanical compression may not be as large. However, the RD% of the infant is lower than that of the adults. This may suggest that the skin rebound is faster in an infant and that the in-tissue metrics are able to show differences, although there is less deformation retained in the infant skin. It is hypothesized that this may also be related to the dynamics of the fluids constituents (e.g. ECF or ECM without the fibrous structural proteins). Since the infant skin may have a larger degree of hydration (although mostly observed in the stratum corneum [27]) and a larger content of the fluid components (as compared to the solid fibers), a small deformation could displace a larger amount of fluid, which can be reflected by the contrast shown in the in-tissue parameters.

As the recovery trend of the two groups is compared, an obvious trend in both the in-tissue parameters (toward unity) and in the skin surface parameter (toward 0% residual deformation), is only exhibited in the infant thighs. On the other hand, the in-tissue parameters from the adult post-indentation periods show values fluctuating around the 0-min value throughout the first 5 min; the surface RD% decreases slowly during recovery. These imply that a faster in-tissue recovery mechanism occurred in the infant skin, which may possibly be a result of a faster return of the

expelled fluids, sufficient and responsive blood supply to the deformed site, or a faster restoration of shape of the solid components in the skin. The post-indentation recovery results were measured within 5 min, which is an arbitrarily chosen experimental period. However, none of the data indicates that the skin has returned to mechanical equilibrium during the 5 min recovery process. Therefore, in the future, an experimental time can be extended to beyond 5 min in order to provide a more complete temporal characterization of the recovery kinetics.

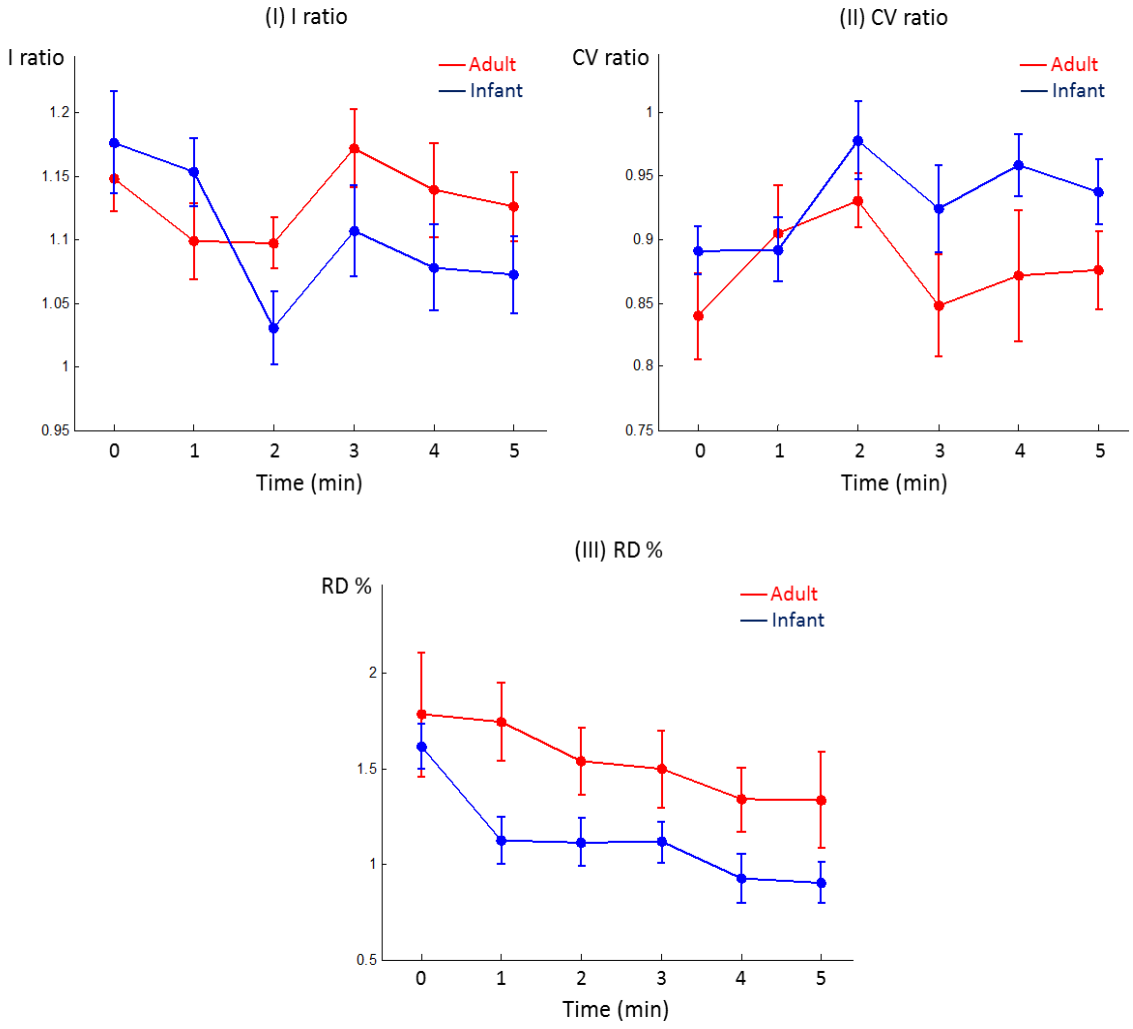

Figure 2.19. Comparison of the adult forearm (red) and the infant thigh (blue) results for (I) intensity ratio, (II) CV ratio, and (III) residual deformation percentage at 0-5 min post-indentation. The error bars indicate standard error of the mean. N=8 for both adult and infant data.

2.4.4 Intra-group comparison

In this section, other physiological factors are introduced and an intra-group comparison is performed. In the adult group, the influence of the subjects' age and body mass index (BMI) is investigated, relative to the indentation results. Shown in Figure 2.20 (upper row) are the results for pre- and 0-min post-indentation results for all adult subjects, sorted by age. The younger adults (age 20-28 yr) show a less dramatic change after indentation for the in-tissue parameters (i.e. the intensity and CV ratios) as compared to the older adults (age 30-33 yr). This is likely due to the reduced amount of ECF in the older skin [25], where less mechanical support is provided, and hence the alteration in the aged skin remains longer after the release of loading. Within the younger subgroup, no significant variation was found with respect to BMI. However, in the older subgroup, larger pre- and post-indentation changes are seen in the individuals with a BMI < 30. It is hypothesized that this is related to the amount of supporting tissue with higher mass density, such as muscle. In terms of RD%, one can see a higher average for the younger subgroup as compared to the older subgroup. This may be associated with the increased rigidity and decreased extensibility of the aged skin [24]. Interestingly, though, within each group, an increasing trend of RD% is shown with increasing age.

Regarding the infant skin data, the indentation results are compared based on the age. However, there is no clear trend observed for a conclusive discussion. This is likely due to the large bio-variation among each individual infant, since the skin (at least with the first year of infancy) is still undergoing significant maturation processes [27].

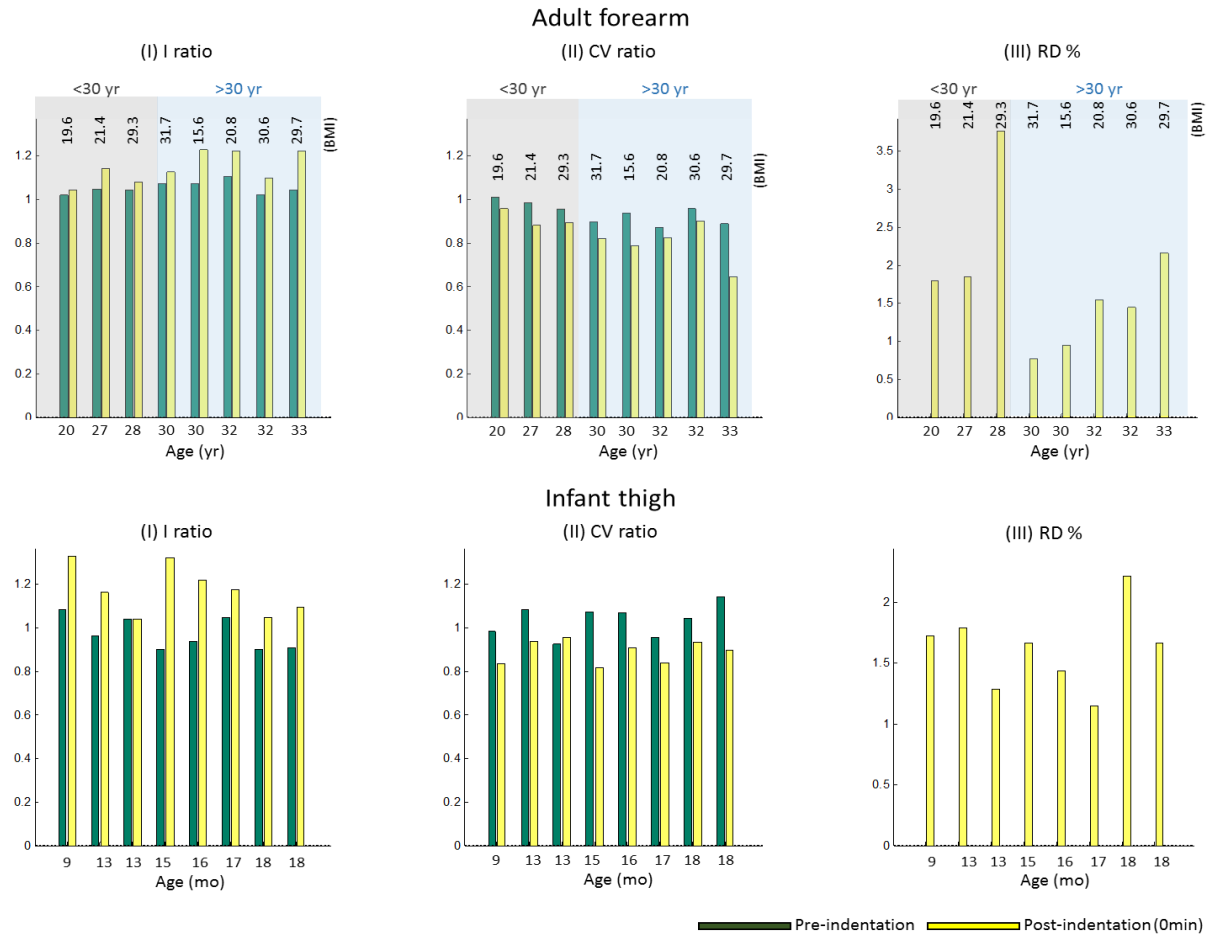

Figure 2.20. Intragroup comparison for (upper row) adult forearm and (lower row) infant thigh skin for (I) intensity ratio, (II) CV ratio, and (III) residual deformation percentage. The green and yellow bars indicate pre- and post- indentation (at 0 min), respectively. In the (upper row) adult data, the grey and blue shading indicates the subgroups with ages less than and above 30-years-old, respectively. The BMI values are noted on the charts as well.

2.4.5 Other parameters

Other than the above-mentioned metrics, analysis was also performed based on the lateral intensity profile at different depths. When indenters with different geometric shapes were applied, the FWHM of the lateral intensity profile (using Gaussian fit) at different depths also exhibited geometric-dependent features. Shown in Figure 2.21 are the lateral intensity profiles of the skin indented by an indenter tip with a triangular or square cross-section. A gradient of the FWHM in depth is observed from the triangular cross-section, while the values remain almost the same in depth for the square cross-section. This is possibly due to the variation of stress along the

transverse direction, which results in a geometry-related stress distribution, and hence the deformation. This preliminary data has shown the potential for lateral fluid translocation or shear strain characterization in the future.

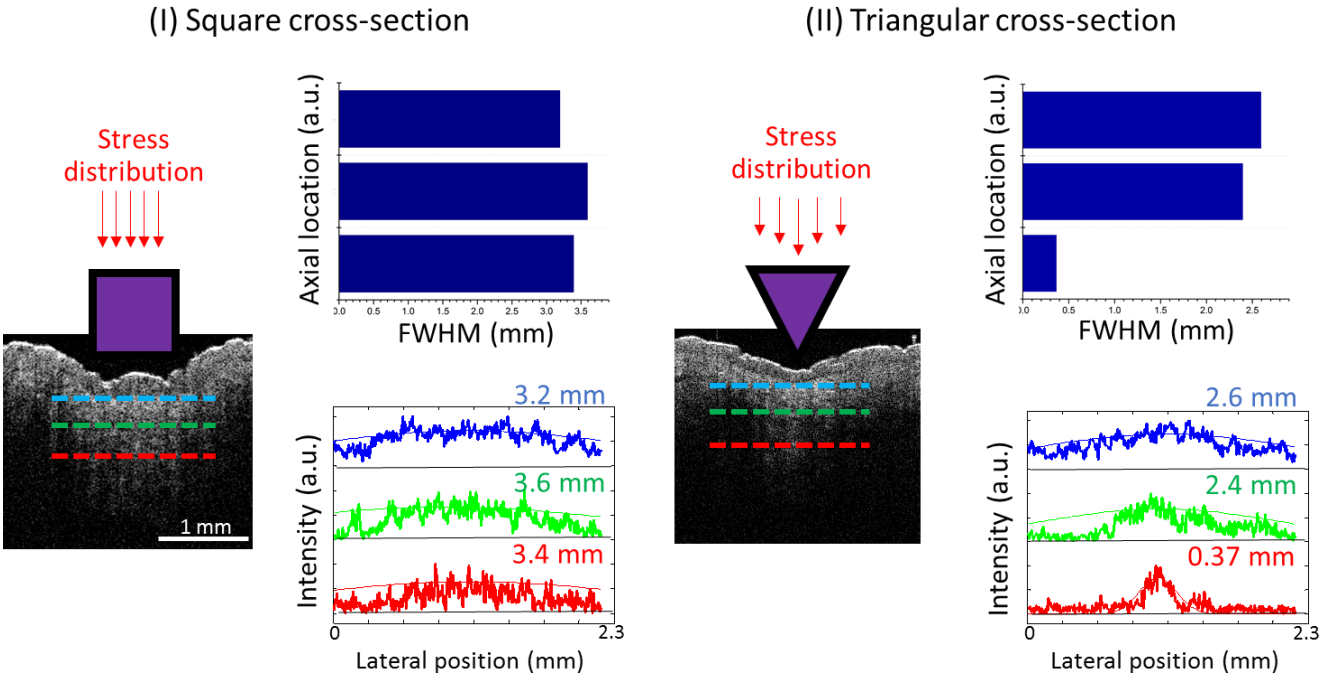

Figure 2.21. OCT image and lateral intensity profile of the skin tissue indented by an indenter with a (I) square cross-section and a (II) triangular cross-section. In the intensity plot, both the intensity profile and the Gaussian fit curve are shown, where the blue, green, and red colors correspond to signals obtained from the depths indicated with the blue, green, and red dashed lines in the OCT image, respectively.

3 Characterization of viscoelastic properties of human skin

Up to this point, this thesis has presented quantitative analyses of *in vivo* human skin to characterize the effect of mechanical indentation. Here, this investigation is extended to include the contributing factors to the biomechanical response of skin. Based on assumptions and experimental observations, the viscoelastic properties of the solid components and the fluid dynamics within the skin tissue are likely the two main factors that significantly affect the indentation response of skin. Therefore, in this and the next chapter, the feasibility of using two techniques, optical coherence elastography (OCE) and Doppler OCT, to evaluate the viscoelastic properties and the fluid transport within the skin tissue is studied.

3.1 Optical coherence elastography (OCE) and tissue viscoelasticity

Elastography is an imaging technique which facilitates diagnostic imaging by introducing mechanical contrast to biomedical images non-invasively [103]. The success of ultrasound elastography (USE) [104, 105] has stimulated extensive elastography studies using other imaging modalities such as magnetic resonance elastography (MRE) [106] and optical coherence elastography (OCE) [52, 107, 108]. OCE surpasses MRE and USE in the following aspects: (1) higher imaging resolution (micrometers), which allows for the discrimination of fine morphological features, (2) higher displacement sensitivity (hundreds of nanometers), which enables the detection of subtle changes in tissue deformation, and (3) faster image acquisition time (sub-seconds) [52]. However, compared to USE or MRE, OCE has a lower penetration depth (1-2 mm).

In general, all elastography techniques require a certain mechanical excitation source and some means of measuring the resulting deformation or dynamic response. OCE techniques can be categorized in several ways, such as being based on the time-scale of the measurements (static or

dynamic), configuration of the excitation source (internal or external), or the motion detection approach (phase-dependent or cross-correlation-dependent) [52, 107].

In terms of mechanical properties, to date, most OCE techniques have assumed the tissue to be linear and viscoelastic. Biological soft tissue is a complex material composed of both fluids and solids. Under certain assumptions, the viscoelastic mechanical response of the tissue can be described by empirical rheological models such as the Kelvin-Voigt and Maxwell models. In the Kelvin-Voigt model, the elastic and viscous components coexist in a parallel configuration, while the Maxwell model assumes the two components coexist in a serial manner [84].

Static OCE is a conventional OCE technique that relies on the spatial characteristics of the biological material, such as the deformation under a uniform stress field (intuitively, a stiffer material exhibits less deformation under the same loading). Stiffness is a one-dimensional characteristic often quantified by the Young's modulus, which has the widest dynamic range as compared to other elasticity parameters [109]. In general, for small deformations of an elastic material (usually less than 10% of the original length), the material will respond in a linear (Hookean) fashion. The Young's modulus E of such a material undergoing a uniaxial deformation can be given by

$$\mathrm{E} = \frac{\sigma}{\varepsilon}, \tag{3-1}$$

where σ is the imposed stress that can be obtained by the ratio of force loading to the area ($\sigma = \frac{F}{A}$), and ε is the fractional change in sample length ($\varepsilon = \frac{\Delta l}{l_0}$) of the material at the axial direction [84].

The elastic contrast is typically revealed in a strain map in response to a uniform stress field. Using this approach, static OCE has been demonstrated in postmortem aorta and cornea [110, 111], *ex vivo* human breast, lymph node, and ovary [112, 113], and *in vivo* human skin [114, 115]. However, strain mapping only provides a relative measurement. To quantify Young's modulus, techniques such as micro-indentation based on the Hertz contact theory [116], and optical

palpation where a translucent compliant silicone stress sensor is placed on the sample surface [117], can be implemented. Most static OCE techniques rely on contact-based, external excitation sources, such as a glass plate with a ring actuator or piston [112, 118], or a needle probe configuration with the needle inserted into the tissue [119].

Viscoelastic features can also be inferred from the characterization of the temporally-resolved dynamics. Numerous dynamic OCE techniques have been proposed and investigated, while conventionally the target variables of detection include the elastic wave propagation speed and the natural/resonant frequency. Crawling waves have been proposed lately as another approach that can be related to the elastic wave velocity, without the need for high imaging speed [120]. The elastic wave approach is perhaps a more favorable and common OCE technique since a quantitative result (e.g. the Young's modulus) is achievable and has been demonstrated on *in vivo* samples. The elastic-wave OCE techniques will be discussed in detail in Chapter 3.2. The natural/resonant frequencies are commonly probed by magnetomotive OCE (MM-OCE), which is a variant of OCE that utilizes superparamagnetic magnetomotive nanoparticles (MNPs) as internal force transducers, allowing for remote manipulation with an external magnetic field [121]. The natural/resonant frequency reflects the sample stiffness and can be detected via mechanical transient and spectroscopic responses. In the transient response method, a step-wise magnetic force is exerted on the MNP-loaded tissue, so that the MNPs along with the neighboring tissue will be driven by the magnetic force and settle at a new equilibrium position while undergoing an underdamped oscillation. Similarly, when the magnetic field is removed, the MNP-laden tissue is released from the magnetic force and the restoring force of the sample microenvironment will again result in an underdamped harmonic oscillation around its original equilibrium position [122]. Solving the equation of motion $m\ddot{z}(t)+\gamma\dot{z}(t)+kz(t)=F(t)$, the natural frequency (f_0) can be extracted, which is related to the damping (γ), spring (k) constants, and specimen mass (m), given as:

$$f_0 = \frac{1}{2\pi}\sqrt{\frac{k}{m} - \frac{\gamma}{4m^2}}\,. \tag{3-2}$$

Using Hooke's law, Young's modulus is given by $E = {kL}/{S}$, where L is the sample thickness L and S is the cross-sectional area that the force has been applied to. If the sample mass and shape are relatively constant, with negligible viscosity, a linearity between the natural frequency and the square root of the Young's modulus, $f_0 \propto \sqrt{E}$, can be observed [122, 123]. Hence, the higher the natural frequency, the stiffer the sample.

In dynamic OCE, several excitation configurations have been implemented. A mechanical vibrator and glass plate with mechanical actuators can be used for contact-based excitation [124-126]. Contact-free excitation configurations have also been utilized, including acoustic radiation forces [123, 127], laser-pulses [128], air-puffs [129, 130], or magnetic forces [122, 131]. Recently, an approach using magnetic force in a contact-based manner on *ex vivo* animal tissue has also been proposed [132]. Dynamic OCE techniques have been applied to different biomedical applications. In elastic-wave OCE, a contact-based external mechanical vibrator is commonly applied to *in vivo* human skin [15, 126]. A contact-free acoustic radiation force (ARF, internal source) and a focused air-puff beam (external source) have been applied to gelatin phantoms [133] and *ex vivo* and *in vivo* cornea [130, 134], and as an internal excitation source, magnetomotive nanoparticles have been demonstrated in *ex vivo* rat liver and chicken muscle tissues [55]. Transient-response MM-OCE has been applied to various *ex vivo* rabbit organs, such as muscle, adipose, lung, kidney, heart, and liver [131]. Spectroscopic OCE has been performed with a contact-based piezo-actuator on *ex vivo* rat mammary tissue [125] or with remote manipulation of magnetic force on *ex vivo* human breast tissue [135] or blood samples [136].

The mechanical responses can be detected by motion-tracking techniques such as speckle tracking (e.g. cross-correlation or speckle decorrelation [137, 138]) and phase-sensitive OCT [139, 140], where the latter is more common due to its larger dynamic range and the lower data acquisition requirement [52]. Dynamic OCE techniques are commonly performed with phase-

sensitive OCT, where the displacement response of the stimulated sample is estimated from the phase profile by [122]

$$d\varphi(dt) = \frac{4\pi n}{\lambda_0} dz(dt). \tag{3-3}$$

Here, dt is the time interval between adjacent scans, $d\varphi(dt)$ is the phase change, n is the refractive index of the material, λ_0 is the center wavelength of the OCT light source, and $dz(dt)$ is the displacement induced during the time interval dt. Recently, Doppler phase variance has also been utilized as an alternative way to detect the displacement (especially the transverse vibration), which is less affected by the bulk motion or phase wrapping issues [141].

3.2 Elastic-wave optical coherence elastography (Elastic-wave OCE)

3.2.1 Principle

The propagation behavior of elastic waves through materials provides another way to assess the biomechanical properties. Originating from the equation of motion and linked through the constitutive equation, shear wave propagation within an isotropic, linear elastic, homogeneous, incompressible material can be described by the Helmholtz equation [52, 106]

$$G\nabla^2 u - \rho \frac{\partial^2 u}{\partial t^2} = 0. \tag{3-4}$$

Here, u is the displacement and ρ is the sample density. The shear modulus G is related to Young's modulus E through $G = \frac{E}{2(1+\upsilon)}$, where the Poisson's ratio υ of soft tissues is typically close to 0.5 (υ of liquid). Young's modulus can then be approximated as $E \cong 3G = 3\rho^2 C_S$ since the shear modulus G can be extracted from the shear wave velocity C_S using [142]

$$C_S = \sqrt{\frac{G}{\rho}}. \tag{3-5}$$

Note that the shear modulus can also be calculated from the surface wave velocity. At $\upsilon = 0.5$, the shear wave and surface wave velocities give similar results. However, the two waves are conceptually different, as the shear wave represents the wave propagating within the bulk tissue and the surface wave describes the wave propagation confined to the surface region (~one wavelength in depth [15]).

In elastic-wave OCE, both an impulse and a harmonic oscillation waveform can be generated to propagate through or across the sample, where the group and phase velocities can be used for wave velocity calculations, respectively. When the excitation source has a point-wise characteristic in the lateral direction, a phase gradient $\frac{\Delta\phi}{\Delta r}$ can be obtained by linearly fitting the phase profile $\Delta\phi$ with respect to the radial spatial interval Δr, which can be used to compute the empirical phase velocity $C_S = \omega\frac{\Delta r}{\Delta\phi}$ [55]. In one study [55], MNPs were deployed into tissue-mimicking phantoms and tissue specimens, where the MNPs act as a cylindrical excitation source. The sample stiffness can be related to the wavelength of the elastic wave (i.e. a larger wave wavelength implies a higher elastic wave traveling speed, and hence the elasticity). For a viscoelastic body, the shear modulus is complex and the frequency-dependent shear wave speed (dispersion) can be quantified assuming a certain tissue model. Using the Kelvin-Voigt model, the shear wave speed dispersion can be given as [143]

$$C_S(\omega) = \sqrt{\frac{2\left(G^2 + \omega^2\eta^2\right)}{\rho\left(G + \sqrt{G^2 + \omega^2\eta^2}\right)}}, \tag{3-6}$$

where G is the real part of the complex shear modulus, ω is the angular frequency of excitation, ρ is the mass density, and η is the viscosity. The viscosity can be inferred from the slope of the wave velocity speed dispersion curve – the steeper the slope, the greater the viscosity [55]. When $\eta = 0$ or the shear modulus is much greater than the viscosity ($G \gg \eta$), the above equation become non-dispersive and reduces to Equation (3-5).

Previously, elastic-wave OCE has been performed in various ways with different advantages and limitations. The mechanical perturbation can be given in the form of a harmonic or impulse excitation, while the former ensures a higher wave propagation energy, the latter allows for a higher range of frequency response, in theory. In terms of the configuration of the excitation source, a point source can be given by the tip of a mechanical vibrator [126] or a focused air puff [129], which allows for spherical wave propagation (the spreading loss is proportional to the square of the wave propagation radius $\sim r^{-2}$ [144]). On the other hand, a line-shaped excitation can be performed either in the lateral direction using an external piezo shaker [15], or in the axial direction by injecting the magnetic nanoparticles into the sample [55] (Figure 3.1). This cylindrical-like wave propagation preserves a relatively higher energy (the spreading loss is proportional to the wave propagation radius $\sim r^{-1}$). When an excitation source is located at the sample surface, the elastic wave generated is termed a surface or Rayleigh wave (as mentioned earlier). The depth of the surface wave motion z depends on the wavelength λ and the frequency f of the driving force in the following manner.

$$z \approx \lambda = \frac{C_S}{f} \tag{3-7}$$

Therefore, the higher the excitation frequency, the shallower the probed depth. The property has been demonstrated and applied previously to obtain the elasticity of different layers of human

skin [15]. However, as the authors assumed the skin to be mostly elastic and ignored the viscous properties, how to decouple the dispersion caused by the depth penetration of the surface wave from the viscous nature of the sample has yet been discussed.

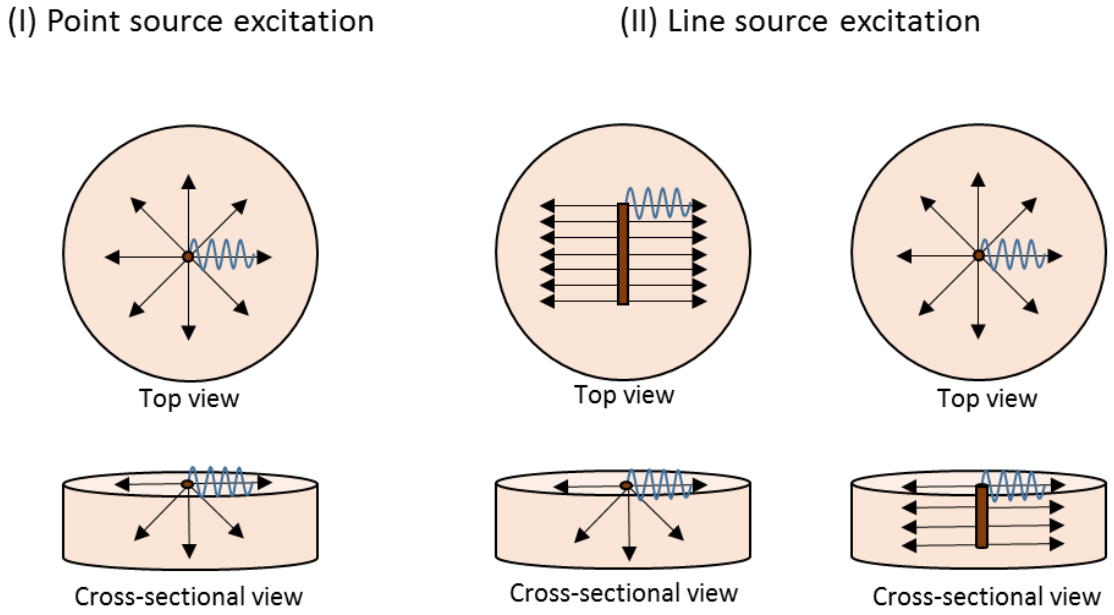

Figure 3.1. Schematic visualization of various configurations of excitation sources. (I) Point source (brown circle) excitation allows for a spherical wave propagation, where the wave propagates radially in both transverse and cross-sectional views. (II) Line source excitation can be exerted at (left) the transverse plane or (right) the axial direction. The wave propagates radially in the cross-sectional view for the former and in the transverse plane in the latter case. In all the diagrams here, the brown circle or line indicates the excitation source, the blue lines denote the elastic wave propagation, and the black line with arrow describes the wave propagation direction.

The detection scheme of the elastic wave velocity could take different forms. Commonly, the displacement on the sample is detected by point-scanning phase-sensitive OCT, where multiple M-mode scans were collected across a certain spatial range (M-B mode) with repeated excitation. Recently, a line-field scanning scheme has been proposed to acquire the spatial-temporal profile of the elastic wave in a single-shot manner, and increase the OCE measurement speed (5 mm in less than 15 msec) [145]. While most studies place both the mechanical excitation and displacement detection in parallel (both located at the sample surface), one study [141] implemented an orthogonal scheme, where the acoustic radiation force (ARF) excitation source is placed along the side of the sample and the OCT beam, at one lateral position, detects the wave

propagating through various depths over time. The biomechanical properties of the sample at deeper regions could be probed by placing the excitation source at a region beyond the OCT imaging depth and measuring the wave propagation delay at the sample surface [141]. Typically, most techniques fix the location of excitation and detect the wave propagation at different spatial locations. However, one study [146] proposed to fix the OCT detection beam at one location while moving the excitation source through various spatial positions. It is claimed that this scheme has the potential for detecting the shear modulus from speckle-free regions or speckle-less samples, such as a crystalline lens.

3.2.2 Results and discussions

Here, the quantification of Young's modulus was first demonstrated on tissue-mimicking silicone phantoms using contact-based elastic-wave OCE and the results were correlated with those from standard mechanical testing. Then, *in vivo* human data were collected and the Young's moduli were extracted using the same OCE technique.

Several room temperature vulcanizing (RTV)-based silicone phantoms were made from a mixture of a polydimethylsiloxane (PDMS) fluid, curing agent (RTV-A), and cross-linker (RTV-B). The fabrication procedure was similar to the protocol described in [135]. Briefly, a mixture of PDMS fluid, RTV-A, and RTV-B were created while titanium dioxide particles (size < 5 μm, 2 mg/ml) were added to increase optical scattering. The entire solution was sonicated for one hour. Sequentially, the solutions were poured into a Petri dish and placed inside an oven (80 °C) for 8 hr, resulting in a cylinder-shaped phantom with a diameter of 38 mm and a height of 5 mm. To create phantoms with varying stiffness, the concentration ratios of PDMS fluid:RTV-A:RTV-B were selected as 200:10:1, 100:10:1, and 30:10:1 (from soft to stiff). For the human subject study, we recruited a 31-year-old male patient with a BMI of 22.7 whose volar forearm and dorsal hand served as the main sites for the OCE measurements.

The mechanical properties of the PDMS phantoms were first characterized by the gold standard mechanical testing. Using a conventional uniaxial mechanical indentation instrument with a spherical indenter (radius 2.5 mm), the contact mechanics between a sphere and a half-space can be described via Hertz contact theory, $F = \frac{4}{3} E^* R^{1/2} d^{3/2}$. Here, F is the loading force, R is the indenter radius, d is the indentation depth, and $E^* = \left(\frac{1-\upsilon_s^2}{E_s} + \frac{1-\upsilon_p^2}{E_p} \right)^{-1}$ is related to the Young's modulus and the Poisson ratio of the spherical indenter (E_s , υ_s) at the deformable plane (E_p , υ_p) [147]. Assuming a rigid body, $E_s \to \infty$ and hence $E^* = \left(\frac{1-\upsilon_p^2}{E_p} \right)^{-1}$. To ensure the measurement is performed within the elastic region, data fitting was performed within a small depth range (0-5 mm in depth) to ensure a small strain (< 10%). The Young's moduli obtained for the three PDMS phantoms were determined to be 2.2±0.15 kPa, 7.35±0.32 kPa, and 43.89±11.31 kPa (mean ± standard deviation), respectively (Figure 3.3 (II)).

The experimental setup and data acquisition of elastic-wave OCE is described as follows. A force driven at a 153 Hz in a sinusoidal pattern was provided by a piezo-actuator, which was placed at the sample surface. The data collection was performed in such a way that the excitation of the piezo-actuator was synchronized with the camera acquisition (Figure 3.2). The OCT data were collected with M-B mode scanning, where a 32.6 msec duration M-mode (91,912 Hz line scan rate, 3,000 scans per frame) was collected at each lateral location (Figure 3.2).

The selected line scan rate guaranteed that the Nyquist sampling criteria would be met. A total of 100 locations were selected within a lateral range of 3.2 mm, where the spatial interval between each point scan was 32 μm (although the lateral pixel resolution can be increased by acquiring data at more points, 100 locations were selected to reduce the total data acquisition time).

The time interval between each sequential frame collection was 10 msec. The total acquisition time for one OCE dataset was 4.25 sec.

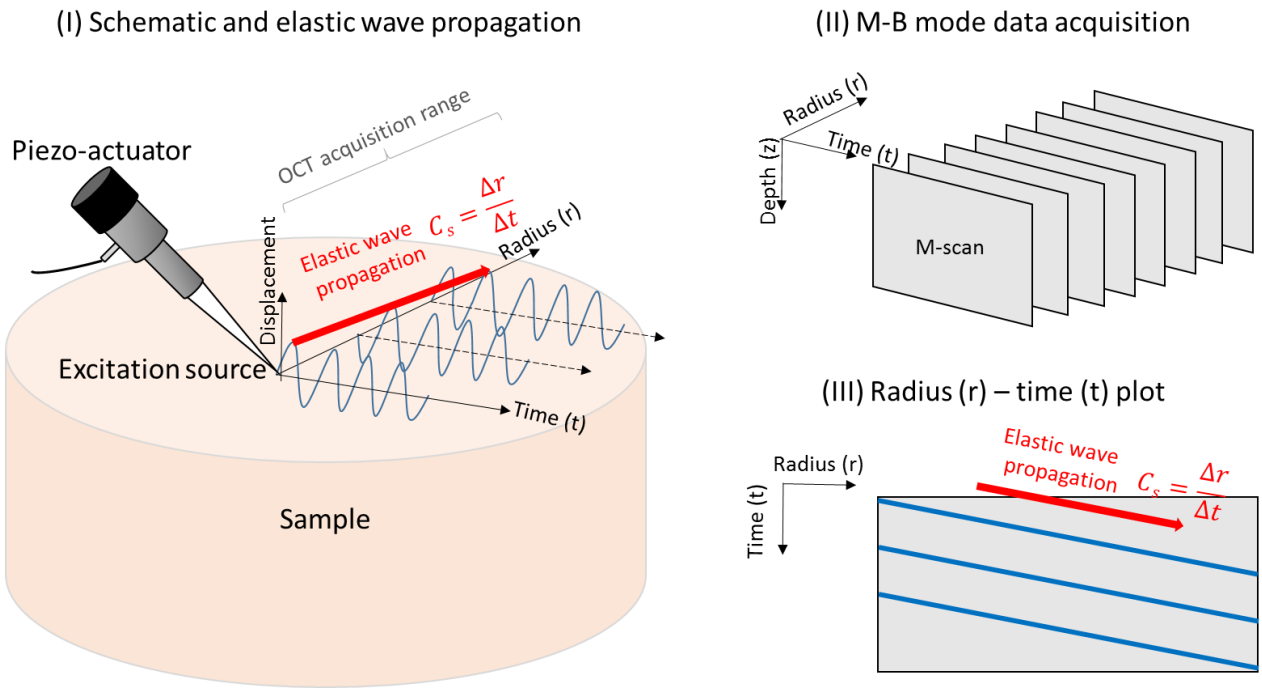

Figure 3.2. Illustration of the experimental setup and data acquisition for contact-based elastic wave-OCE. (I) The schematic of the experimental setup at the sample arm. A piezo-actuator was placed near the center of the sample at the surface to induce repetitive mechanical waves in a sinusoidal manner, while the excitation was synchronized with data acquisition. (II) The data collection was performed in a M-B mode scanning approach, where the elastic wave velocity can be extracted from (III) the radius-time plot.

The data processing flow is detailed as follows. First, standard OCT signal processing (background subtraction, resampling, and FFT) was performed. Sequentially, moving average filtering (over 10 pixels) was performed axially before phase extraction. Then, phase differences between adjacent line scans were obtained and unwrapped. Bandpass filtering was performed at 10% to 90% of the exciting frequency (153 Hz) to reduce the out-of-band noise. The filtered signals were averaged across 10 rows near the row detected with the maximum amplitude. The signal contrast was then stretched and normalized to fall within the range from 0 to 1. From the $r-t$ plot, the peaks of the wave at each side of the excitation source were detected and utilized

for linear fitting in order to obtain the wave propagation velocity ($C_S = \frac{\Delta r}{\Delta t}$), where the means and deviations of the results were calculated from a total of 6 wave propagations. To extract the Young's modulus, the mass density of skin was assumed to be 1040 kg/m^3 (i.e. $\rho = 1040\ kg/m^3$).

The OCE results of the PDMS phantom data are shown in Figure 3.3. It is observed that the stiffer the phantom, the higher the wave propagation speed (the steeper the $\frac{\Delta r}{\Delta t}$ slope), which correlates with theory. In addition, the elastic-wave OCE results also correlate with the Young's moduli obtained from conventional mechanical indention testing. However, the inspection also revealed that the standard deviation of the Young's modulus obtained from the OCE approach is larger than that from indentation. This is possibly due to the wave distortion during propagation, the fluctuation of the repetitive excitation waves, and the limited lateral range for wave propagation detection (which results in greater variation of the results at the stiffer sample, compared to the softer ones).

From the *in vivo* human skin results, it is observed that the volar forearm (E: 3±2.58 kPa; C_s: 0.85±0.43 m/s) is softer than the dorsal hand (E: 46.35±37.95 kPa; C_s: 3.48±1.38 m/s), as can be seen from the lower shear wave velocity of the former, compared to the latter (Figure 3.4). An inverse wave propagation direction is shown in the volar forearm data, which is possibly caused by the misalignment between the piezo-actuator tip and the OCT beam. However, it is believed that the accuracy of measurement is not significantly affected, given that the forearm stiffness characterized through the $\Delta r / \Delta t$ slope still agrees with the Young's modulus range obtained from the subcutaneous fat layer of the forearm measured in [15]. While the skeletal anatomy is more rigid than fat under the dorsal hand skin, it is also expected that the stiffness of the skin obtained from the dorsal hand should be higher. These results demonstrate the feasibility of using elastic-wave OCE on *in vivo* human skin. However, one can also observe a noisier signal in the human data. This is possibly due to the surface geometry and human subject motion during data acquisition. To make the measurement more stable, several approaches could be performed, such

as reducing the OCE measurement duration by using a higher frequency driving force, or implementing a faster line-field scanning platform [145].

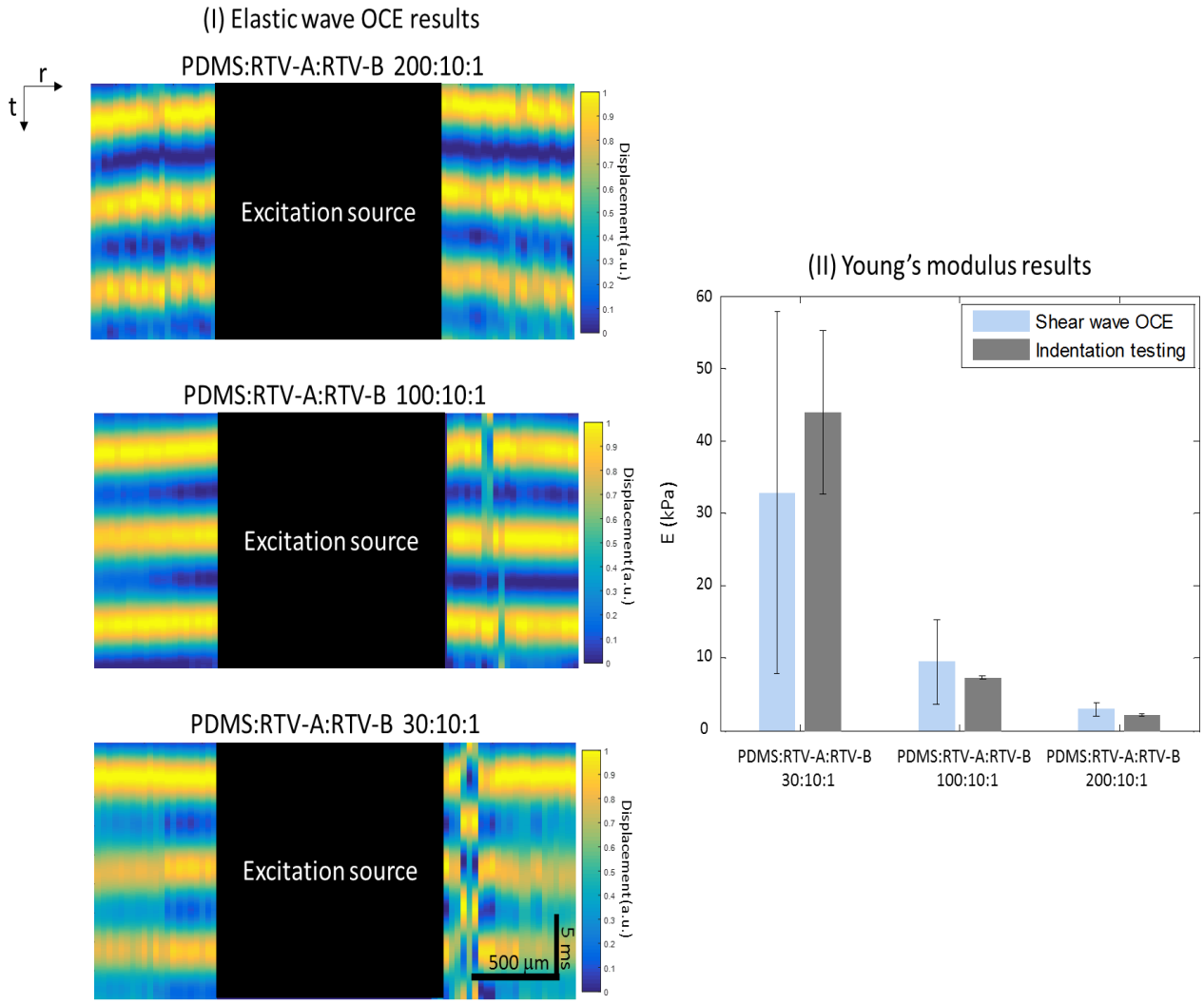

Figure 3.3. Elastic-wave OCE and indentation testing results of PDMS tissue-mimicking phantoms. (I) The radius-time plots from the OCE results for the three samples (from top to bottom, soft to stiff) are shown, where the a steeper $\Delta r/\Delta t$ slope indicates a faster wave velocity, seen in the stiffer sample. (II) The Young's modulus results obtained from both OCE and conventional mechanical testing are comparable and follow a similar trend.

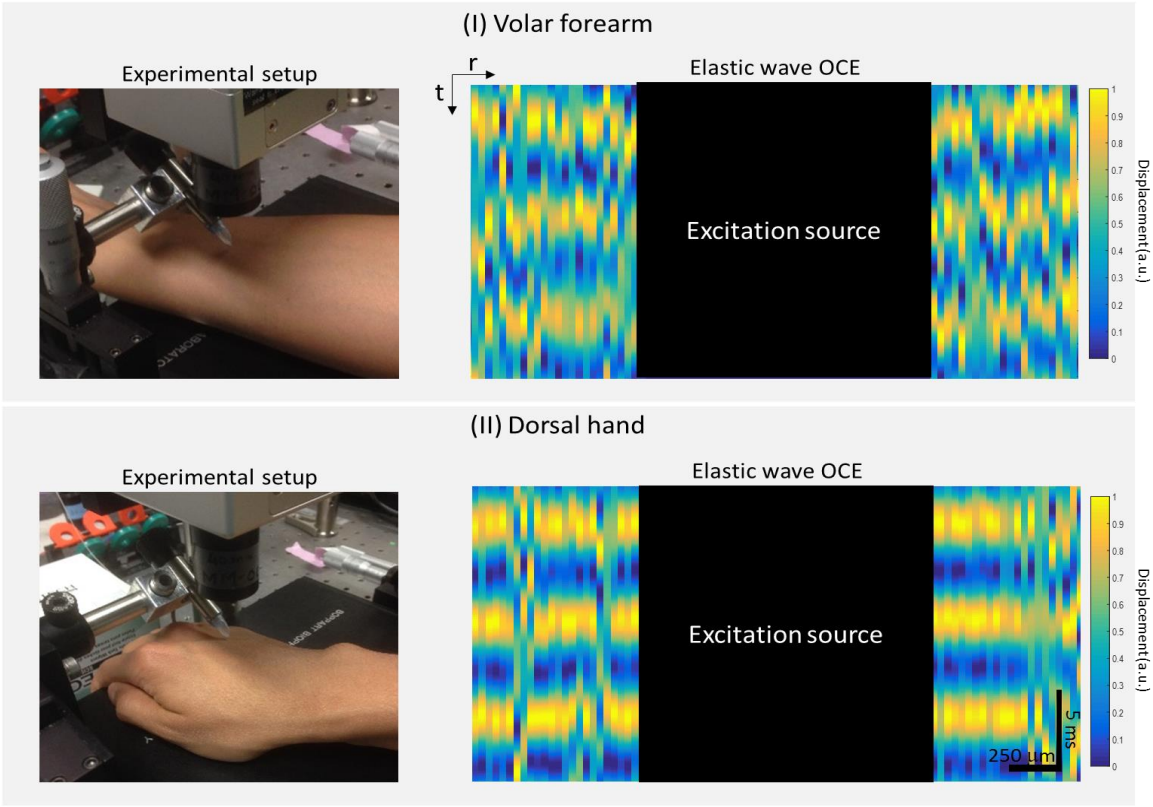

Figure 3.4. Experimental setup and *in vivo* elastic wave OCE results from the human (I) volar forearm and (II) dorsal hand. A higher elastic wave propagation velocity (steeper $\Delta r/\Delta t$ slope) is observed from the dorsal hand, indicating stiffer biomechanics as compared to the volar forearm.

The intrinsic biomechanical properties of the human skin could affect the responsive characteristics of the mechanically-perturbed skin spatially and/or temporally (e.g. for the stiffer skin, the same force loading would result in less deformation, and hence a potentially shorter temporal window for full recovery). Therefore, in the future, a systematic understanding of the linkage between the viscoelastic properties and the biomechanical response of the skin can be performed. The Young's modulus of the human subject can be characterized and compared to the quantitative morphological analysis results (as discussed in Chapter 2). In addition, since the localized mechanical compression would result in the transport and redistribution of ECF, the viscosity-related parameters can be characterized and related to the history-dependent responsive dynamics of the skin (e.g. the residual deformation as a function of time) as well.

3.3 Finite element methods (FEM)

3.3.1 Introduction

Numerous rheological models have been employed for biomechanical characterization, yet erroneous results may often appear due to violations of various mechanical assumptions. One way to alleviate this issue is by using the finite element method (FEM), which is an effective numerical tool that iteratively approximates the boundary value solutions [148]. In addition, FEM has shown to be a useful tool to model samples with complex mechanical properties and geometry, as in the practical case of biological tissues. To date, FEM has been implemented in both static [149, 150] and dynamic [135, 151] OCE. In one study [150], FEM was utilized to study the impact of mechanical parameters, the imaging system, and signal processing parameters on the mechanical contrast revealed in compressional OCE. In another study [135], FEM was applied to study the frequency response of heterogeneous samples with various mechanical properties.

3.3.2 Results and discussions

In this study, the relationship of the indenter geometry to the local compression results on human skin was investigated, similar to the research presented in Section 2.4.5. Both OCT images and FEM results were obtained and compared. In the OCT experiment, two custom-fabricated polymer-based indenters with different cross-section geometric shapes (square- and triangular-shaped) were applied to the same human subject prior to OCT data acquisition. As discussed in Chapter 2, the backscattered light intensity is associated with in-tissue deformation at the indented sites. Meanwhile, an FEM simulation using the COMSOL Multiphysics (v5.2) structural module was performed to reveal the stress and displacement distribution within a skin tissue specimen. Here, the skin was modeled using a Kelvin-Voigt viscoelastic model and assigned several mechanical parameters based on assumptions (Table 3.1). Since the indenters and the directions

of the compressive force were designed so that the maximum pressure gradients induced on the sample, as well as the indenter-geometry-dependent stress distributions, would mainly occur along depth, the focus was on the FEM simulation results in the cross-sectional plane ($x-z$ plane). Two types of indenters were modeled with the same cross-sectional dimensions as the indenters used in the experiment. The load was applied to the skin surface and sustained for 3 min. The resulting stress and displacement fields within the simulated skin at t=3 min are shown in Figure 3.5.

Table 3.1. Input parameters for FEM simulations.

Parameter	**Value**
FEM mesh size	Fine
Viscoelastic model	Kelvin-Voigt
Material	Skin
Young's modulus (E)	150 kPa (within the range of reported human skin stiffness [15, 126])
Viscosity (η)	4 mPa·s (viscosity of blood [152])
Poisson ratio (ν)	0.49
Applied force (F)	20 N (calculated based on the indentation area and the reported pain threshold ~1.1 MPa [59])
Force sustained duration	3 min

From the FEM results, geometric-dependent stress and spatial displacement distributions in the $x-z$ plane are observed. In the stress field, the highest stress exists at the contacting contour between the indenter and the sample, or at the edges of the indenter, in both cases, while the stress distribution within the sample are indenter-geometry-related. Additionally, the in-tissue displacement field resembles the indenter-geometry. These simulation results can be understood by considering the variation of contour contact and the change of surface area as the depth of the local indentation is increased during the loading process. Depends on the indenter geometry, the contact area between the indenter and the sample surface could either expand (e.g. for the indenter with a triangular cross-section) or remain relatively constant (e.g. for the indenter with a square cross-section) with an increasing indentation depth. As a result, the variations in the contact area

as a function of the indentation depth could lead to different spatial distributions of stress and displacement. In the cross-sectional plane, a square-shaped indentation introduces a similar deformation level across a wider lateral range, while the triangular-shaped indentation induces a similar displacement only across a narrow range. Also, the square-shaped indentation has a larger contact area and hence a smaller maximum displacement. The triangular-shaped indentation has a smaller contact area and a larger maximum displacement. Comparing the experimental OCT data to the simulation results, a similar spatial distribution of OCT intensity is observed, in comparison to the displacement fields from the FEM results. This indicates that the OCT backscattering intensity could be a suitable metric that reflects the degree of local compression, which agrees with the previous hypothesis. To further quantify the OCT intensity distribution, the FWHM of the lateral intensity profile can be applied (as shown in Section 2.4.5).

Note that only the trend of the deformation distribution are compared in this research, instead of the absolute values, due to the lack of knowledge on the empirical parameters such as the actual mechanical properties of the sample, the applied stress, and the actual incline of the skin surface with respect to the indentation direction, and so forth. In addition, the skin biomechanical properties were simulated rather simply by using a viscoelastic model without considering other mechanical features of the skin, such as its poroelasticity (which could be affected by physiological factors, such as the blood flow or interstitial fluid transport). The parameters of the imaging system, such as the signal-to-noise ratio (SNR), sampling rate, and displacement sensitivity, and the optical properties of the tissue, such as the attenuation properties, were also not taken into account either. In the future, the both the empirical characteristics of the human subject and the parameters of the imaging system should be obtained in order to improve the simulation accuracy.

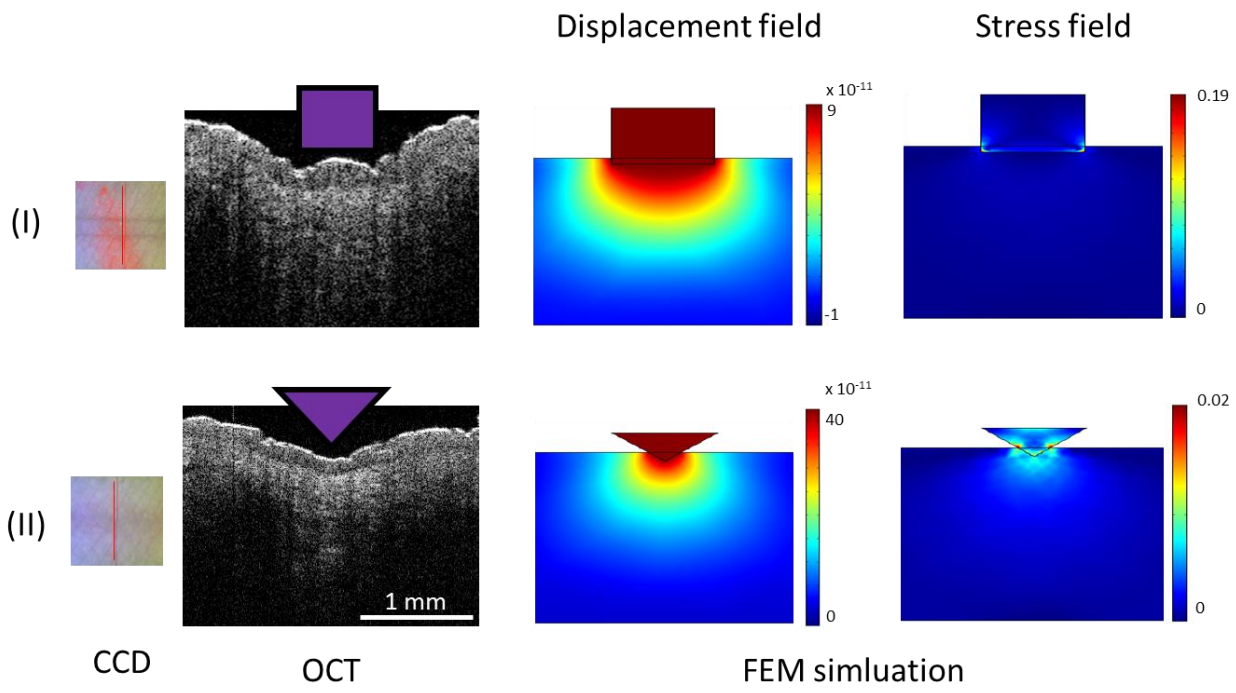

Figure 3.5. Experimental OCT and FEM simulation results of human skin following a 3-min indentation induced by indenters with (I) square and (II) triangular cross-sectional shapes (t=3min). The red lines on the CCD images indicate the scanning location for the OCT images.

4 Characterization of fluid dynamics in human tissue

4.1 Fluid dynamics inside the tissue

Several techniques have been proposed for detection and visualization of the existence of fluid flow within tissues, including Doppler OCT [153], speckle or phase variance [154], and optical microangiography (OMAG) [53]. The basic principle of Doppler OCT is relatively straightforward, which simply relies on the detection of the change in optical phases, and hence allows for a high displacement sensitivity. In addition, Doppler OCT technique enables quantification of the velocity of fluid flow and detection of the directionality of the fluid flow, which are not achievable in the speckle or phase variance methods. On the other hand, the data processing algorithm of Doppler OCT is less complicated than that of the OMAG techniques. Therefore, the focus will be on Doppler OCT in this thesis research.

4.2 Doppler optical coherence tomography (Doppler OCT)

4.2.1 Principle

Doppler OCT enables the visualization of the in-tissue fluid flow and the quantification of flow direction, where the motion of the moving particle(s) is obtained based on the detection of the Doppler frequency shift, $\Delta f = f_d - f_o$. Here, f_o is the frequency of the moving object and f_d is the frequency detected, which can be described as $f_d = \frac{c-u}{c+u} f_o$ (where c is the speed of light and u is the velocity of the moving particle). Given that the particle velocity is much smaller than that of the light ($u \ll c$), the frequency shift can be approximated as $\Delta f = \frac{u}{c} f_d$, which is proportional to the moving velocity of the object [34].

Expressed with the wave-vector k, the Doppler frequency shift detected with OCT can be given as $\Delta f = \frac{1}{2\pi}\left(k_d - k_o\right)\vec{u}$, where k_d are k_o the detected and moving-object wave-vectors, respectively (Figure 4.1). Thus, the frequency shift can be linked to the particle velocity by:

$$\Delta f = \frac{2u\cos\theta}{\lambda_0}. \tag{4-1}$$

Note that the direction of the particle motion is encoded in the sign of the frequency shift, where a positive sign ($\Delta f > 0$) indicates the particle moving toward the OCT imaging beam and a negative signal ($\Delta f < 0$) represents the object moving in the opposite direction.

The Doppler frequency shift can be extracted by the phase change between adjacent A-scans detected in OCT data, as shown below [153].

$$\Delta f = \frac{1}{2\pi}\frac{d\varphi}{dt} = \frac{1}{2\pi}\frac{\varphi_{j+1,z} - \varphi_{j,z}}{dt} = \frac{1}{2\pi}\frac{\arg\left(A_{j+1,z}\right) - \arg\left(A_{j,z}\right)}{\Delta T} \text{ or } \frac{1}{2\pi}\frac{\arg\left(A_{j+1,z}A_{j,z}^{*}\right)}{\Delta T} \tag{4-2}$$

Here, $A_{j,z}$ is the complex analytic signal obtained at the j-th line scan at depth z, $\varphi_{j,z}$ is the phase extracted from $A_{j,z}$, and ΔT is the time interval between two adjacent line scans.

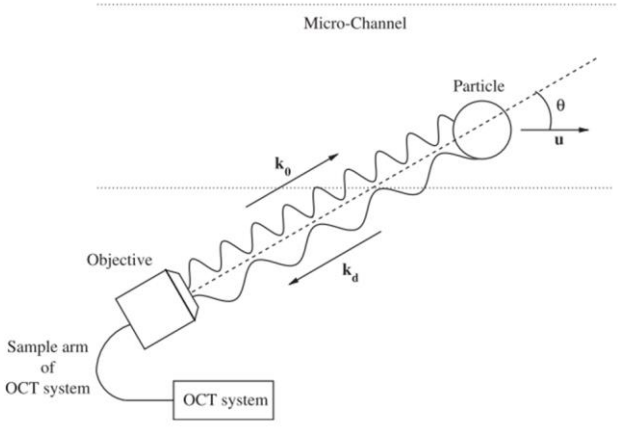

Figure 4.1. Illustration of a Doppler OCT sample arm and the motion of a moving particle [34].

The velocity range that can be probed with Doppler OCT is $u_{\min} \sim u_{\max} = \frac{\lambda_0 \delta\varphi}{4\pi n \Delta T} \sim \frac{\lambda_0}{4n\Delta T}$, which depends on the center wavelength of the light source λ_0, the refractive index of the sample n, the time interval between successively acquired line scans ΔT, and the range of detectable phase (i.e. from phase resolution $\delta\varphi$ to π). Therefore, certain *a priori* information, such as the velocity range of the targeted flow, are required for Doppler OCT measurements.

4.2.2 Results and discussions

Here, the Doppler OCT algorithm is first applied on data from a sample with flowing fluid to evaluate the performance of this algorithm. Sequentially, *in vivo* human gum data were processed in the same manner to obtain Doppler phase shift information. The flow phantom consisted of intralipid flowing inside a plastic capillary tube (data acquisition described in [155]), while the micro-vessels (with blood flow) residing in the human gum are the main detection target for the *in vivo* data. Since the micro-vessels are small in size, spatial oversampling was performed (i.e. lateral pixel resolution was set to 8 μm/pixel while the lateral resolution of the OCT system was ~ 16 μm). Additionally, two line scan rates were selected for data acquisition to enable the detection of blood flow rates within different ranges (the maximum detectable velocity for the 19.5 kHz and 30 kHz line scan rates were 2.9 mm/s and 4.6 mm/s, respectively, assuming the refractive index of skin to be 1.4).

Standard OCT signal processing (background subtraction, resampling, and FFT) was performed and the resulting complex analytical signals were used for Doppler phase shift quantification (using Equation (4-2)). Phase unwrapping was then performed on the phase shift results. The performance of the algorithm was demonstrated using the intralipid sample, where

strong phase shift amplitudes within the capillary tube were observed in the Doppler OCT data, while the structural OCT data (intensity profile) does not reveal any fluid flow information (Figure 4.2).

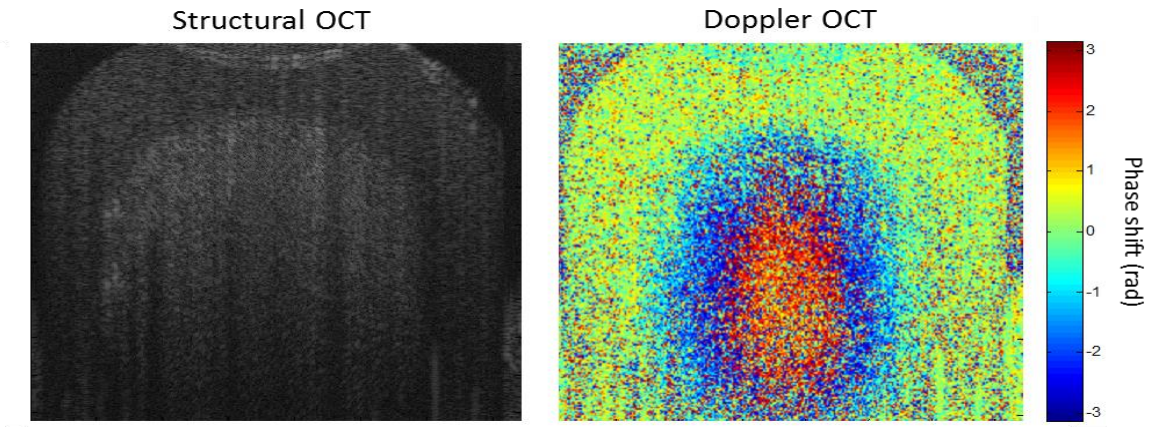

Figure 4.2. Structural OCT and Doppler OCT results of intralipid flow within a capillary tube. (Left) The intensity profile data reveals only subtle structural information, while (right) the Doppler shift map clearly illustrates the flow dynamics within the capillary tube. The Doppler shift can be converted to fluid flow velocity, as can be seen in Figure 4.3.

From the *in vivo* human gum data, small regions containing large phase shifts were revealed, which may indicate the presence of blood flow (Figure 4.3). Interestingly, when comparing the Doppler signal with the structural OCT image, one can see that the vessel-like structures (black holes) shown in the OCT image do not entirely correspond with the locations that exhibit the large Doppler phase shifts. This implies that the vasculature-like structures may not actually be blood vessel, or that the vessels do not contain any blood flow moving at a velocity that would fall within the detectable range of Doppler OCT under the data acquisition parameters used.

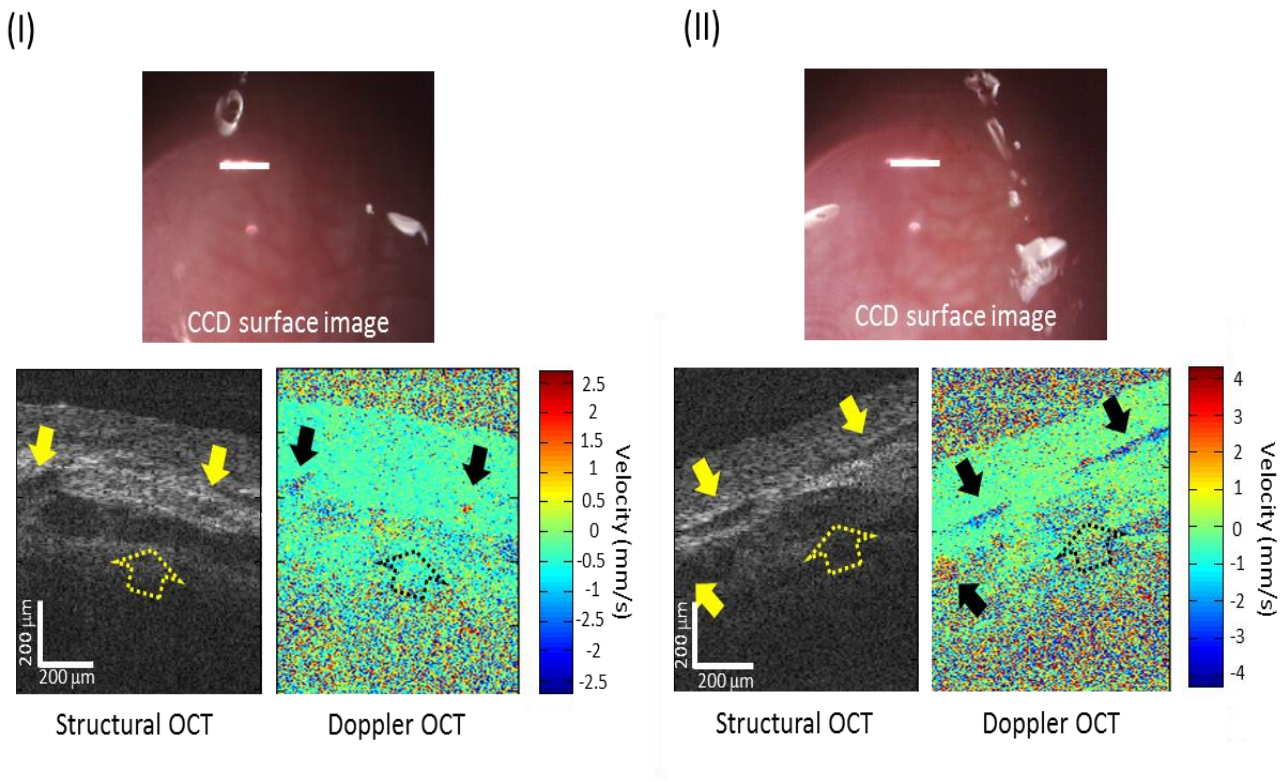

Figure 4.3. Structural and Doppler OCT results for *in vivo* human gum. (Bottom left) The OCT images were obtained at the lateral location indicated by a white line shown in (upper row) the CCD surface photos. The Doppler OCT data were collected with a line scan rate of (I) 19.5 kHz and (II) 30 kHz, respectively, and hence the fluid flows with different velocity ranges are observed. The black solid arrows in the Doppler OCT images indicate the presence of fluid flow, which correspond to the location indicated by the yellow solid arrows in the structural OCT images. At certain locations, vessel-like structures are seen in the structural OCT images (indicated with yellow, hollow, dashed arrows), however, obvious Doppler signals were not observed in the corresponding locations from the Doppler OCT images (indicated with black, hollow, dashed arrows).

Although Doppler OCT has been successfully demonstrated for detecting the vasculature in the human gum, there are several limitations. As mentioned earlier, certain *a priori* information about the fluid flow is required, which possesses challenges for Doppler OCT-based diagnostics. In addition, the optical scattering properties of the tissue will also have an impact on the Doppler OCT results. In ophthalmology, Doppler signals can be clearly seen due to the lower-scattering tissue in the eye [156]. However, the Doppler results from human skin are typically more vague and less obvious [54, 157]. This is possibly because that larger vessels are typically located in deeper regions, under more highly scattering skin tissue. Note that in this study, the Doppler

signals were acquired from the gum vessels that are close to the tissue surface, which lowers the influence of scattering.

In the future, the Doppler OCT techniques can be integrated to the skin compression studies, with the assistance of a translucent indenter. As the compressive force could reduce the distance between the skin surface and the embedded blood vessels, a reduced optical scattering along with the extended penetration depth of light (as discussed in Section 2.2.1) may allow for possible detection of microvascular structure in the skin. Therefore, by implementing Doppler OCT, the response of blood perfusion or the microcirculation in the skin tissue to the external mechanical loading may potentially be assessed, as demonstrated in a previous study [158] with the use of OMAG. With sufficient oversampling in the lateral direction, not only the morphological changes, but also the Doppler phase shifts induced by the fluid translocation, could be revealed in the skin as the tissue undergoes mechanical indentation. As a result, the association between the structural alterations (as discussed in Chapter 2) and the local hemodynamics or the temporal characteristics of the ECF, could possibly be investigated.

5 Conclusions and future directions

5.1 Conclusions

In conclusion, this thesis research demonstrated that OCT, along with the quantitative analysis and the functional extensions (such as OCE and Doppler OCT) are capable of visualizing the biomechanical response, viscoelastic properties, and fluid dynamics within *in vivo* human tissues, especially the skin.

Quantitatively, three novel metrics (both in-tissue and skin surface related) have been developed for OCT image characterization of the skin before and after indentation from external mechanical forces. The proposed metrics were first evaluated using a porous tofu phantom, which successively revealed the in-tissue alteration upon compression. Sequentially, the same metrics were applied to *in vivo* human skin data from both the adult forearm and the infant thigh. The analysis revealed significant differences between the pre- and the post-indentation (0-min) time periods, for all metrics. Moreover, the post-indentation recovery trends manifest observable differences between the adult forearm and the infant thigh tissues. These results suggest that the proposed OCT-image-based metrics not only can quantitatively distinguish optical tissue properties between indented and non-indented skin, but also have the potential for differentiating tissue with different biomechanical and physiological conditions, which may potentially assist in disease diagnosis.

In addition, the physical and physiological factors influencing the biomechanical response of skin can be assessed via functional OCT techniques. Elastic-wave OCE was applied to different anatomical sites (volar forearm and dorsal hand) on a human subject and exhibited distinct differences between stiffness values, quantified by Young's modulus. Additionally, blood flowing in micro-vessels in human gum tissue was successfully detected and visualized with Doppler OCT.

These demonstrate the functional capabilities of OCT, which, by providing further biomechanical and physiological characterization, may potentially increase the accuracy for clinical diagnosis.

5.2 Future directions

Human skin is a complex tissue and organ which exhibits complicated physical, mechanical, biological, and physiological properties. Subsequently, the mechanically-induced response of *in vivo* skin could be affected by numerous factors. In the future, a systematic investigation of human skin can be performed in order to correlate the quantitative results and analysis (based on OCT data) with the viscoelastic properties (by OCE) and/or the vascular distribution and hemodynamics (by Doppler OCT). Additionally, an integrated system combing OCT system, OCE hardware components, and Doppler OCT algorithms can conceivably be developed in the future, which may enable a multifunctional, quantitative, objective, and informative clinical diagnosis tool with potentially improved accuracy.

Improvements can be made for each technique as well. For the quantitative analysis, more automatic surface detection and image segmentation approaches (e.g. [94]) can be applied, and the in-tissue intensity artifacts [100] should also be removed in the pre-processing procedures. Moreover, transparent indenters (e.g. glass or plastic-based) and force sensors can be implemented in the future so that the alteration "during" indentation can be visualized and investigated, enabling a more quantitative assessment of the visco-elastic and poro-elastic properties of *in vivo* tissue. Additional metrics can also be developed based on the lateral spatial distribution of certain features, and hence the shear gradient of lateral fluid transport may be characterized as well. By tracking empirical parameters such as stress and the 3-D dimensions of the tissue specimen, FEM simulations can be performed with better accuracy.

For OCE investigations, a faster imaging scheme (increasing the driving force frequency or by line-field scanning [145]) can be applied to diminish the motion artifacts. More sophisticated models that consider poroelastic behaviors or nonlinear material behaviors (e.g. hypoelastic models) can implemented in FEM simulations as well [13]. Finally, more stable and higher resolution blood flow visualization can possibly be investigated with optical microangiography [53] in the future.

In conclusion, this thesis research demonstrates the feasibility of using OCT-based techniques (OCT and its functional extensions) not only to characterize the biomechanical response of the mechanically-perturbed skin, but also to assess the underlying physical and physiological properties of the *in vivo* human subjects (in particular, the intrinsic mechanical properties and the microvascular flow dynamics). While the biomechanical properties or the fluid dynamics characteristics alone could help reveal certain aspects of the health state of the human subjects, a combined knowledge of both may enable a more informative characteristics about the pathologies. In addition, the biomechanical response of the skin, as an outcome affected by both the intrinsic stiffness of the solid components and the accumulation level or dynamics of the fluid components, can be quantitatively evaluated and effectively associated with the physiological conditions of the human subjects. Collectively, a better understanding of the localized (e.g. the skin lesion) and/or the overall health conditions (e.g. heart-failure-induced edema) can be allowed, and hence potentially enable a more informative, objective, and quantitative tool for clinical diagnosis in the future.

References

1. Guy, G.P., et al., *Prevalence and costs of skin cancer treatment in the US, 2002− 2006 and 2007− 2011.* Am. J. Prev. Med, 2015. **48**(2): p. 183-187.
2. Mozaffarian, D., et al., *Heart disease and stroke statistics—2016 update.* Circulation, 2015.
3. Menke, A., et al., *Prevalence of and trends in diabetes among adults in the United States, 1988-2012.* JAMA, 2015. **314**(10): p. 1021-1029.
4. Marks, J.G. and J.J. Miller, *Lookingbill and Marks' Principles of Dermatology*. 2013: Elsevier Health Sciences.
5. Silver, F.K., L.M. Siperko, and G.P. Seehra, *Mechanobiology of force transduction in dermal tissue.* Skin Res. Technol., 2003. **9**(1): p. 3-23.
6. Weinstein, G.D. and R.J. Boucek, *Collagen and elastin of human dermis.* J. Invest. Dermatol., 1960. **35**(4): p. 227-229.
7. *Human skin diagram*. [cited 2016 Apr.]; Available from: http://www.seabuckthorn.com/images/Diagram-of-the-Human-Skin.jpg.
8. Bensouilah, J. and P. Buck, *Aromadermatology: Aromatherapy in the Treatment and Care of Common Skin Conditions*. 2006: Radcliffe Publishing.
9. Pierard, G.E. and C.M. Lapière, *Physiopathological variations in the mechanical properties of skin.* Arch. Dermatol. Res., 1977. **260**(3): p. 231-239.
10. Zaidi, Z. and S.W. Lanigan, *Skin: Structure and Function*, in *Dermatol. Clin. Practice*. 2010, Springer. p. 1-15.
11. Li, W., *Modelling methods for in vitro biomechanical properties of the skin: A review.* Biomed. Eng. Lett., 2015. **5**(4): p. 241-250.
12. Bernstein, E.F., et al., *Chronic sun exposure alters both the content and distribution of dermal glycosaminoglycans.* Br. J. Dermatol., 1996. **135**(2): p. 255-262.
13. Paul, E.B., et al., *Nonlinear and poroelastic biomechanical imaging: elastography beyond Young's modulus*, in *Handbook of Imaging in Biological Mechanics*. 2014, CRC Press. p. 199-216.
14. Kirkpatrick, S.J., et al., *Imaging the mechanical stiffness of skin lesions by in vivo acousto-optical elastography.* Opt. Express, 2006. **14**(21): p. 9770-9779.
15. Li, C., et al., *Determining elastic properties of skin by measuring surface waves from an impulse mechanical stimulus using phase-sensitive optical coherence tomography.* J. R. Soc. Interface 2012. **9**(70): p. 831-841.
16. Clark, J.A., J.C.Y. Cheng, and K.S. Leung, *Mechanical properties of normal skin and hypertrophic scars.* Burns, 1996. **22**(6): p. 443-446.
17. Verhaegen, P.D.H.M., et al., *Differences in collagen architecture between keloid, hypertrophic scar, normotrophic scar, and normal skin: an objective histopathological analysis.* Wound Repair Regen., 2009. **17**(5): p. 649-656.
18. Porth, C., *Essentials of Pathophysiology: Concepts of Altered Health States*. 2011: Lippincott Williams & Wilkins.
19. Berry, G.P., et al., *The spatio-temporal strain response of oedematous and nonoedematous tissue to sustained compression in vivo.* Ultrasound Med. Biol., 2008. **34**(4): p. 617-629.
20. Warren, J.V. and E.A. Stead, *Fluid dynamics in chronic congestive heart failure: an interpretation of the mechanisms producing the edema, increased plasma volume and elevated venous pressure in certain patients with prolonged congestive failure.* Arch. Intern. Med., 1944. **73**(2): p. 138-147.
21. Johnson, R.J., et al., *Potential role of sugar (fructose) in the epidemic of hypertension, obesity and the metabolic syndrome, diabetes, kidney disease, and cardiovascular disease.* Am. J. Clin. Nutr., 2007. **86**(4): p. 899-906.
22. Homans, J., *Thrombophlebitis of the lower extremities.* Ann. Surg., 1928. **87**(5): p. 641.

23. Gniadecka, M., *Localization of dermal edema in lipodermatosclerosis, lymphedema, and cardiac insufficiency: high-frequency ultrasound examination of intradermal echogenicity.* J. Am. Acad. Dermatol., 1996. **35**(1): p. 37-41.
24. Farage, M.A., et al., *Structural characteristics of the aging skin: a review.* Cutan. Ocul. Toxicol., 2007. **26**(4): p. 343-357.
25. Waller, J.M. and H.I. Maibach, *Age and skin structure and function, a quantitative approach (II): protein, glycosaminoglycan, water, and lipid content and structure.* Skin Res. Technol., 2006. **12**(3): p. 145-154.
26. Waller, J.M. and H.I. Maibach, *Age and skin structure and function, a quantitative approach (I): blood flow, pH, thickness, and ultrasound echogenicity.* Skin Res. Technol., 2005. **11**(4): p. 221-235.
27. Stamatas, G.N., et al., *Infant skin physiology and development during the first years of life: a review of recent findings based on in vivo studies.* Int. J. Cosmetic Sci., 2011. **33**(1): p. 17-24.
28. Stamatas, G.N., et al., *Infant skin microstructure assessed in vivo differs from adult skin in organization and at the cellular level.* Pediatr. Dermatol., 2010. **27**(2): p. 125-131.
29. Hoeger, P.H. and C.C. Enzmann, *Skin physiology of the neonate and young infant: a prospective study of functional skin parameters during early infancy.* Pediatr. Dermatol., 2002. **19**(3): p. 256-262.
30. Huang, D., et al., *Optical coherence tomography.* Science, 1991. **254**(5035): p. 1178-1181.
31. Schmitt, J.M., *Optical coherence tomography (OCT): A review.* IEEE J. Sel. Top. Quantum Electron., 1999. **5**(4): p. 1205-1215.
32. Fercher, A.F., et al., *Optical coherence tomography-principles and applications.* Rep. Prog. Phys., 2003. **66**(2): p. 239.
33. Drexler, W. and J.G. Fujimoto, *Optical Coherence Tomography: Technology and Applications*. 2008: Springer Science & Business Media.
34. Tomlins, P.H. and R.K. Wang, *Theory, developments and applications of optical coherence tomography.* J. Phys. D: Appl. Phys., 2005. **38**(15): p. 2519.
35. *Introduction to OCT*. [cited 2016 Apr.]; Available from: http://obel.ee.uwa.edu.au/research/fundamentals/introduction-oct/.
36. Shrestha, T.B., et al., *Stem cell-based photodynamic therapy.* Photochem. Photobiol. Sci., 2012. **11**(7): p. 1251-1258.
37. Adhi, M. and J.S. Duker, *Optical coherence tomography–current and future applications.* Curr. Opin. Ophthalmol., 2013. **24**(3): p. 213.
38. Sattler, E., R. Kästle, and J. Welzel, *Optical coherence tomography in dermatology.* J. Biomed. Opt., 2013. **18**(6): p. 061224-061224.
39. Vakoc, B.J., et al., *Cancer imaging by optical coherence tomography: preclinical progress and clinical potential.* Nat. Rev. Cancer, 2012. **12**(5): p. 363-368.
40. Bezerra, H.G., et al., *Intracoronary optical coherence tomography: a comprehensive review clinical and research applications.* JACC Cardiovas. Interv. , 2009. **2**(11): p. 1035-1046.
41. Hsieh, Y.-S., et al., *Dental optical coherence tomography.* Sensors, 2013. **13**(7): p. 8928-8949.
42. Rashidifard, C., et al., *The application of optical coherence tomography in musculoskeletal disease.* Arthritis, 2013. **2013**.
43. Tearney, G.J., et al., *Catheter-based optical imaging of a human coronary artery.* Circulation, 1996. **94**(11): p. 3013-3013.
44. Tearney, G.J., et al., *In vivo endoscopic optical biopsy with optical coherence tomography.* Science, 1997. **276**(5321): p. 2037-2039.
45. Jung, W., et al., *Handheld optical coherence tomography scanner for primary care diagnostics.* IEEE Trans. Biomed. Eng., 2011. **58**(3): p. 741-744.
46. Shelton, R.L., et al., *Optical coherence tomography for advanced screening in the primary care office.* J. Biophotonics, 2014. **7**(7): p. 525-533.

47. Erickson-Bhatt, S.J., et al., *Real-time imaging of the resection bed using a handheld probe to reduce incidence of microscopic positive margins in cancer Surgery.* Cancer Res., 2015. **75**(18): p. 3706-3712.
48. Ding, Z., -.P.L. C, and Y. Chen, *Technology developments and biomedical applications of polarization-sensitive optical coherence tomography.* Front. Optoelectron., 2015. **8**(2): p. 128-140.
49. South, F.A., et al., *Differentiation of ex vivo human breast tissue using polarization-sensitive optical coherence tomography.* Biomed. Opt. Express, 2014. **5**(10): p. 3417-3426.
50. Oldenburg, A.L., et al., *Imaging and elastometry of blood clots using magnetomotive optical coherence tomography and labeled platelets.* IEEE J. Sel. Top. Quantum Electron., 2012. **18**(3): p. 1100-1109.
51. John, R., et al., *In vivo magnetomotive optical molecular imaging using targeted magnetic nanoprobes.* Proc. Natl. Acad. Sci. USA, 2010. **107**(18): p. 8085-8090.
52. Kennedy, B.F., K.M. Kennedy, and D.D. Sampson, *A review of optical coherence elastography: Fundamentals, techniques and prospects.* IEEE J. Sel. Top. Quantum Electron., 2014. **20**(2): p. 272-288.
53. Wang, R.K., *Optical microangiography: a label-free 3-D imaging technology to visualize and quantify blood circulations within tissue beds in vivo.* Selected Topics in Quantum Electronics, IEEE Journal of, 2010. **16**(3): p. 545-554.
54. Zhao, Y.H., et al., *Phase-resolved optical coherence tomography and optical Doppler tomography for imaging blood flow in human skin with fast scanning speed and high velocity sensitivity.* Opt. Lett., 2000. **25**(2): p. 114-116.
55. Ahmad, A., et al., *Magnetomotive optical coherence elastography using magnetic particles to induce mechanical waves.* Biomed. Opt. Express, 2014. **5**(7): p. 2349-2361.
56. Ralston, T.S., et al., *Data Analysis and Signal Postprocessing for Optical Coherence Tomography.* Optical Coherence Tomography: Technology and Applications, 2015: p. 407-436.
57. Bazant-Hegemark, F. and N. Stone, *Towards automated classification of clinical optical coherence tomography data of dense tissues.* Lasers Med. Sci., 2009. **24**(4): p. 627-638.
58. Wang, R.K. and V.V. Tuchin, *Optical Coherence Tomography: Light Scattering and Imaging Enhancement*, in *Handbook of Coherent-Domain Optical Methods*, V.V. Tuchin, Editor. 2013, Springer New York. p. 665-742.
59. Gurjarpadhye, A.A., et al., *Effect of localized mechanical indentation on skin water content evaluated using OCT.* J. Biomed. Imag., 2011. **2011**: p. 17.
60. Larin, K.V., et al., *Optical clearing for OCT image enhancement and in-depth monitoring of molecular diffusion.* IEEE J. Sel. Top. Quantum Electron., 2012. **18**(3): p. 1244-1259.
61. Drew, C., T.E. Milner, and C.G. Rylander, *Mechanical tissue optical clearing devices: evaluation of enhanced light penetration in skin using optical coherence tomography.* J. Biomed. Opt., 2009. **14**(6): p. 064019-064019-6.
62. Zhong, H.Q., et al., *Quantification of glycerol diffusion in human normal and cancer breast tissues in vitro with optical coherence tomography.* Laser Phys. Lett., 2010. **7**(4): p. 315.
63. Wang, S., et al., *Three-dimensional computational analysis of optical coherence tomography images for the detection of soft tissue sarcomas.* J. Biomed. Opt., 2013. **19**(2): p. 021102-021102.
64. Rylander, C.G., et al., *Dehydration mechanism of optical clearing in tissue.* J. Biomed. Opt., 2006. **11**(4): p. 041117-041117-7.
65. Agrba, P.D., et al., *Compression as a method for increasing the informativity of optical coherence tomography of biotissues.* Opt. Spectrosc., 2009. **107**(6): p. 853-858.
66. Zysk, A.M. and S.A. Boppart, *Computational methods for analysis of human breast tumor tissue in optical coherence tomography images.* J. Biomed. Opt., 2006. **11**(5): p. 054015-054015-7.
67. Cheng, Y. and K.V. Larin, *Artificial fingerprint recognition by using optical coherence tomography with autocorrelation analysis.* Appl. Opt., 2006. **45**(36): p. 9238-9245.

68. Oldenburg, A.L., C. Xu, and S.A. Boppart, *Spectroscopic optical coherence tomography and microscopy.* IEEE J. Sel. Top. Quantum Electron., 2007. **13**(6): p. 1629-1640.
69. Schmitt, J.M., S.H. Xiang, and K.N. Yung, *Speckle in optical coherence tomography.* J. Biomed. Opt., 1999. **4**(1): p. 95-105.
70. Gossage, K.W., et al., *Texture analysis of speckle in optical coherence tomography images of tissue phantoms.* Phys. Med. Biol., 2006. **51**(6): p. 1563.
71. Lingley-Papadopoulos, C.A., et al., *Computer recognition of cancer in the urinary bladder using optical coherence tomography and texture analysis.* J. Biomed. Opt., 2008. **13**(2): p. 024003-024003-9.
72. Ughi, G.J., et al., *Automated tissue characterization of in vivo atherosclerotic plaques by intravascular optical coherence tomography images.* Biomed. Opt. Express, 2013. **4**(7): p. 1014-1030.
73. Pande, P., et al., *Automated classification of optical coherence tomography images for the diagnosis of oral malignancy in the hamster cheek pouch.* J. Biomed. Opt., 2014. **19**(8): p. 086022-086022.
74. Sullivan, A.C., J.P. Hunt, and A.L. Oldenburg, *Fractal analysis for classification of breast carcinoma in optical coherence tomography.* J. Biomed. Opt., 2011. **16**(6): p. 066010-066010-6.
75. Lopes, A., R. Touzi, and E. Nezry, *Adaptive speckle filters and scene heterogeneity.* IEEE Trans. Geosci Remote Sens. , 1990. **28**(6): p. 992-1000.
76. Yu, Y. and S.T. Acton, *Speckle reducing anisotropic diffusion.* IEEE Trans. Imag. Process., 2002. **11**(11): p. 1260-1270.
77. Cheng, H.D., et al., *Automated breast cancer detection and classification using ultrasound images: A survey.* Pattern Recognit., 2010. **43**(1): p. 299-317.
78. Babu, J.J.J. and G.F. Sudha, *Adaptive speckle reduction in ultrasound images using fuzzy logic on Coefficient of Variation.* Biomed. Signal Process. Control, 2016. **23**: p. 93-103.
79. Mora, M., C. Tauber, and H. Batatia. *Robust level set for heart cavities detection in ultrasound images.* in *Comput. Cardiol.* 2005. IEEE.
80. Carvalho, E.A., et al., *SAR imagery segmentation by statistical region growing and hierarchical merging.* Digit. Signal Process. , 2010. **20**(5): p. 1365-1378.
81. Tearney, G.J., et al., *Quantification of macrophage content in atherosclerotic plaques by optical coherence tomography.* Circulation, 2003. **107**(1): p. 113-119.
82. Vincent, J., *Structural biomaterials*. 2012: Princeton University Press.
83. Carlsson, S. and P.-L. Larsson, *On the determination of residual stress and strain fields by sharp indentation testing.: Part I: theoretical and numerical analysis.* Acta Mater., 2001. **49**(12): p. 2179-2191.
84. Tschoegl, N.W., *The Phenomenological Theory of Linear Viscoelastic Behavior: An Introduction*. 1989, Berlin, German: Springer-Verlag Berlin Heidelberg.
85. Sridhar, M., J. Liu, and M.F. Insana, *Viscoelasticity imaging using ultrasound: parameters and error analysis.* Phys. Med. Biol., 2007. **52**(9): p. 2425-2443.
86. Oomens, C., M. Brekelmans, and F. Baaijens, *Biomechanics: concepts and computation*. 2009: Cambridge University Press.
87. Bates, D.O., J.R. Levick, and P.S. Mortimer, *Quantification of rate and depth of pitting in human edema using an electronic tonometer.* Lymphology, 1994. **27**(4): p. 159-172.
88. Lindahl, O.A., *The evaluation of a biexponential model for description of intercompartmental fluid shifts in compressed oedematous tissue.* Physiol. Meas., 1995. **16**(1): p. 17.
89. Mridha, M. and S. Ödman, *Noninvasive method for the assessment of subcutaneous oedema.* Med. Biol. Eng. Comp., 1986. **24**(4): p. 393-398.
90. Leiderman, R., et al., *Coupling between elastic strain and interstitial fluid flow: ramifications for poroelastic imaging.* Phys. Med. Biol., 2006. **51**(24): p. 6291.
91. Pattison, A.J., et al., *A dynamic mechanical analysis technique for porous media.* IEEE Trans. Biomed. Eng., 2015. **62**(2): p. 443-449.

92. Kim, Y.T., et al., *Evaluation of tissue mimicking quality of tofu for biomedical ultrasound.* Ultrasound Med. Biol., 2009. **35**(3): p. 472-481.
93. Garcia-Allende, P.B., et al., *Morphological analysis of optical coherence tomography images for automated classification of gastrointestinal tissues.* Biomed. Opt. Express, 2011. **2**(10): p. 2821-2836.
94. Hori, Y., et al., *Automatic characterization and segmentation of human skin using three-dimensional optical coherence tomography.* Opt. Express, 2006. **14**(5): p. 1862-1877.
95. Qi, X., et al., *Computer-aided diagnosis of dysplasia in Barrett's esophagus using endoscopic optical coherence tomography.* J. Biomed. Opt., 2006. **11**(4): p. 044010-044010-10.
96. Weissman, J., T. Hancewicz, and P. Kaplan, *Optical coherence tomography of skin for measurement of epidermal thickness by shapelet-based image analysis.* Opt. Express, 2004. **12**(23): p. 5760-5769.
97. Wang, C., et al., *Automated assessment of epidermal thickness and vascular density of port wine stains OCT image.* J. Innov. Opt. Health Sci., 2014. **7**(01): p. 1350052.
98. Avanaki, M.R.N. and A. Hojjatoleslami, *Skin layer detection of optical coherence tomography images.* Optik, 2013. **124**(22): p. 5665-5668.
99. Wang, J., et al., *Evaluation of optical clearing with the combined liquid paraffin and glycerol mixture.* Biomed. Opt. Express, 2011. **2**(8): p. 2329-2338.
100. Liew, Y.M., et al., *Reduction of image artifacts in three-dimensional optical coherence tomography of skin in vivo.* J. Biomed. Opt., 2011. **16**(11): p. 116018-11601810.
101. Vargas, G., et al., *Use of an agent to reduce scattering in skin.* Lasers Surg. Med. , 1999. **24**(2): p. 133-141.
102. Scolaro, L., et al., *Parametric imaging of the local attenuation coefficient in human axillary lymph nodes assessed using optical coherence tomography.* Biomed. Opt. Express, 2012. **3**(2): p. 366-379.
103. Sarvazyan, A., et al., *An overview of elastography-An emerging branch of medical imaging.* Curr. Med. Imaging Rev., 2011. **7**(4): p. 255-282.
104. Ophir, J., et al., *Elastography: A quantitative method for imaging the elasticity of biological tissues.* Ultrasonic Imag., 1991. **13**(2): p. 111-34.
105. Krouskop, T.A., et al., *Elastic moduli of breast and prostate tissues under compression.* Ultrasonic Imag., 1998. **20**(4): p. 260-74.
106. Manduca, A., et al., *Magnetic resonance elastography: Non-invasive mapping of tissue elasticity.* Med. Image Anal., 2001. **5**(4): p. 237-54.
107. Liang, X., V. Crecea, and S.A. Boppart, *Dynamic optical coherence elastography: A review.* J. Innov. Opt. Health Sci., 2010. **3**(4): p. 221-233.
108. Wang, S. and K.V. Larin, *Optical coherence elastography for tissue characterization: A review.* J. Biophotonics, 2015. **8**(4): p. 279-302.
109. Greenleaf, J.F., M. Fatemi, and M. Insana, *Selected methods for imaging elastic properties of biological tissues.* Annu. Rev. Biomed. Eng., 2003. **5**: p. 57-78.
110. Rogowska, J., et al., *Optical coherence tomographic elastography technique for measuring deformation and strain of atherosclerotic tissues.* Heart, 2004. **90**(5): p. 556-62.
111. Ford, M.R., et al., *Method for optical coherence elastography of the cornea.* J. Biomed. Opt., 2011. **16**(1): p. 016005.
112. Kennedy, B.F., et al., *Optical coherence micro-elastography: mechanical-contrast imaging of tissue microstructure.* Biomed. Opt. Express, 2014. **5**(7): p. 2113-24.
113. Nandy, S., et al., *Correlating optical coherence elastography based strain measurements with collagen content of the human ovarian tissue.* Biomed. Opt. Express, 2015. **6**(10): p. 3806-3811.
114. Kennedy, B.F., et al., *In vivo three-dimensional optical coherence elastography.* Opt. Express, 2011. **19**(7): p. 6623-34.
115. Kennedy, B.F., et al., *In vivo dynamic optical coherence elastography using a ring actuator.* Opt. Express, 2009. **17**(24): p. 21762-72.

116. Yang, Y., et al., *A novel optical coherence tomography-based micro-indentation technique for mechanical characterization of hydrogels.* J. R. Soc. Interface, 2007. **4**(17): p. 1169-73.
117. Kennedy, K.M., et al., *Optical palpation: optical coherence tomography-based tactile imaging using a compliant sensor.* Opt. Lett., 2014. **39**(10): p. 3014-3017.
118. Nahas, A., et al., *3D static elastography at the micrometer scale using Full Field OCT.* Biomed. Opt. Express, 2013. **4**(10): p. 2138-2149.
119. Kennedy, K.M., et al., *Needle optical coherence elastography for the measurement of microscale mechanical contrast deep within human breast tissues.* J. Biomed. Opt., 2013. **18**(12): p. 121510-121510.
120. Meemon, P., et al., *Crawling wave optical coherence elastography.* Opt. Lett., 2016. **41**(5): p. 847-850.
121. Oldenburg, A.L., et al., *Phase-resolved magnetomotive OCT for imaging nanomolar concentrations of magnetic nanoparticles in tissues.* Opt. Express, 2008. **16**(15): p. 11525-39.
122. Crecea, V., et al., *Magnetomotive nanoparticle transducers for optical rheology of viscoelastic materials.* Opt. Express, 2009. **17**(25): p. 23114-22.
123. Qi, W., et al., *Resonant acoustic radiation force optical coherence elastography.* Appl. Phys. Lett., 2013. **103**(10): p. 103704.
124. Liang, X., et al., *Optical micro-scale mapping of dynamic biomechanical tissue properties.* Opt. Express, 2008. **16**(15): p. 11052-65.
125. Adie, S.G., et al., *Spectroscopic optical coherence elastography.* Opt. Express, 2010. **18**(25): p. 25519-34.
126. Liang, X. and S.A. Boppart, *Biomechanical properties of in vivo human skin from dynamic optical coherence elastography.* IEEE Trans. Biomed. Eng., 2010. **57**(4): p. 953-9.
127. Adie, S.G., et al., *Audio frequency in vivo optical coherence elastography.* Phys. Med. Biol., 2009. **54**(10): p. 3129-39.
128. Li, C., Z. Huang, and R.K. Wang, *Elastic properties of soft tissue-mimicking phantoms assessed by combined use of laser ultrasonics and low coherence interferometry.* Opt. Express, 2011. **19**(11): p. 10153-10163.
129. Wang, S., et al., *Noncontact measurement of elasticity for the detection of soft-tissue tumors using phase-sensitive optical coherence tomography combined with a focused air-puff system.* Opt. Lett., 2012. **37**(24): p. 5184-5186.
130. Wang, S. and K.V. Larin, *Noncontact depth-resolved micro-scale optical coherence elastography of the cornea.* Biomed. Opt. Express, 2014. **5**(11): p. 3807-21.
131. Crecea, V., A. Ahmad, and S.A. Boppart, *Magnetomotive optical coherence elastography for microrheology of biological tissues.* J. Biomed. Opt., 2013. **18**(12): p. 121504.
132. Wu, C., et al. *Lorentz Force Megahertz Optical Coherence Elastography*. in *SPIE BiOS*. 2016. SPIE.
133. Liang, X., et al., *Acoustomotive optical coherence elastography for measuring material mechanical properties.* Opt. Lett., 2009. **34**(19): p. 2894-2896.
134. Li, J., et al., *Dynamic optical coherence tomography measurements of elastic wave propagation in tissue-mimicking phantoms and mouse cornea in vivo.* J. Biomed. Opt., 2013. **18**(12): p. 121503-121503.
135. Ahmad, A., et al., *Mechanical contrast in spectroscopic magnetomotive optical coherence elastography.* Phys. Med. Biol., 2015. **60**(17): p. 6655-68.
136. Wu, G., et al., *High sensitivity micro-elastometry: Applications in blood coagulopathy.* Ann. Biomed. Eng., 2013. **41**(10): p. 2120-9.
137. Ahmad, A., et al., *Cross-correlation-based image acquisition technique for manually-scanned optical coherence tomography.* Opt. Express, 2009. **17**(10): p. 8125-36.
138. Kirkpatrick, S.J., R.K. Wang, and D.D. Duncan, *OCT-based elastography for large and small deformations.* Opt. Express, 2006. **14**(24): p. 11585-97.
139. Wang, R.K., S. Kirkpatrick, and M. Hinds, *Phase-sensitive optical coherence elastography for mapping tissue microstrains in real time.* Appl. Phys. Lett., 2007. **90**(16): p. 164105.

140. Song, S., Z. Huang, and R.K. Wang, *Tracking mechanical wave propagation within tissue using phase-sensitive optical coherence tomography: motion artifact and its compensation.* J. Biomed. Opt., 2013. **18**(12): p. 121505-121505.
141. Zhu, J., et al., *Imaging and characterizing shear wave and shear modulus under orthogonal acoustic radiation force excitation using OCT Doppler variance method.* Opt. Lett., 2015. **40**(9): p. 2099-2102.
142. Achenbach, J.D., *Wave Propagation in Elastic Solids*. 1987, Amsterdam, Netherlands: North-Holland.
143. Yamakoshi, Y., J. Sato, and T. Sato, *Ultrasonic imaging of internal vibration of soft tissue under forced vibration.* IEEE Trans. Ultrason. Ferroelectr. Freq. Control, 1990. **37**(2): p. 45-53.
144. Preisig, J., *Acoustic propagation considerations for underwater acoustic communications network development.* ACM SIGMOBILE Mobile Comp. and Comm. Rev., 2007. **11**(4): p. 2-10.
145. Liu, C.-H., et al. *Single Shot Line-Field Optical Coherence Elastography*. in *SPIE BiOS*. 2016. SPIE.
146. Hsieh, B.-Y., et al. *Elasticity Imaging of Speckle-Free Tissue Regions with Moving Acoustic Radiation Force and Phase-sensitive Optical Coherence Tomography*. in *SPIE BiOS*. 2016. SPIE.
147. Johnson, K.L., *Contact Mechanics*. 1987: Cambridge University Press.
148. Hughes, T.J.R., *The Finite Element Method: Linear Static and Dynamic Finite Element Analysis*. 2012, New York, USA: Dover Publications.
149. Chin, L.X., et al., *Analysis of image formation in optical coherence elastography using a multiphysics approach.* Biomed. Opt. Express, 2014. **5**(9): p. 2913-2930.
150. Kennedy, K.M., et al., *Analysis of mechanical contrast in optical coherence elastography.* J. Biomed. Opt., 2013. **18**(12): p. 121508-121508.
151. Han, Z., et al., *Analysis of the effects of curvature and thickness on elastic wave velocity in cornea-like structures by finite element modeling and optical coherence elastography.* Appl. Phys. Lett., 2015. **106**(23): p. 233702.
152. Mollica, F., L. Preziosi, and K.R. Rajagopal, *Modeling of Biological Materials*. 2007: Springer Science & Business Media.
153. Liu, G. and Z. Chen, *Phase-resolved Doppler optical coherence tomography*. 2012: INTECH Open Access Publisher.
154. Mahmud, M.S., et al., *Review of speckle and phase variance optical coherence tomography to visualize microvascular networks.* J. Biomed. Opt., 2013. **18**(5): p. 050901-050901.
155. Monroy, G., *Non-Invasive Optical Quantification of Otitis Media and Middle Ear Effusions*. 2014, University of Illinois at Urbana-Champaign.
156. Werkmeister, R.M., et al., *Measurement of Absolute Blood Flow Velocity and Blood Flow in the Human Retina by Dual-Beam Bidirectional Doppler Fourier-Domain Optical Coherence TomographyFlow Velocity Values with Bidirectional Doppler FD-OCT.* Invest. Ophthalmol. Vis. Sci., 2012. **53**(10): p. 6062-6071.
157. Zhao, Y., et al., *Doppler standard deviation imaging for clinical monitoring of in vivo human skin blood flow.* Opt. Lett., 2000. **25**(18): p. 1358-1360.
158. Choi, W.J., H. Wang, and R.K. Wang, *Optical coherence tomography microangiography for monitoring the response of vascular perfusion to external pressure on human skin tissue.* J. Biomed. Opt., 2014. **19**(5): p. 056003-056003.